Wave-CAIPI for Accelerated Dynamic MRI of the Thorax

Beschleunigte Dynamische MR-Bildgebung des Thorax mit wave-CAIPI

Doctoral thesis for a doctoral degree
at the Graduate School of Life Sciences,
Julius-Maximilians-Universität Würzburg,
Section Biomedicine

Submitted by
Julian Alexander Jürgen Richter
from
Bad Kissingen

Würzburg, 2020

cc BY NC

Submitted on: ____________________

Members of the Promotionskomitee:

Chairperson: ____________________________

Primary Supervisor: Prof. Dr. Herbert Köstler

Supervisor (Second): Prof. Dr. Laura Schreiber

Supervisor (Third): PD Dr. Peter Nordbeck

Supervisor (Fourth): PD Dr. Dr. Bernhard Petritsch

Date of Public Defense: ____________________

Date of Receipt of Certificates: ____________________

Wave-CAIPI for Accelerated Dynamic MRI of the Thorax

Contents

List of Figures 9

List of Tables 13

1 Introduction 15

1.1 Motivation 15

1.2 Outline 18

2 Non-Cartesian MR Data Acquisition 19

2.1 Sampling and Reconstruction 19

2.1.1 K-Space 19

2.1.2 Non-uniform Fourier Transform 21

2.1.3 Parallel Imaging 24

2.2 Wave-CAIPI k-space Trajectory 27

2.3 Gradient Correction 30

3 Wave-CAIPI for Dynamic 3D Lung MRI 35

3.1 Background 35

3.2 Methods 37

3.3 Results 46

3.4 Discussion 53

3.5 Conclusion 58

4 Wave-CAIPI for 4D Flow MRI of the Aorta 59

4.1 Background 59

4.2 Methods 62
4.3 Results 68
4.4 Discussion 87
4.5 Conclusion 93

5 Summary 95

6 Zusammenfassung 99

7 Bibliography 103

A Curriculum Vitae 117

B Publications 119

C Affidavit / Eidestattliche Erklärung 121

D Acknowledgments 123

List of Figures

2.1 Convolutional gridding in 2D 22
2.2 Kaiser-Bessel convolution kernel 23
2.3 Conjugate Gradient SENSE residual 26
2.4 Wave-CAIPI k-space sampling 28
2.5 Aliasing in Cartesian and wave-CAIPI acquisitions . . 29
2.6 Wave-CAIPI trajectory errors 31
2.7 GSTF-based gradient correction for wave-CAIPI 32
2.8 Autocalibration for gradient correction 34

3.1 Sampling pattern for self-gated 4D lung MRI with wave-CAIPI 38
3.2 DC-signal for respiratory self-gating 41
3.3 Cartesian and wave-CAIPI 4D lung examinations for different acquisition times 46
3.4 2-Minute 4D lung MRI with Cartesian and wave-CAIPI sampling 47
3.5 Quantitative image analysis of retrospectively accelerated 4D lung MRIs 48
3.6 Normalized mutual information as a function of acquisition time for Cartesian and wave-CAIPI sampling . . 49
3.7 PET/CT scans and 4D lung MRIs of a patient with squamous cell carcinoma in the lung 50
3.8 Phantom-based SNR assessment, simulating a 1-minute 4D lung MRI 51

3.9 Simulated in vivo g-factor 52

4.1 Representation of flow velocity encoding in phase contrast MRI 63
4.2 4D flow pulse sequence diagram with wave-CAIPI sampling 64
4.3 Prospective image-based respiratory gating 65
4.4 Comparison of different acceleration rates in wave-CAIPI 4D flow MRI and assessment of pixel-based velocity differences between $R = 2$ and $R = 6$ 69
4.5 Phase contrast MRIs for 4D flow acquisitions 70
4.6 Noise calculations in 6-fold accelerated 4D flow MRIs with wave-CAIPI and Cartesian sampling 71
4.7 Bar charts of uncertainties in flow parameters 72
4.8 Comparison of the measured flow rate for Cartesian and wave-CAIPI 4D flow acquisitions 74
4.9 Comparison of the measured flow per cycle for Cartesian and wave-CAIPI 4D flow acquisitions 75
4.10 Comparison of the measured peak velocity for Cartesian and wave-CAIPI 4D flow acquisitions 75
4.11 Comparison of the measured net average through-plane velocity for Cartesian and wave-CAIPI 4D flow acquisitions 76
4.12 Comparison of the measured flow rate for 2-fold and 6-fold accelerated 4D flow acquisitions 79
4.13 Comparison of the measured net flow for 2-fold and 6-fold accelerated 4D flow acquisitions 80
4.14 Comparison of the measured peak velocity for 2-fold and 6-fold accelerated 4D flow acquisitions 81

4.15 Comparison of the measured net average through-plane velocity for 2-fold and 6-fold accelerated 4D flow acquisitions 82
4.16 Streamline and particle traces visualizations of aortic blood flow 84
4.17 Velocity vector representations of aortic blood flow . . 85
4.18 4D flow visualization of a patient with aortic valve stenosis 86
4.19 Encoded and excited field of view 91

List of Tables

4.1 Discrepancies in flow parameters between 2-fold and 6-fold accelerated 4D flow MRIs, averaged over 10 healthy volunteers 73

4.2 Average differences in flow parameters between Cartesian and wave-CAIPI acquisitions for 10 healthy volunteers with assessment of statistical significance 76

4.3 Average differences in flow parameters between wave-CAIPI 4D flow acquisitions with 2-fold and 6-fold acceleration for 10 healthy volunteers with assessment of statistical significance 77

4.4 Average differences in flow parameters between Cartesian/2D-CAIPI 4D flow acquisitions with 2-fold and 6-fold acceleration for 10 healthy volunteers with assessment of statistical significance 78

4.5 4D flow examination of a patient with aortic valve stenosis 87

1 | Introduction

1.1 Motivation

Magnetic resonance imaging (MRI) is a valuable diagnostic imaging technique that, unlike Computed Tomography (CT) or conventional X-Ray examinations, does not require ionizing radiation. Another advantage of magnetic resonance (MR) is its superior soft-tissue contrast, compared to CT. For 3-dimensional spatial coverage, however, MR scans can be very time-consuming, especially for high-resolution or dynamic applications. Extensive scan times not only reduce patient comfort, but also increase the risk of involuntary patient motion, which ultimately degrades image quality. Furthermore, available time slots in clinical routine are very limited and lengthy scans decrease patient throughput.

Many techniques on the acceleration of MR scans have been developed and are usually based on utilizing additional information about the imaged object or about the MR signal receiver system, in order to reconstruct an image from an undersampled dataset. The most prominent example is parallel imaging – it uses the different spatial sensitivities of the multiple MR receiver coils for additional spatial encoding. In 1999, Pruessmann et al. presented SENSE (Sensitivity Encoding for Fast MRI) [1], a reconstruction algorithm for undersampled MR datasets that operates in image space. An algorithm operating in the k-space domain (GRAPPA: Generalized Autocalibrating Partially Parallel Acquisitions) was later introduced by Grisworld et al. [2]. Both these techniques require full sampling in a region, typically around the k-space center, which corresponds to a low-resolution image of the object. SENSE-based methods then estimate spatial sensitivity maps from the low-resolution images of the multiple receiver elements and use this knowledge to undo the pixel superposition of the aliasing effect. GRAPPA-based methods use the fully sampled k-space region to calculate a GRAPPA kernel, consisting of linear combinations of neighboring k-space locations in the different receiver coils. Missing k-space locations can then be calculated via convolution of the acquired k-space samples with the GRAPPA kernel.

Compressed Sensing (CS) [3, 4] approaches make use of the compressibility of MR images to reconstruct artifact-free images from an undersampled k-space. Exploiting correlations in spatial, temporal and/or flow-encoding directions, Compressed Sensing has proven efficient in various cardiac applications [5–9]. A drawback of any technique that applies a temporal model to dynamic data is, however, that due to possible smoothing effects, functional parameters may exhibit a lower temporal fidelity.

Apart from elaborated reconstruction techniques for undersampled MR data, the image acquisition can also be accelerated by using the gradient hardware more efficiently by means of non-Cartesian k-space trajectories. Conventional MR examinations are performed with the Cartesian trajectory, which has many advantages, such as ease of implementation and inherent robustness against gradient system imperfections [10]. However, other k-space trajectories may be better suited for specific applications. For example, the inherent signal averaging near the k-space center in radial acquisitions reduces motion artifacts in morphological and functional lung imaging [11–13]. Radial k-space trajectories also facilitate the use of respiratory self-gating, since the k-space center signal is measured in each readout and may be used for gating. Furthermore, non-Cartesian k-space trajectories may lead to improved parallel imaging reconstructions of undersampled MR images. Recently, the wave-CAIPI (CAIPIRINHA: Controlled Aliasing in Parallel Imaging Results in Higher Acceleration) technique was shown to be very efficient in highly undersampled volumetric acquisitions [14–19]. It enables parallel imaging reconstructions with considerably reduced noise enhancement, which is usually introduced in the final images.

While the utilization of non-Cartesian k-space trajectories can have a beneficial impact in parallel imaging reconstructions and may be less sensitive to motion artifacts, some challenges also arise. For example, off-resonance effects in spiral trajectories can lead to significant blurring [20, 21]. This effect becomes stronger, as the readout duration is increased. Moreover, significant distortions of non-Cartesian gradient waveforms arise due to gradient system imperfections [10, 22–24]. This leads to inaccuracies in the k-space trajectory and finally translates to severe image artifacts. As a consequence, methods for correcting gradient errors, such as the gradient system transfer function (GSTF) or autocalibration based on data consistency, are often required [10, 17, 22–24].

The aim of this work is to investigate the potential of the wave-CAIPI technique to accelerate two particularly lengthy applications: dynamic 3D lung MRI for radiotherapy treatment planning and 4D flow MRI for the assessment of flow alterations in heart diseases. In dynamic 3D lung MRI (4D lung MRI), several breathing states of the lung need to be resolved, in order to quantify respiration-induced tumor movement. Since a large field of view (FOV) needs to be covered with sufficient spatial and temporal resolution, long scan times arise. 4D flow applications are usually accompanied by extensive acquisition times, as a 3D volume must be encoded, the flow velocity needs to be encoded in three orthogonal directions and resolution of the cardiac cycle must be performed.

All in vivo studies presented in this work were approved by our institution's ethics committee and informed, written consent was obtained from each subject prior to the examination.

1.2 Outline

Chapter 2 elaborates on general aspects of MR image reconstruction and signal encoding. In that context, the pulse sequence design for the wave-CAIPI k-space trajectory is outlined and reconstruction techniques are introduced. Further, the gradient system transfer function and data-driven autocalibration are presented as methods to correct for gradient system imperfections. In Chapter 3, dynamic 3D lung imaging is introduced for radiotherapy treatment planning. The results of 4D lung MR scans, performed with wave-CAIPI and Cartesian sampling, are quantitatively compared. To assess performance gains by employing the wave-CAIPI sampling technique, image quality is quantified as a function of acquisition time. 4D flow MRIs of the aorta are presented in Chapter 4 for wave-CAIPI and Cartesian sampling and for different acceleration factors. The dependence of several flow parameters on the sampling scheme and on the acceleration factor is investigated. Furthermore, error rates in flow parameters are calculated to quantitatively compare the two sampling strategies. Finally, Chapter 5 summarizes the main findings of this work.

2 Non-Cartesian MR Data Acquisition

This chapter presents non-Cartesian k-space sampling and discusses advantages and challenges. A brief introduction of parallel imaging reconstructions for non-Cartesian k-space trajectories is given. The wave-CAIPI k-space trajectory is introduced in detail. For more background on MR signal generation and measurement, the interested reader is referred to relevant textbooks, e.g., the work by Bernstein et al. [25].

Parts of the presented content in this chapter, as well as in the following chapters, were previously published in *Magnetic Resonance in Medicine* by John Wiley & Sons, Inc., [26] under the Creative Commons BY-NC 4.0 License[1]. Figures that were replicated in this work (entirely, or in parts) are declared accordingly.

2.1 Sampling and Reconstruction

2.1.1 K-Space

In magnetic resonance imaging, the Fourier transform

$$\hat{A} = \mathcal{F} A \tag{2.1}$$

---

[1] https://creativecommons.org/licenses/by-nc/4.0/

of the imaged object A is sampled during the measurement, where $\mathcal{F}$ denotes the Fourier transformation operator, defined by

$$(\mathcal{F}A)(\vec{k}) = \int_{\mathbb{R}^3} A(\vec{r})e^{-2\pi\imath\vec{k}\vec{r}}d^3r \tag{2.2}$$

in continuous 3-dimensional space, where $\vec{k} = (k_x, k_y, k_z)$ are locations in Fourier space and $\vec{r} = (x, y, z)$ denotes the spatial position. In order to obtain an image $A(\vec{r})$ from the measured MR data $\hat{A}(\vec{k})$, an inverse Fourier transform must be performed:

$$\begin{aligned} A(\vec{r}) &= (\mathcal{F}^{-1}\hat{A})(\vec{r}) \\ &\overset{\text{(Eq. 2.1)}}{=} (\mathcal{F}^{-1}\mathcal{F}A)(\vec{r}) \\ &= \mathcal{F}^{-1}(\mathcal{F}A)(\vec{r}) \\ &\overset{\text{(Eq. 2.2)}}{=} \int_{\mathbb{C}^3} \hat{A}(\vec{k})e^{2\pi\imath\vec{k}\vec{r}}d^3k. \end{aligned} \tag{2.3}$$

As in reality, the MR signal is sampled with a finite sampling frequency, the Fourier space (*k-space*) is sampled only at discrete positions (i.e., only a finite set of Fourier coefficients is sampled). Furthermore, since the acquisition time in MR imaging is limited – due to signal decay and also for practical reasons – only a limited volume in Fourier space can be sampled. Therefore, the inverse Fourier transform in Eq. 2.3 can be discretized in the following way

$$\begin{aligned} A(\vec{r}) = \frac{1}{N} \sum_{n_x=0}^{N_x-1} \sum_{n_y=0}^{N_y-1} \sum_{n_z=0}^{N_z-1} & A(n_x\Delta k_x, n_y\Delta k_y, n_z\Delta k_z) \\ & e^{2\pi\imath(\frac{\Delta k_x n_x}{N_x}x + \frac{\Delta k_y n_y}{N_y}y + \frac{\Delta k_z n_z}{N_z}z)}, \end{aligned} \tag{2.4}$$

where for $i \in \{x, y, z\}$, N_i denotes the number of equidistant sample positions in direction i, $N = N_xN_yN_z$ and Δk_i is the distance between sample positions in direction i. Characteristics of the k-space sampling scheme impact the image which is then reconstructed. For instance, the distance between two adjacent k-space samples in direction x defines the encoded field of view in that direction:

$$\mathrm{FOV}_x = \frac{1}{\Delta k_x}. \tag{2.5}$$

Furthermore, the spatial resolution in the image is related to the maximum sampled frequency in k-space. For the x direction, the spatial resolution is given by

$$\Delta x = \frac{1}{2k_{\mathrm{max,x}}}. \tag{2.6}$$

Directly performing the discrete Fourier transform in Eq. 2.4 is an operation of $O(N^2)$ computational complexity, which can be very demanding for large sample sizes. A more efficient implementation of the discrete Fourier transform is the Fast Fourier Transform (FFT), which reduces the complexity to $O(N \log(N))$ [27].

2.1.2 Non-uniform Fourier Transform

While the Fourier transformation of MR data acquired with the standard Cartesian trajectory can be efficiently performed by a Fast Fourier Transformation, some extra steps need to be taken for non-Cartesian MR data. In 1991, Jackson et al. presented an efficient method to transform data that was acquired on non-Cartesian sampling positions to a regular Cartesian grid [28]. The method is called *convolutional gridding* and is comprised of a convolution of the non-Cartesian sampling positions with a short-ranged convolution kernel $b(k)$. After resampling the data on a Cartesian grid, the standard FFT can be applied. After the Fourier transformation, however, the image suffers from intensity errors, as the convolution with the kernel function $b(k)$ in k-space corresponds to a multiplication of the image with the Fourier transformation of the kernel $B(r) = \mathcal{F}b(k)$ in image space. Therefore, the image needs to be divided by the Fourier transformation of the convolution kernel. Care needs to be taken that $B(r)$ does not have zeros within the FOV of interest. A schematic convolution of non-Cartesian sampling positions with the convolution kernel is displayed in Fig. 2.1. As investigated by Jackson et al., the Kaiser-Bessel function

$$b(k) = \begin{cases} \frac{1}{W} I_0(\beta\sqrt{1-(2k/W)^2}) & k \leq W/2 \\ 0 & \text{otherwise} \end{cases} \tag{2.7}$$

serves as a suitable convolution kernel, where I_0 is the zeroth-order modified Bessel function of the first kind, W describes the width of the kernel and β is a scaling parameter. Fig. 2.2 displays the shape of an exemplary Kaiser-Bessel convolution kernel.

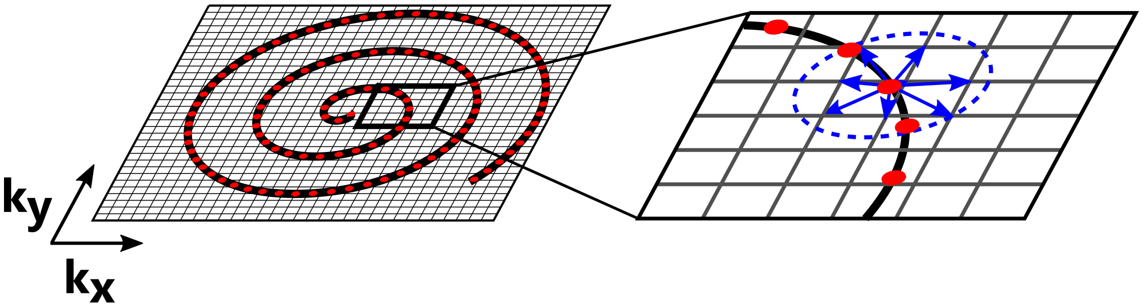

Figure 2.1: Resampling of a spiral trajectory in 2D k-space onto a Cartesian grid via convolutional gridding. Each data point on the non-Cartesian trajectory (red) is convolved with a finite kernel (blue dotted line).

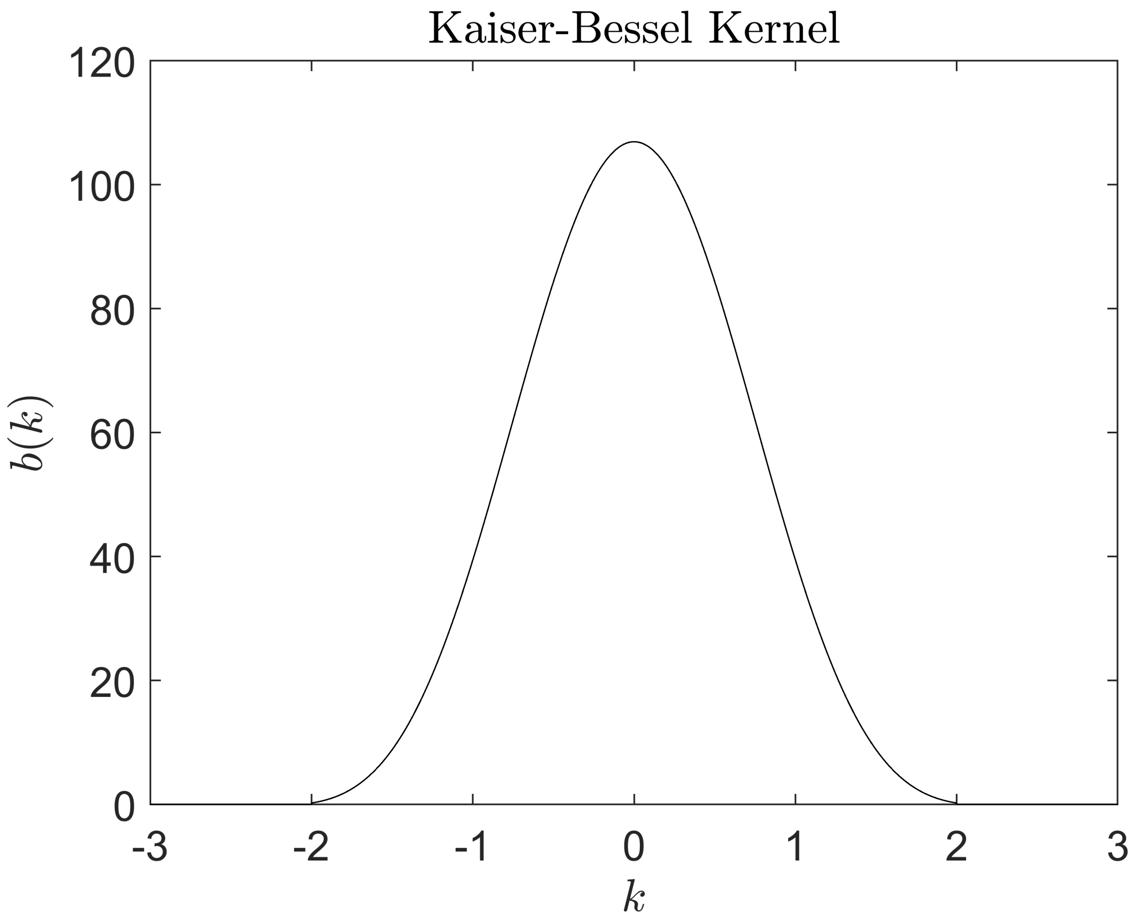

Figure 2.2: Kaiser-Bessel convolution kernel for $W = 4$ and $\beta = 8$.

2.1.3 Parallel Imaging

The image acquisition in magnetic resonance imaging can be accelerated by omitting readout lines in k-space, e.g., by measuring only every other phase encoding step in 2D imaging (acceleration factor $R = 2$). As a consequence, however, the distance between adjacent sampled k-space locations is increased by a factor of 2 in phase encoding direction. According to Eq. 2.5, the encoded field of view is thereby reduced by a factor of 2, leading to aliasing artifacts in the image. In order to remove the aliasing artifacts and obtain a full FOV image, parallel imaging algorithms, such as SENSE or GRAPPA, can be employed [1, 2, 29]. SENSE-based algorithms make use of the different spatial sensitivity profiles of the individual receiver coils for additional spatial encoding. GRAPPA, on the other hand, estimates correlations in neighboring k-space locations and among different receive channels to recover missing k-space samples.

In this work, a SENSE-based algorithm was chosen for the reconstruction of undersampled MR images. In $R = 2$-fold undersampled Cartesian MR images, for instance, aliasing leads to a superposition of pixels that are separated by a distance of FOV/2 in the undersampled direction. The SENSE reconstruction relies on the fact that pixel superposition is weighted by the spatial sensitivities of the individual receiver elements. If the spatial sensitivities of the respective receive channels are known, the superposition can be undone and the full FOV image can be recovered.

For the reconstruction of images acquired with non-Cartesian k-space trajectories, it is more efficient to perform the SENSE reconstruction iteratively, as introduced in [29]. To this end, the SENSE problem is solved with a Conjugate Gradient (CG) algorithm, minimizing a data consistency term in image space. A common challenge in iterative image reconstructions is the choice of a proper regularization or termination criterion. The number of iterations in an iterative SENSE reconstruction corresponds to a regularization parameter, dictating the compromise between the amplitude of undersampling artifacts and image noise [30]. In this work, the residual of the Conjugate Gradient algorithm r_{CG}, which is a measure of data consistency, was used as a stopping criterion. The algorithm was stopped when r_{CG} decreased beyond a pre-determined threshold. To this end, the actual image noise was estimated using the pseudo multiple replica approach [31]. Noise amplitudes and correlations between different channels were measured in a short pre-scan, using the same pulse sequence setup as for actual imaging, but omitting the excitation pulse. With the knowledge of noise amplitudes and correlations, a noise covariance matrix was calculated. The noise covariance matrix was then used to generate authentic, artificial noise samples (i.e., correct scaling and correlations across the receive channels). A fully sampled, noise-only k-space was thereby generated and, by performing a Fourier transform, a noise-only image was obtained. The noise level was calculated in the noise image, taking into account the sensitivity profiles of the individual receive channels:

$$r_{\mathrm{Noise}} = \sqrt{\sum_{i=1}^{N_{\mathrm{px}}} \left| \sum_{k=1}^{N_{\mathrm{ch}}} m_{ik} C_{ki}^{*} \right|^{2}}, \tag{2.8}$$

where N_{px} denotes the number of pixels, N_{ch} is the number of channels, m_{ik} is the value of pixel i in channel k and C^{*} is the complex conjugate spatial sensitivity of channel k at pixel i. Using the image noise level, the termination criterion of the Conjugate Gradient SENSE algorithm was defined as

$$r_{\mathrm{CG}} \leq c \cdot r_{\mathrm{Noise}}, \tag{2.9}$$

where c controls the compromise between noise level and residual undersampling artifacts. In this work, c was chosen to be in the range of [0.09, 0.7], depending on the application. A typical evolution of the CG residual is shown in Fig. 2.3, displaying also the termination threshold for the reconstruction of an undersampled 3D lung MRI examination.

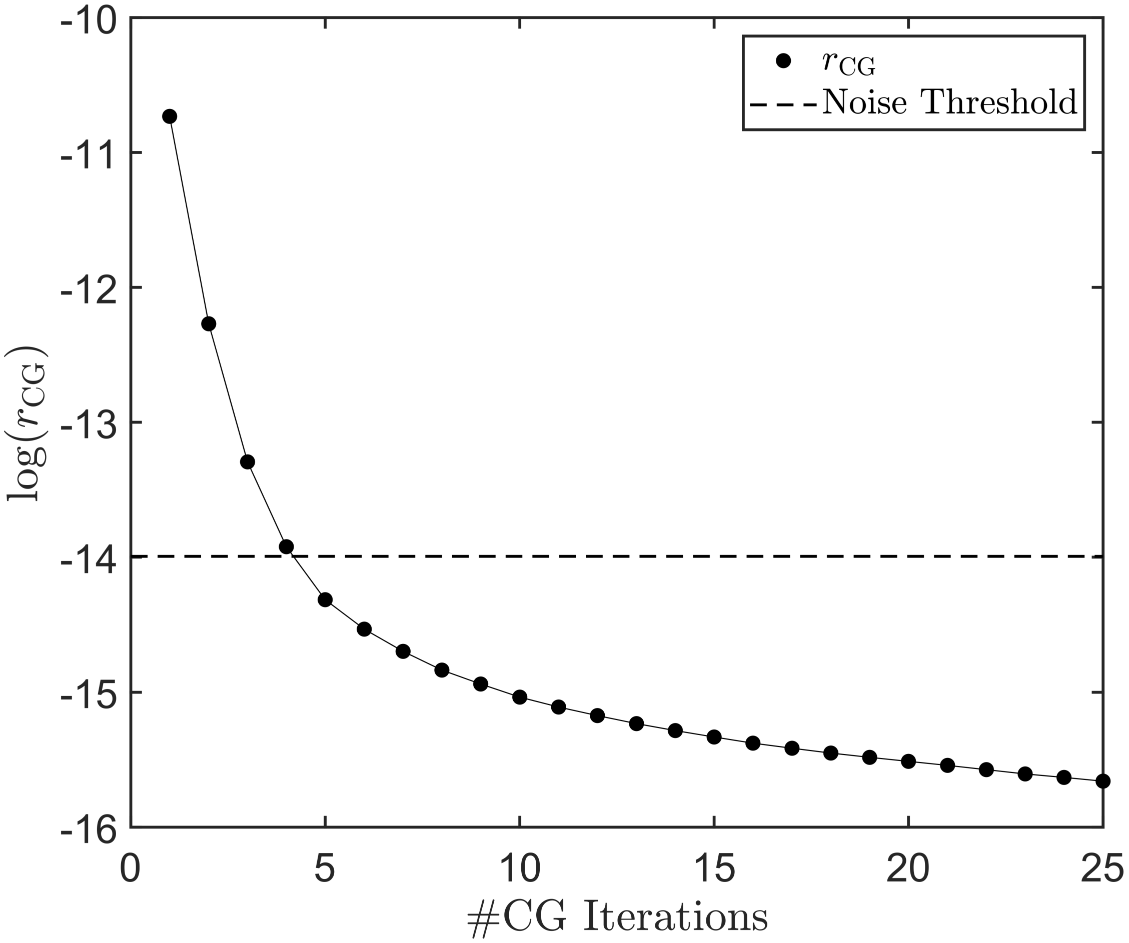

Figure 2.3: Residual r_{CG} of a Conjugate Gradient SENSE reconstruction after each iteration. The dashed line represents the noise threshold according to Eq. 2.9.

A drawback of parallel imaging reconstructions is an elevated noise level in the reconstructed images. In addition to the $\sqrt{R}$-fold loss in SNR for R-fold acceleration, which is due to the smaller acquisition time, a noise penalty related to the ill-conditioning of the reconstruction problem arises [31]. This noise amplification depends on the level of undersampling and the receive coil setup (number of channels, location of receive elements and sensitivity profiles). The latter influence is quantified by the geometry factor g, often abbreviated as the g-factor. The g-factor can be calculated from the estimated SNR in accelerated and fully sampled acquisitions, i.e., by using the pseudo multiple replica approach [31]:

$$g = \frac{\mathrm{SNR}_{\mathrm{full}}}{\mathrm{SNR}_{\mathrm{acc}}\sqrt{R}}, \tag{2.10}$$

where $\mathrm{SNR}_{\mathrm{full}}$ and $\mathrm{SNR}_{\mathrm{acc}}$ denote the SNR of fully sampled and accelerated acquisitions, respectively. The g-factor is calculated on a pixel-by-pixel basis.

2.2 Wave-CAIPI k-space Trajectory

The wave-CAIPI technique was recently introduced for optimized volumetric acquisitions [14–19], enabling parallel imaging reconstructions of undersampled datasets with reduced noise enhancement. The wave-CAIPI technique applies sinusoidal gradient waves on the two phase encoding directions during readout (cf. Fig. 2.4a). The gradient wave oscillations are shifted with respect to one another by a phase difference of $\pi/2$. The k-space trajectory results from the time integral of the gradient waveforms

$$\vec{k}(t) = \gamma \int_0^t \vec{G}(t')dt', \tag{2.11}$$

where $\vec{k} = (k_x, k_y, k_z)$ is the k-space location, t is the time, $\vec{G} = (G_x, G_y, G_z)$ is the magnetic field gradient vector and γ denotes the gyromagnetic ratio for protons. In the present case, the trajectory then consists of helix-shaped readout lines in 3D k-space, as shown in Fig. 2.4b. This wave encoding strategy is combined with a 2D-CAIPI undersampling pattern, to make better use of receive coil sensitivity variations [32, 33].

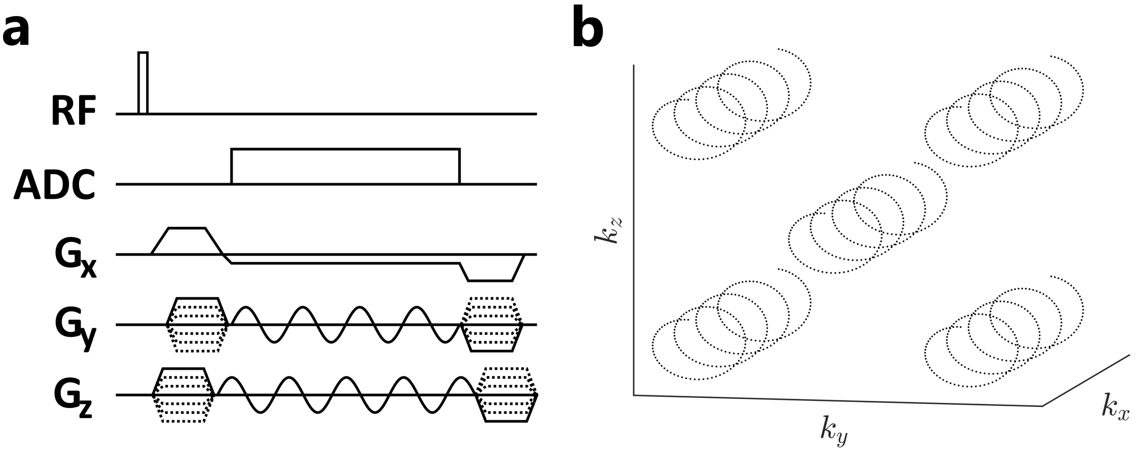

Figure 2.4: (a) Pulse sequence diagram of a gradient echo sequence with wave-CAIPI sampling. (b) Wave-CAIPI k-space trajectory, consisting of helix-shaped readout lines. Previously published in [26] under the CC BY-NC 4.0 license (modified).

The wave-CAIPI sampling leads to a more homogeneous distribution of missing k-space locations in the case of undersampling, compared to the Cartesian trajectory. The omission of readout lines leads to undersampling in the phase encoding, as well as in the frequency encoding direction. As a result, aliasing artifacts in the image space are distributed in all three spatial dimensions. Therefore, coil sensitivity variations can be exploited also in the frequency encoding direction, leading to overall better parallel imaging reconstructions. In contrast to that, aliasing only takes place in the phase encoding directions for 3D Cartesian sampling and coil sensitivity variations are only used in two dimensions.

To demonstrate the voxel-spreading properties of the wave-CAIPI k-space trajectory, the appearance of undersampling artifacts for wave-CAIPI are presented in Fig. 2.5 for an acceleration rate of $R = 2$ in the anterior-posterior direction (phase encoded).

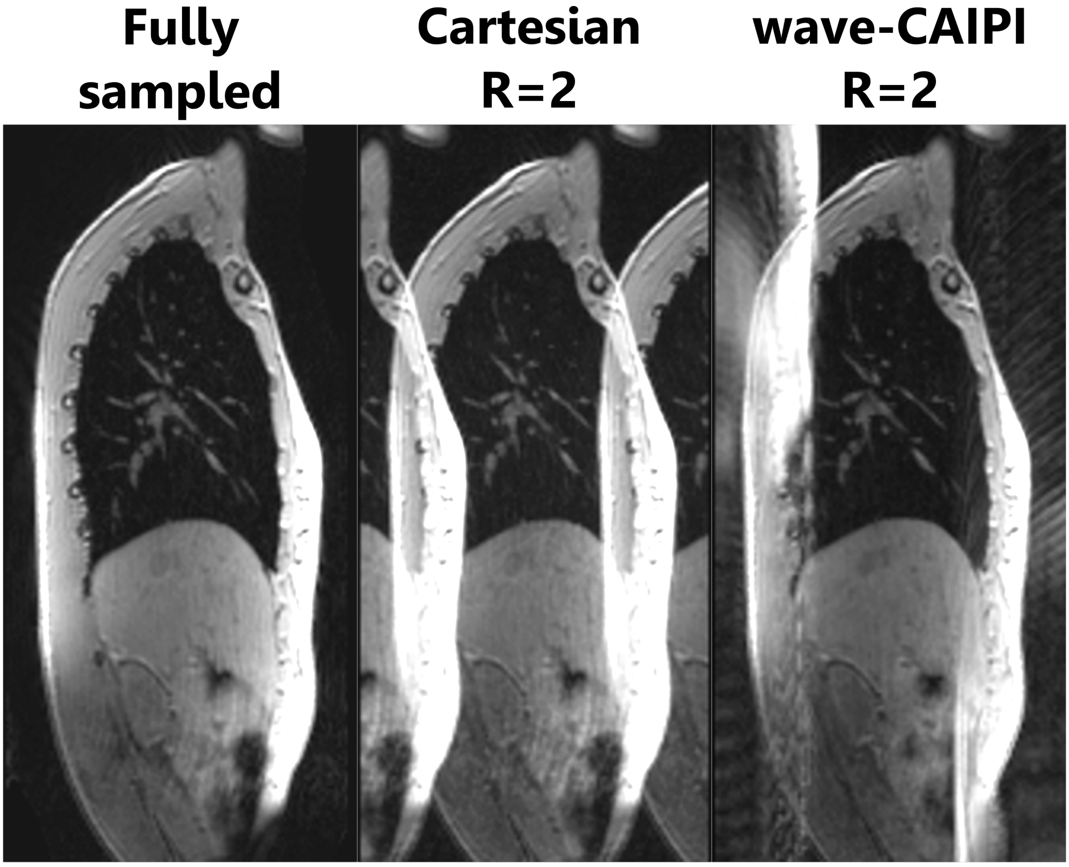
Fully sampled
Cartesian R=2
wave-CAIPI R=2

Figure 2.5: Appearance of undersampling artifacts in 3D Cartesian and wave-CAIPI acquisitions. The images are 2-fold accelerated in anterior-posterior direction. The wave-CAIPI technique spreads undersampling artifacts also in the frequency encoding direction (head-feet).

2.3 Gradient Correction

A disadvantage of non-Cartesian k-space trajectories is their susceptibility to imperfections in the gradient system [10, 22–24]. The waveforms that are actually played out by the MR scanner usually differ from the nominal input gradients. In case of the wave-CAIPI method, the real sinusoidal gradient waves are distorted and differ from the nominal gradient oscillations by time-delays and magnitude alterations, which depend on the frequency of the oscillation. Differences between the theoretical input gradient and the gradient that is actually played out lead to errors in the k-space trajectory, as displayed in Fig. 2.6. Severe image artifacts arise from k-space trajectory inaccuracies. Thus, a correction method that accounts for gradient distortions is required, in order to avoid artifacts.

The gradient system behavior, including imperfections, can be characterized by means of the gradient system transfer function (GSTF) [10, 22–24]. The scanner specific GSTF can be determined in phantom measurements. For this purpose, the phase evolution of the MR signal is measured in two parallel slices, while several triangular input gradients are applied on the gradient axis perpendicular to the excited slice. From the phase information in two slices, the gradient that is actually played out can be calculated and compared to the nominal input. Using this method, three separate measurements need to be performed, in order to characterize the system behavior in all three gradient axes. The GSTF represents a general, linear model for gradient distortions and can be used to estimate the alterations of arbitrary gradient waves, in order to account for them during the image reconstruction. In this work, gradient correction was performed by only using the linear self-terms of the GSTF. The effect of gradient inaccuracies on the image and the corresponding correction is demonstrated in Fig. 2.7.

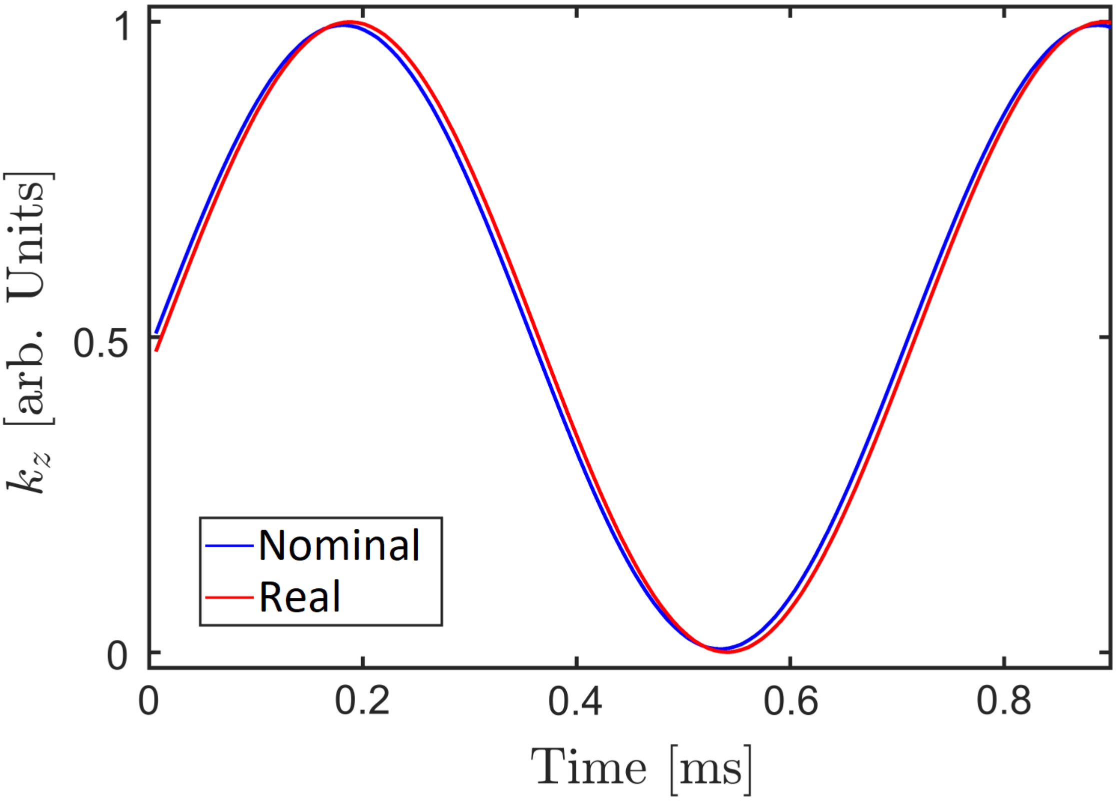

Figure 2.6: Differences between nominal and real k-space trajectory for wave-CAIPI sampling on the Z gradient axis. Previously published in [26] under the CC BY-NC 4.0 license (modified).

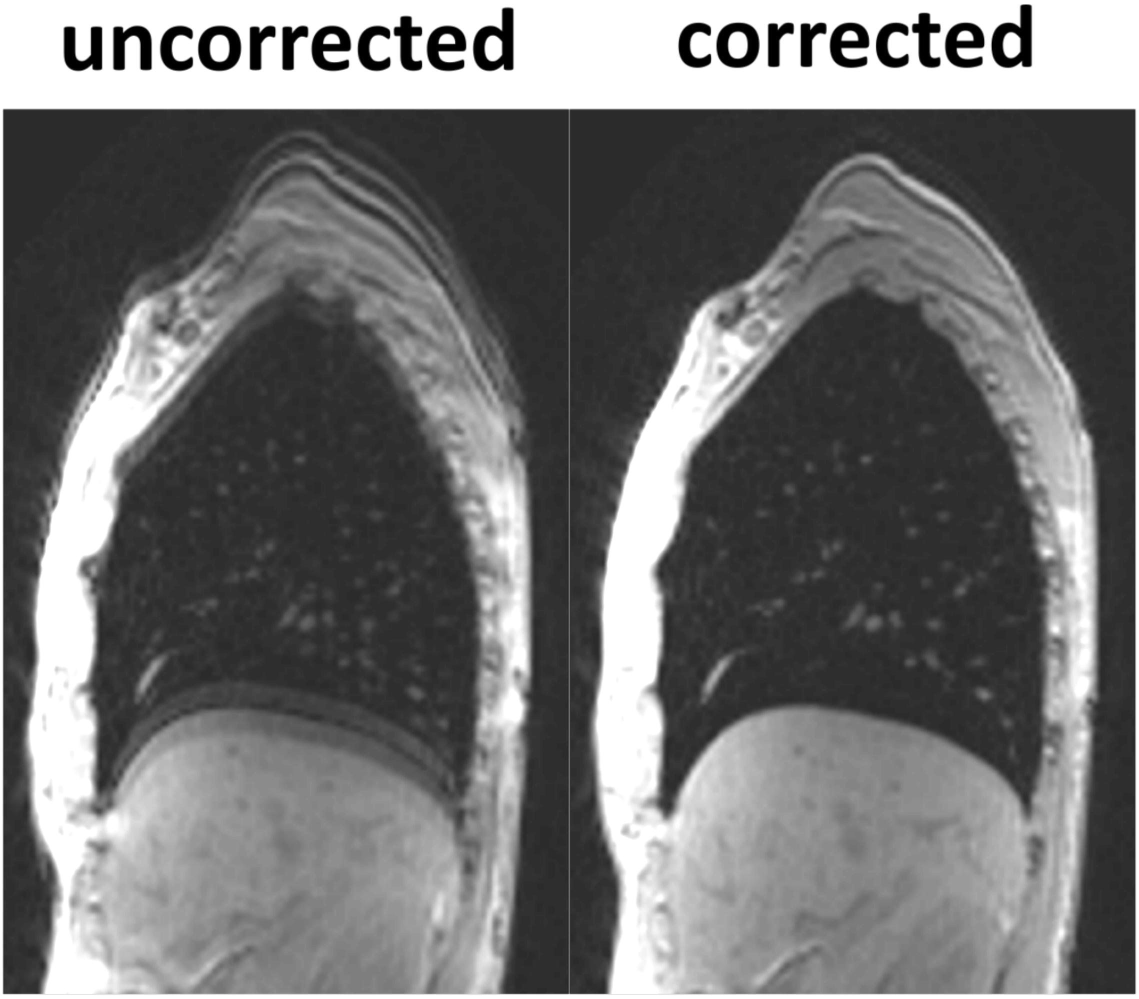

Figure 2.7: Impact of the GSTF-based gradient correction in a wave-CAIPI acquisition of the lung. Trajectory errors in the left image lead to image artifacts. The right image shows that GSTF-correction removes these artifacts efficiently. Previously published in [26] under the CC BY-NC 4.0 license (modified).

Gradient correction could also be performed by minimizing a data consistency term, as was suggested recently for the wave-CAIPI k-space trajectory [15]. There, the authors relate gradient distortions to a small set of correction parameters. The gradient wave oscillations of the wave-CAIPI can be sparsely described in the Fourier domain, since the oscillation contains only a single frequency. In the presented model, only the peak position and its neighboring positions in the frequency spectrum are subjected to the optimization problem, resulting in 3 complex correction parameters per gradient axis. The correction parameters are varied and data consistency in a reduced SENSE reconstruction model is used to guide the algorithm to the set of correction parameters that best describes the acquired data.

A similar approach is to consider one delay and one magnitude alteration parameter per gradient axis and calculate the data consistency term as a function of these parameters. Thereby, the gradient correction model consists of only 2 real correction parameters per gradient axis, similar to the linear self-term GSTF approach. In Fig. 2.8, the L_1-norm of the Conjugate Gradient SENSE residual r_{CG} is shown as a function of the delay parameter of the Y-gradient axis. The minimum in $L_1(r_{\mathrm{CG}})$ is located near the GSTF-predicted value of $5.2\,\mu$s.

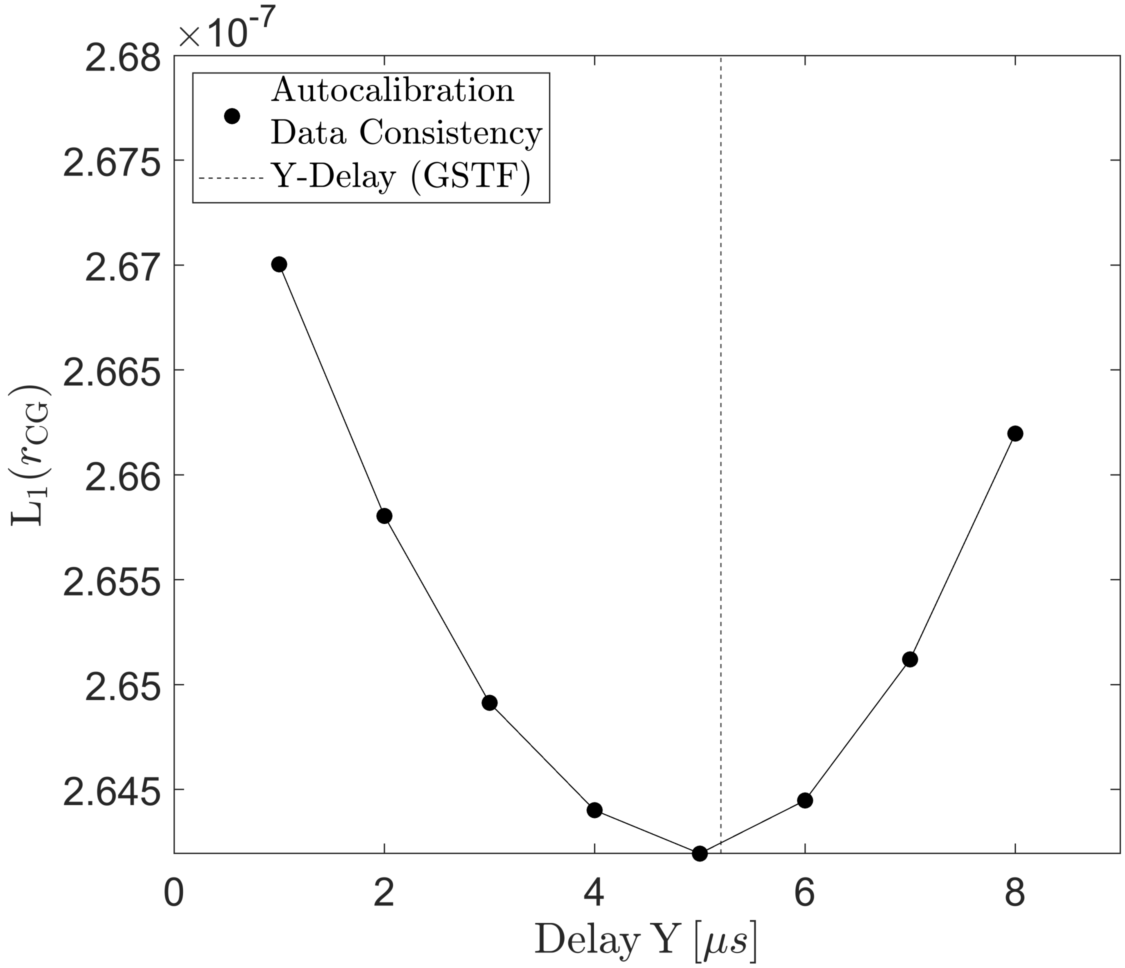

Figure 2.8: Autocalibration method to estimate the gradient delay of the Y-gradient axis in a wave-CAIPI acquisition. The residual of the iterative SENSE reconstruction is used to find the delay value that best represents the measured data, quantified in terms of data consistency. The minimum of $L_1(r_{\mathrm{CG}})$ indicates a suitable value for the gradient delay and compares well to the GSTF-based estimation (dashed vertical line).

3 | Wave-CAIPI for Dynamic 3D Lung MRI

This chapter presents the application of the wave-CAIPI sampling technique to respiratory self-gated dynamic 3D lung MRI (4D lung MRI) during free breathing, for the purpose of radiotherapy treatment planning. The technique is tested on 6 volunteers (5 healthy volunteers, 1 patient) and is compared to 4D lung MRI with standard Cartesian sampling.

The majority of the presented findings was previously published in *Magnetic Resonance in Medicine* by John Wiley & Sons, Inc., [26] under the Creative Commons BY-NC 4.0 License[1]. Figures that were replicated in this work (entirely, or in parts) are declared accordingly.

3.1 Background

Due to respiration and cardiac motion, moving organs, such as the lungs are particularly challenging to image with MR, since the acquisition is typically impaired by motion artifacts and blurring. Furthermore, the inherently low proton density and the fast T_2^* decay of lung tissue complicates lung imaging, as the signal is weak. In order to eliminate motion artifacts arising from respiration, a breathhold examination can be performed. Such an approach, however, requires patient compliance and severely restricts the time frame available for the acquisition. Breathhold examinations can be increasingly challenging for patients with a limited breathhold capability.

---

[1] https://creativecommons.org/licenses/by-nc/4.0/

Respiratory motion can also be accounted for by means of image-based gating methods [34, 35], or by employing additional hardware, such as respiration belts, for instance [36]. A respiration belt, however, requires additional time for setup and may reduce patient comfort. An emerging hardware-based approach is the Pilot Tone technique [37, 38], which uses an additional RF transmitter to capture respiration-induced tissue displacement.

Another approach is respiratory self-gating [39–41]. Thereby, the breathing motion is estimated directly from the acquired MR data. To this end, signal variations in the center of k-space may be used as a respiratory navigator signal. A small increase in acquisition time has to be spent for acquiring the center of k-space repeatedly, for Cartesian, as well as wave-CAIPI pulse sequences. In contrast to that, some k-space trajectories, such as the 3D radial trajectory, inherently measure the center of k-space in each T_R [13]. Only minor modifications to existing MR pulse sequences are required to implement self-gating. As long scan times increase the risk of involuntary patient motion that degrades the image quality, the acquisition time of lung examinations should be as short as possible, even with respiratory self-gating.

4D morphological lung imaging with respiratory self-gating has previously been reported in the context of radiotherapy treatment planning [40, 42, 43], for the purpose of quantifying respiration-induced tumor displacement. If tumor displacement during respiration is unknown, large safety margins around the tumor need to be defined, in order to guarantee therapy with the prescribed dose. By determining tumor displacement, optimized dose distributions may be calculated to minimize radiation exposure of adjacent organs at risk.

The previous works [40,42,43] used the Cartesian k-space trajectory for acquiring the MR data. In the present work, the wave-CAIPI k-space trajectory was used to further reduce the acquisition time, while maintaining diagnostic image quality. The wave-CAIPI is usually employed on the basis of a regular, 2D-CAIPI undersampling pattern, as presented in Sec. 2.2. In a study investigating motion-correction for abdominal imaging with wave-CAIPI, a variable density sampling and radial view ordering (VDRad) undersampling pattern was chosen [19, 44]. In this work, the phase encoding scheme was randomized using a non-uniform density distribution, leading to random sampling patterns after respiratory gating.

High quality, dynamic 3D images of the human lung were acquired during free breathing using a randomized self-gated FLASH pulse sequence with wave encoding. Wave-CAIPI images were compared to Cartesian images for different acquisition times and image quality was quantitatively assessed by means of similarity measures, as well as g-factor and SNR-calculations.

3.2 Methods

Setup

The wave-CAIPI k-space trajectory was integrated in a 3D gradient echo pulse sequence, by applying sinusoidal gradient oscillations on both phase encoding axes during readout (cf. Sec. 2.2). For this study, a fixed number of complete wave cycles $N_{\text{wave}} = 4$ and a maximum gradient wave amplitude of $A_{\text{wave}} = 6\,\text{mT/m}$ was chosen. The ADC (Analog-Digital Converter) was opened for a short period of time after the non-selective RF excitation pulse. Thereby, the center of k-space ("DC-Signal") was acquired in each T_R and used as a respiratory navigator signal for retrospective self-gating. A schematic pulse sequence diagram is displayed in Fig. 3.1a.

The phase encoding scheme was randomized using a non-uniform density distribution σ_{PE} with increased sampling probability near the

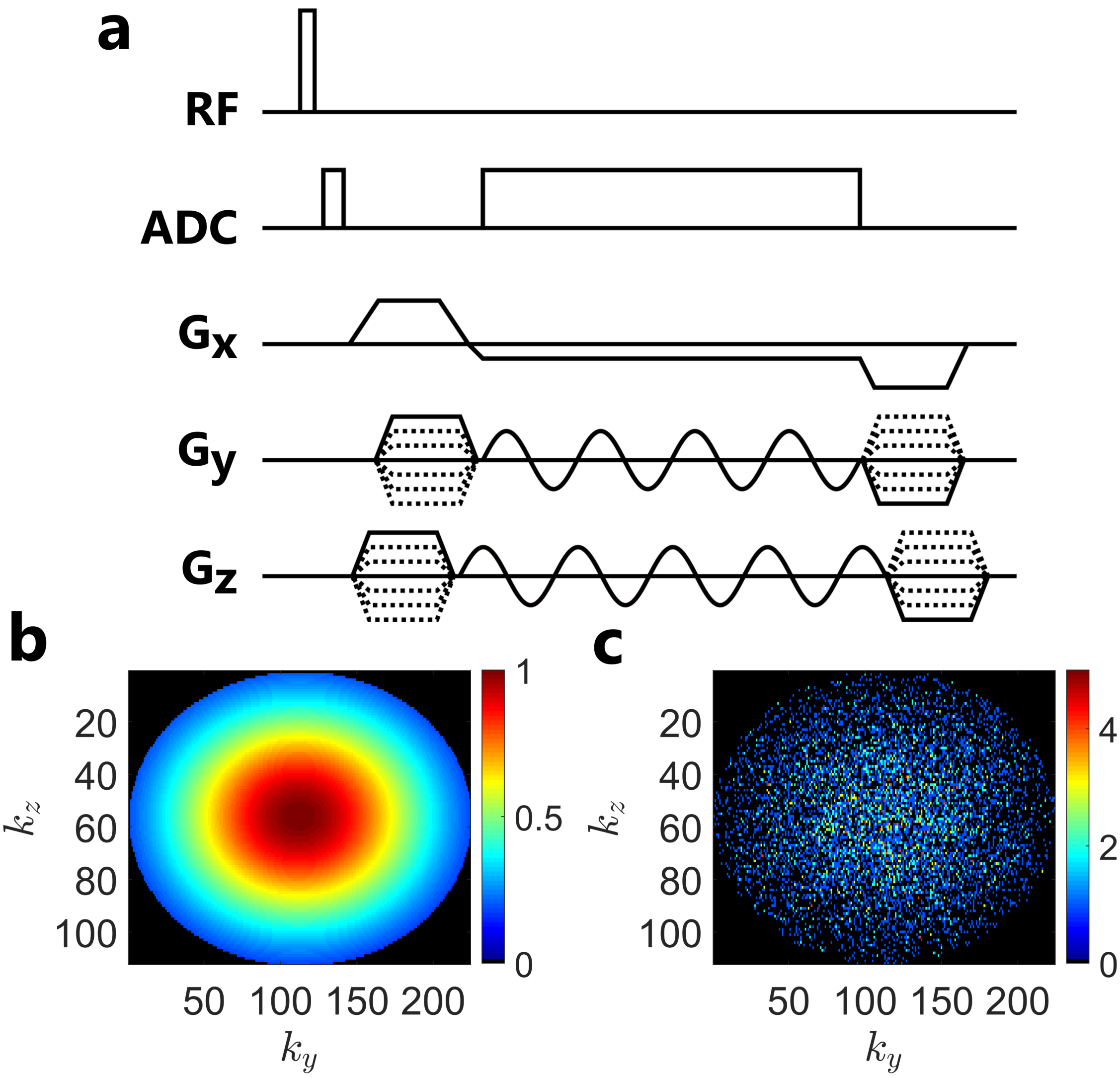

Figure 3.1: (a) Pulse sequence diagram of a self-gated 3D gradient echo sequence with wave-CAIPI sampling. The ADC acquires the DC-signal directly after the non-selective excitation pulse. (b) Nominal density distribution used for randomization of the phase encoding order. (c) Typical sampling pattern of a 3-minute lung scan after retrospective gating, using the density distribution in (b). Previously published in [26] under the CC BY-NC 4.0 license (modified).

k-space center. Thereby, synchronization between phase encoding and respiration is prevented and large gaps in k-space after retrospective self-gating are avoided, especially in the k-space center [42, 43]. To this end, 2D pseudo-random numbers within the range of $([0,1],[0,1])$ were generated using a Mersenne-Twister algorithm [45] (implemented in the C++ standard library). The random numbers were distributed according to a normal distribution with zero mean and a width of $w = 0.3$:

$$\sigma_{\mathrm{PE}}(k_y, k_z) = \exp\Big(-\frac{\sqrt{k_y^2 + k_z^2}}{2w}\Big). \tag{3.1}$$

The nominal density distribution in k-space is displayed in Fig. 3.1b. A typical sampling pattern of a 3-minute lung scan after retrospective self-gating is shown in Fig. 3.1c. The figure shows moderate undersampling near the k-space center and increasing gaps towards the k-space periphery.

In all volunteer and patient examinations, wave-CAIPI and Cartesian reference scans were performed. An identical set of pulse sequence parameters was chosen for both sampling schemes (except for the wave-CAIPI specific parameters A_{wave} and N_{wave}). Images were acquired with a k-space matrix of size $224 \times 224 \times (112-144)$ and an isotropic resolution of 2.23 mm. Further sequence parameters were: FOV $= 500 \times 500 \times (250-321)\,\mathrm{mm}^3$, repetition time $T_R = 4.8\,\mathrm{ms}$, echo time $T_E = 1.9\,\mathrm{ms}$, flip angle $\varphi = 5°$, readout bandwidth BW $= 350\,\mathrm{Hz/px}$, which corresponds to a readout time of 2.86 ms. Frequency encoding was performed in head-feet direction. The examinations were performed using an 18 channel body coil array, positioned on top of the volunteers, and a spine coil array (12–16 channels activated) that was integrated in the scanner table, resulting in a total of 30–34 receiver channels.

In order to compare the image quality of wave-CAIPI and Cartesian 4D lung MR scans quantitatively, five healthy volunteers were examined with both sampling schemes. Furthermore, one patient (male, 65 years old) with known squamous cell carcinoma in the lung was examined and respiration-induced tumor movement was assessed. The total acquisition time for one 4D lung scan was set to be $T_{\mathrm{Acq}} = (08{:}01\text{–}10{:}18)$ min for wave-CAIPI and Cartesian sampling. This acquisition time lead to a moderate undersampling rate in the self-gated images ($R \approx 1.5$), which was considered to provide good reference images for the subsequent comparison to accelerated images. A low-resolution Cartesian calibration scan with increased FOV in the coronal plane was performed for the calculation of coil sensitivity maps.

All examinations were performed on a 3 Tesla clinical MR scanner (MAGNETOM Prisma$^{\mathrm{fit}}$, Siemens Healthcare, Erlangen, Germany).

Respiratory Self-Gating and Image Reconstruction

For both wave-CAIPI and Cartesian 4D lung scans, before image reconstruction, the series of readouts that was acquired in random order needed to be sorted into different breathing phases. Therefore, the DC-signal that was acquired in each T_R served as a respiratory navigator signal [39–41]. In the absence of spatial encoding, the signal is proportional to the total amount of protons and the spatial coil sensitivity profiles of the respective receiver elements. Hence, by manually selecting a receive coil near the lung/liver interface, periodic variations in the DC-signal can be associated with respiration, since tissue (liver) is moving in and out of the range of sensitivity of the respective coil. The DC-signal was band-pass filtered, in order to eliminate signal variations due to cardiac motion and to smooth the signal. A typical self-gating signal, after filtering, is presented in Fig. 3.2 for a volunteer examination. The acquired data was distributed into 8 breathing phases that partly overlap. A requirement in the distribution algo-

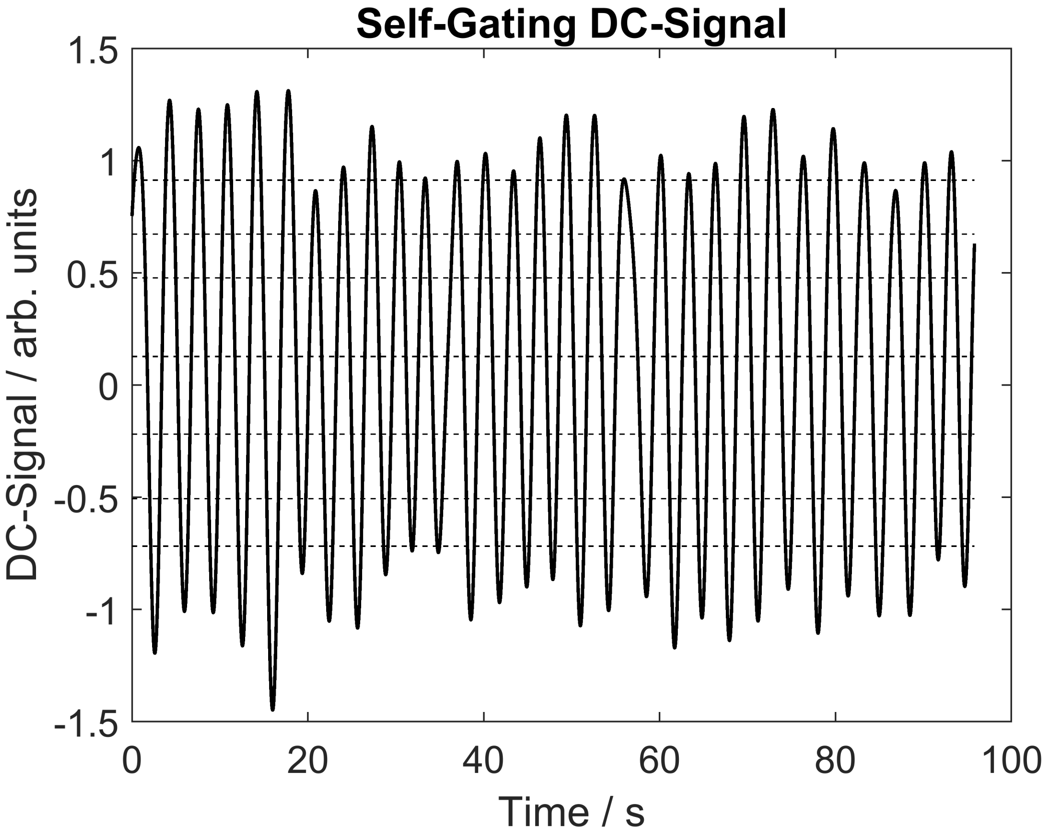

Figure 3.2: Self-gating signal from a volunteer examination (after band-pass filtering). Dashed lines represent the separation of the acquired data into 8 different breathing phases. Adjacent breathing phases overlap to a certain degree (not displayed). Previously published in [26] under the CC BY-NC 4.0 license.

rithm was that all breathing states contain a similar amount of data, in order to ensure that a sufficient amount of data is available in all breathing states for a stable parallel imaging reconstruction. For the purpose of reaching a steady state DC-signal, the first 2500 T_Rs were discarded prior to respiratory gating.

Gradient system imperfections were taken into account in retrospective. During the reconstruction, the k-space trajectory was corrected using the gradient system transfer function that was presented in Sec. 2.3.

The individual breathing states were reconstructed with an iterative Conjugate Gradient (CG) SENSE approach [1,28,29]. Sensitivity maps were estimated using an ESPIRiT calibration algorithm [46], as implemented in the Berkeley Advanced Reconstruction Toolbox (BART) [47]. Specifically for the comparison of two different MR imaging techniques, a suitable, objective selection of regularization parameters – in this case, the number of CG SENSE iterations – is required. To this end, the image noise level was estimated and the termination criterion developed in Sec. 2.1.3 was employed. For the in vivo examinations, the free parameter c in Eq. 2.9 was chosen to be in the range of 0.3–0.5. For phantom-based SNR calculations, $c = 0.3$ was chosen. For each volunteer, the same value of c was chosen for the wave-CAIPI and Cartesian reconstructions.

Quantitative Image Analysis

The initially acquired wave-CAIPI and Cartesian 4D lung MRIs (T_{Acq} = (08:01–10:18) min) were retrospectively accelerated by discarding measured data at the end of the respective scans. For different scan time reductions (down to 01:00 min), the image quality was quantified in terms of similarity to the reference scan. The normalized mutual information (NMI) and the root-mean-square error (RMSE) were calculated for each breathing state as a function of acquisition time and used to quantify image similarity between retrospectively accelerated acquisitions and their respective references. The normalized mutual information of two discrete variables X and Y is defined as

$$\mathrm{NMI}(X,Y) = \frac{I(X,Y)}{\sqrt{H(X)H(Y)}}, \tag{3.2}$$

where $I(X,Y)$ denotes the mutual information and $H(X)$, $H(Y)$ is the Shannon entropy of X and Y, respectively. The Shannon entropy is calculated as

$$H(X) = -\sum_{i=0}^{N_{\mathrm{px}}-1} X_i \log(X_i), \tag{3.3}$$

where X_i describes individual observations of X (here: pixels in an image) and N_{px} is the total number of pixels. The joint entropy is calculated accordingly:

$$H(X,Y) = -\sum_{i=0}^{N_{\mathrm{px}}-1} X_i Y_i \log(X_i Y_i). \tag{3.4}$$

The mutual information $I(X,Y)$ is defined as

$$I(X,Y) = H(X) + H(Y) - H(X,Y), \tag{3.5}$$

therefore, Eq. 3.2 can be expressed as

$$\begin{align}
\mathrm{NMI}(X,Y) &= \frac{I(X,Y)}{\sqrt{H(X)H(Y)}} \tag{3.6}\\
&= \frac{H(X) + H(Y) - H(X,Y)}{\sqrt{H(X)H(Y)}} \tag{3.7}\\
&= \frac{-\sum_{i=0}^{N_{\mathrm{px}}-1} \Big(X_i \log(X_i) + Y_i \log(Y_i) - X_i Y_i \log(X_i Y_i) \Big)}{\sqrt{\sum_{i,j=0}^{N_{\mathrm{px}}-1} X_i Y_j \log(X_i) \log(Y_j)}}. \tag{3.8}
\end{align}$$

The root-mean-square error is defined as

$$\mathrm{RMSE}(X, Y) = \sqrt{\frac{1}{N_{\mathrm{px}}} \sum_{i=0}^{N_{\mathrm{px}}-1} (X_i - Y_i)^2}. \tag{3.9}$$

The NMI describes the amount of information that can be obtained about one variable X by only measuring the variable Y. Hence, it presents a suitable similarity measure to compare various accelerated images to their respective reference. The initial 4D lung scan (i.e., without retrospective scan time reduction) can be used as a reference set to evaluate the image quality of accelerated scans. This approach requires that the initially determined gating windows are kept fixed for all accelerated datasets. Otherwise, changes in the breathing phase could lead to corruptions in the image similarity measure. Additionally, the root-mean-square error between the accelerated images and the reference was calculated to capture and quantify discrepancies.

The SNR ratio, i.e., the ratio

$$r_{\mathrm{SNR}} = \frac{\mathrm{SNR}_{\mathrm{wave-CAIPI}}}{\mathrm{SNR}_{\mathrm{Cartesian}}} \tag{3.10}$$

was estimated in accelerated wave-CAIPI and Cartesian phantom experiments on a pixel-by-pixel basis, using the pseudo multiple replica approach [31] (c.f. also Sec. 2.1.3). For this purpose, 100 reconstructions of the phantom data were performed, each with additional, properly correlated, artificial noise. The phantom experiment was performed with the same setup as for in vivo imaging. The undersampling pattern was designed to mimic a k-space sampling pattern of a 1-minute 4D lung MRI after applying respiratory gating (fraction of missing k-space lines $\approx$ 92%). The phantom consisted of a combination of two canisters, filled with water solutions of NaCl and $\mathrm{NaH_2PO_4} \cdot 2\mathrm{H_2O}$, respectively. The canisters were positioned in the MR scanner, such that typical torso geometries were simulated. The chosen phantom is not representative of actual lung tissue, regarding the relaxation times T_1, T_2 and proton density. Therefore, the individual SNR measurements may not correspond to the SNR in actual in vivo examinations. However, the ratio of two SNR measurements (one for Cartesian and one for wave-CAIPI) is not affected by relaxation parameters or proton density and therefore serves as a suitable measure to quantify the *relative SNR*.

The SNR calculation was performed on phantom data, rather than in vivo measurements, since the undersampling pattern of in vivo examinations is unpredictable with respiratory self-gating. In the presented case, acquisitions of the phantom were performed with wave-CAIPI and Cartesian sampling, using the same undersampling pattern. Thereby, any possible effects arising from different sampling patterns are avoided and a quantitative comparison can be performed on a pixel-by-pixel basis – this is not possible for in vivo examinations. Furthermore, as the ratio r_{SNR} is calculated as the quotient of two separate datasets on a pixel-by-pixel level, anatomical changes (different breathing phases or other, involuntary motion) between the two in vivo scans could influence the SNR ratio.

G-factor maps were calculated for 2-minute 4D lung MRIs with wave-CAIPI and Cartesian sampling. For suitable comparison, equal sampling patterns for wave-CAIPI and Cartesian sampling were simulated in the following way: The initially acquired dataset (i.e., without retrospective scan time reduction, scan time $\sim$ 8 minutes) were reconstructed, using the iterative Conjugate Gradient SENSE method. The resulting images, free of undersampling artifacts, were then re-sampled to the respective trajectory, thereby simulating a fully sampled acquisition. This artificially fully sampled dataset was then undersampled, using a fixed undersampling pattern. G-factor maps were then calculated using the pseudo multiple replica method [31] and were used to identify regions of increased noise enhancement in the in vivo images.

3.3 Results

The gradient system transfer function could be successfully employed to eliminate artifacts arising from imperfections in the gradient system. An exemplary image with and without gradient correction is shown in Sec. 2.3, Fig. 2.7, comparing a sagittal slice from a wave-CAIPI scan.

Fig. 3.3 compares the results of 4D lung MRIs with Cartesian and wave-CAIPI sampling for different retrospective scan time reductions. For a long acquisition time of 08:01 minutes, both sampling schemes result in good image quality. However, as the acquisition time is decreased, the Cartesian images start to exhibit severe residual undersampling artifacts, whereas the artifact level is reduced in the wave-CAIPI case. This effect is most prominent for the 1-minute scan. In Fig. 3.4, the 2-minute Cartesian scan is compared to the 2-minute wave-CAIPI scan in three different orientations. Some residual undersampling artifacts remain in the Cartesian images.

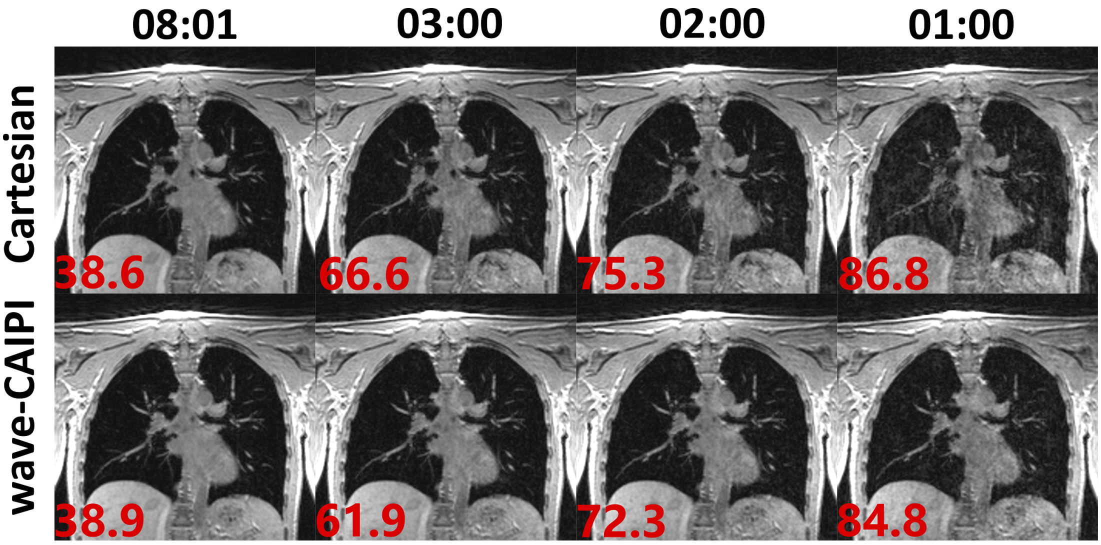

Figure 3.3: Results of 4D lung MRIs with Cartesian (top row) and wave-CAIPI sampling (lower row) for different acquisition times. As the acquisition time is decreased, severe artifacts arise in the Cartesian images. The red numbers in the lower left corners denote the percentage of missing k-space lines in the respective images. Previously published in [26] under the CC BY-NC 4.0 license.

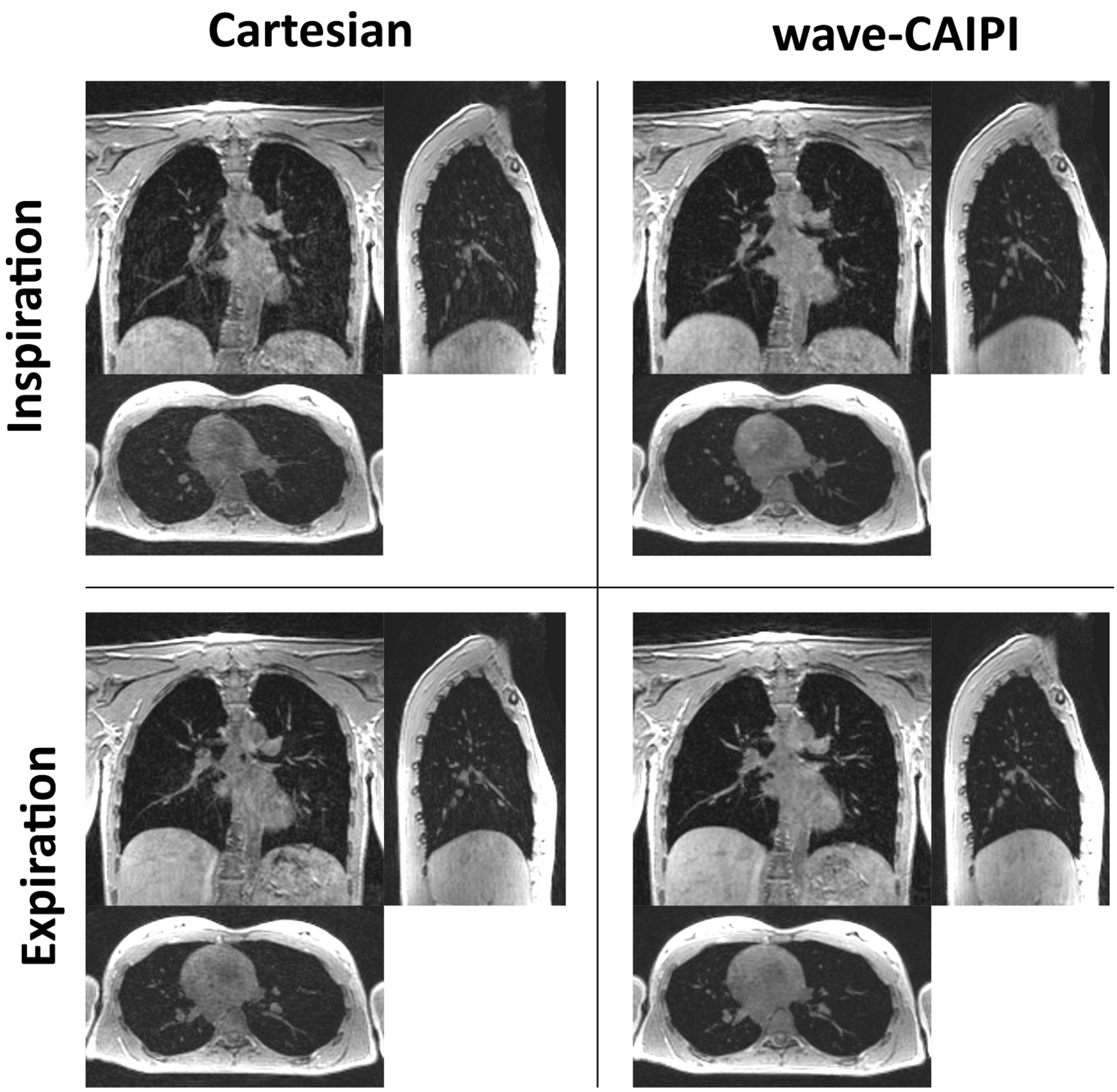
Cartesian
wave-CAIPI
Inspiration
Expiration

Figure 3.4: Comparison of Cartesian and wave-CAIPI 4D lung MRIs in three orientations, for an acquisition time of 02:00 minutes. Residual undersampling artifacts are visible in the Cartesian images. Previously published in [26] under the CC BY-NC 4.0 license.

Scatterplots of the RMSE and NMI, containing data from all 5 volunteers, are displayed in Fig. 3.5. The majority (97%) of the calculated NMI values of the accelerated wave-CAIPI images is higher than the NMI for the Cartesian images. Furthermore, 91% of the individual RMSE values are lower for the wave-CAIPI sampling. The difference between the two sampling techniques is more pronounced for small acquisition times, which corresponds to lower NMI values and higher RMSE values. On average, NMI values were $(10.2 \pm 7.3)\%$ higher, RMSE values were $(18.9 \pm 13.2)\%$ lower for the wave-CAIPI, compared to Cartesian sampling.

Boxplots of the calculated NMI values between retrospectively accelerated images and their respective references for the 5 healthy volunteers are presented in Fig. 3.6. The average was performed over the individual breathing phases. The median NMI values of the wave-CAIPI scans are consistently larger than the NMI values of the Cartesian scans.

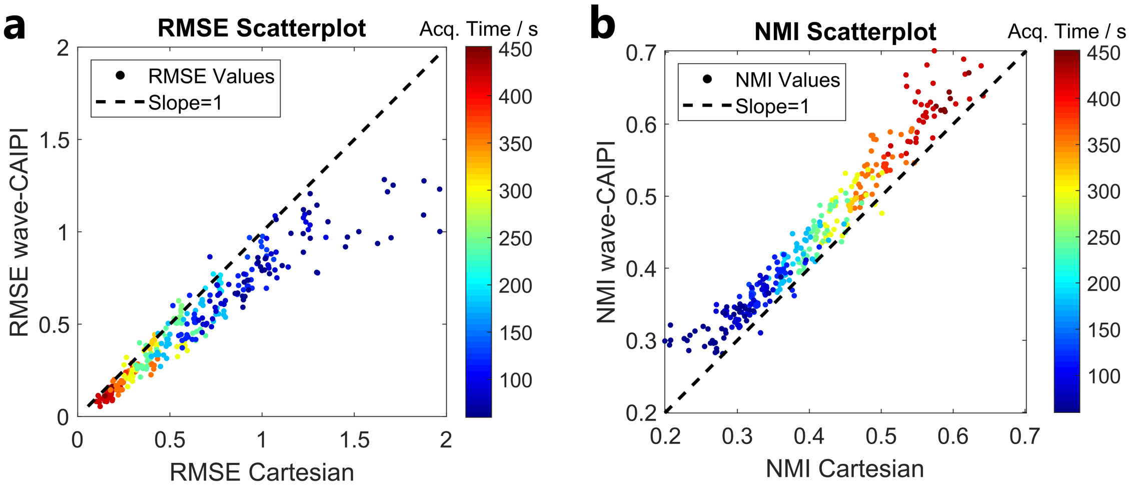

Figure 3.5: Scatterplots of the root-mean-square error (a) and the normalized mutual information (b), comparing wave-CAIPI and Cartesian 4D lung scans for different acquisition times (color encoded). Previously published in [26] under the CC BY-NC 4.0 license.

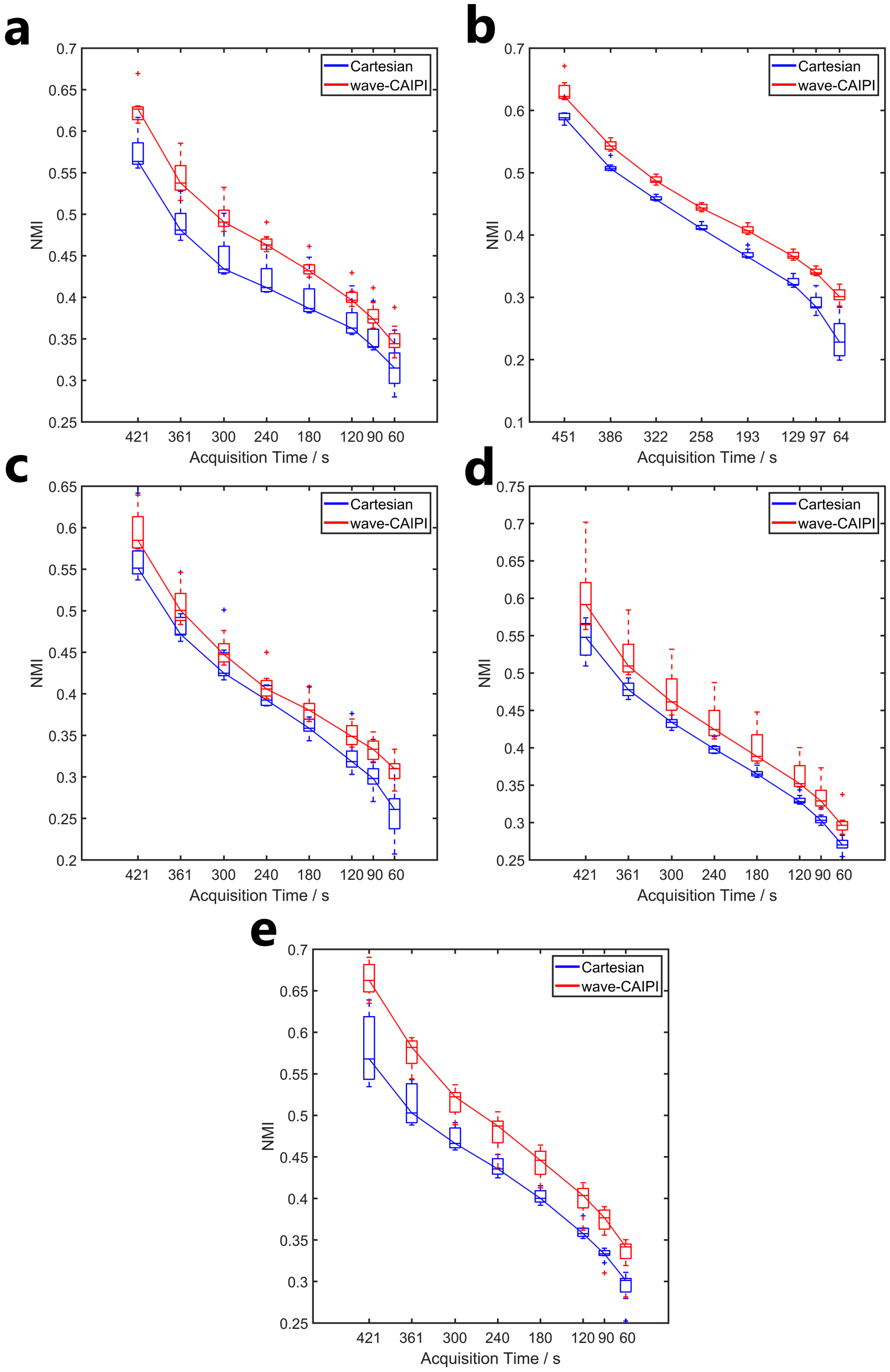

Figure 3.6: Boxplots showing the normalized mutual information between retrospectively accelerated images and their respective references for 5 volunteer examinations (a–e). The average is performed over the individual breathing phases. The median NMI values of the wave-CAIPI technique are consistently higher than the Cartesian NMI values. Previously published in [26] under the CC BY-NC 4.0 license.

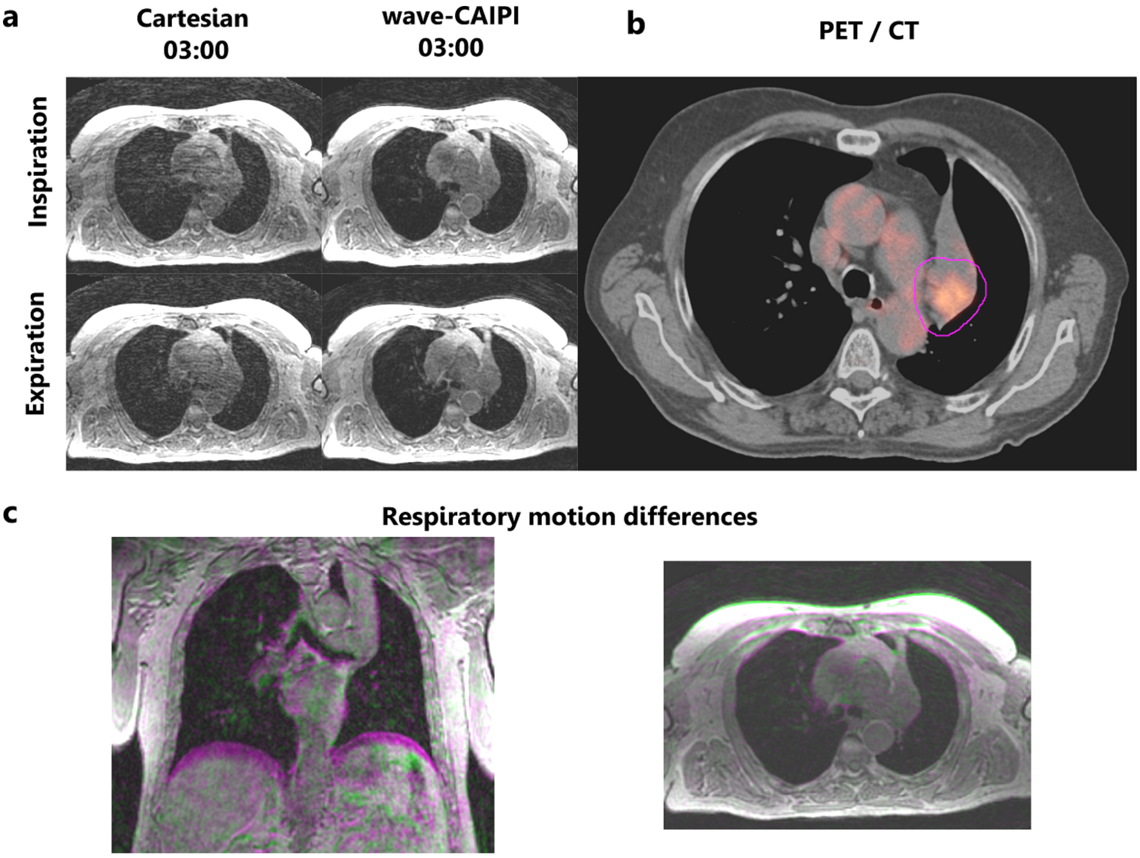

Figure 3.7: (a) Transversal slice of a 4D lung MR scan of a patient with squamous cell carcinoma in the lung in inspiration and expiration, acquired with Cartesian and wave-CAIPI sampling. (b) PET/CT acquisition of a similar slice as in (a), overlaid with the target region for radiotherapy (magenta line). (c) Morphological differences (encoded as magenta/green) between inspiration and expiration in coronal and transversal orientation, determined from a 3-minute 4D lung examination with wave-CAIPI sampling. Previously published in [26] under the CC BY-NC 4.0 license.

Fig. 3.7 presents 4D lung MR scans and a PET/CT (Positron Emission Tomography / Computed Tomography) examination of a patient with squamous cell carcinoma in the lung. The 4D MR images were reconstructed, using a simulated acquisition time of 03:00 minutes. The wave-CAIPI images exhibit superior image quality over the Cartesian images – residual undersampling artifacts remain in the Cartesian case. Fig. 3.7 also shows differences between the end-inspiration and the end-expiration breathing phase from a 3-minute wave-CAIPI scan as a color encoded difference image. Anatomical differences between

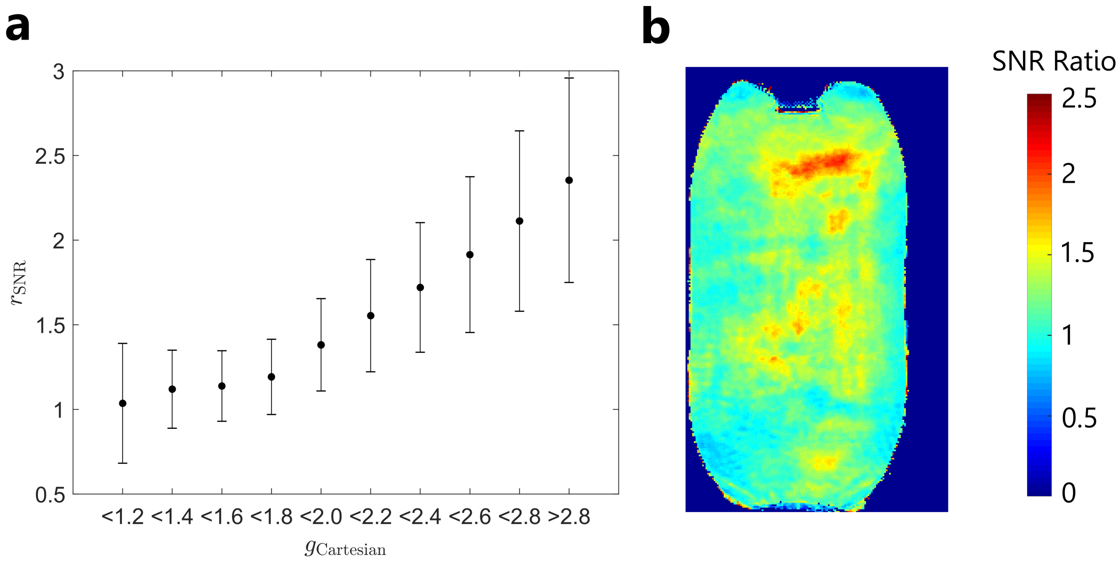

Figure 3.8: (a) SNR ratio $r_{\mathrm{SNR}} = \mathrm{SNR}_{\text{wave-CAIPI}}/\mathrm{SNR}_{\text{Cartesian}}$ in individual pixels of a phantom experiment, binned according to the Cartesian g-factor in the respective pixels. The figure shows a larger SNR benefit of the wave-CAIPI in regions where the Cartesian image exhibits a larger g-factor. (b) Exemplary coronal slice of the SNR ratio map. Previously published in [26] under the CC BY-NC 4.0 license (modified).

inspiration and expiration are most prominent near the diaphragm. From the presented dataset, no relevant respiration-induced tumor displacement can be observed. As a result, the safety margins around the tumor do not need to be increased due to respiration, during the process of radiotherapy treatment planning.

Fig. 3.8a presents the calculated values of the SNR ratio $r_{\mathrm{SNR}} = \mathrm{SNR}_{\text{wave-CAIPI}}/\mathrm{SNR}_{\text{Cartesian}}$ from the phantom study. In each pixel of the phantom, the SNR ratio, as well as the Cartesian and wave-CAIPI g-factors were calculated. The values of the SNR ratio in the individual pixels are binned according to the corresponding Cartesian g-factor in the respective pixel. In regions of the phantom, where the Cartesian g-factor is large, the SNR of the wave-CAIPI technique is more than 2-fold increased. The SNR ratio map was median-filtered, in order to suppress fluctuations. A typical slice of the SNR ratio map is shown in Fig. 3.8b. On average, the SNR gain of the wave-CAIPI

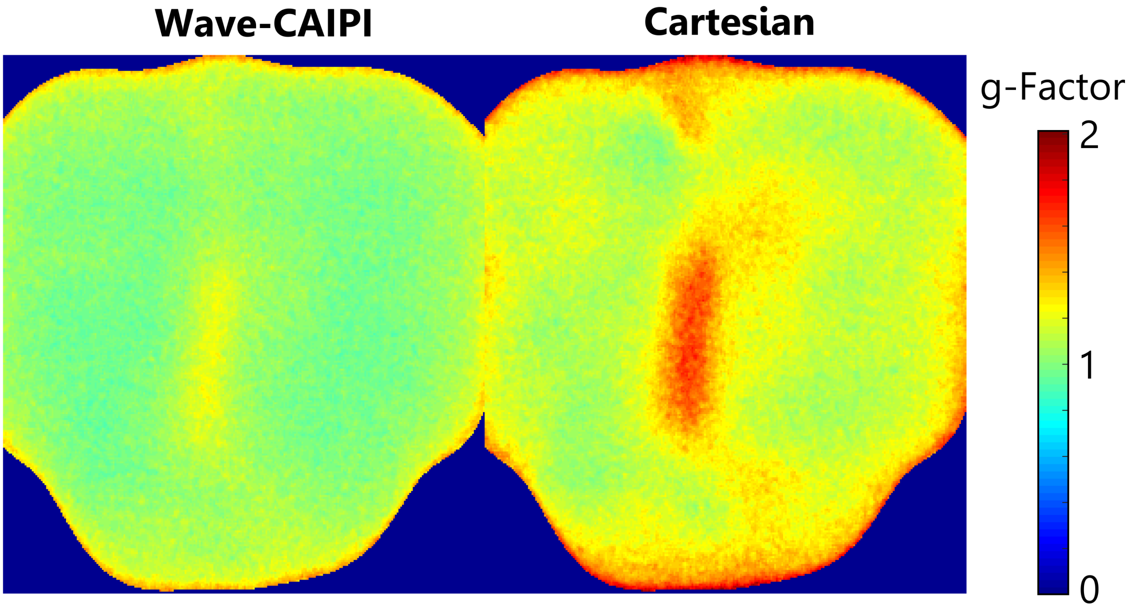

Figure 3.9: g-factor calculations of a simulated 2-minute 4D lung examination for wave-CAIPI (left) and Cartesian sampling (right). For wave-CAIPI sampling, the g-factor is lower. In both cases, the center of the thorax exhibits an elevated g-factor level. Previously published in [26] under the CC BY-NC 4.0 license (modified).

method was $r_{\mathrm{SNR}} = (1.14 \pm 0.31)$, compared to Cartesian imaging. G-factor calculations were performed on the same phantom dataset and resulted in an average g-factor of $g_{\mathrm{mean}} = 1.21$ for wave-CAIPI sampling and $g_{\mathrm{mean}} = 1.34$ for Cartesian sampling.

The simulated in vivo g-factor maps are shown in Fig. 3.9 for a 2-minute 4D lung acquisition of a healthy volunteer. In the center of the thorax, the g-factor is elevated in both the Cartesian and the wave-CAIPI case. For wave-CAIPI sampling, however, the g-factor is smaller, compared to Cartesian sampling.

3.4 Discussion

The NMI as a function of scan time was employed as a quantitative measure of image similarity between the retrospectively accelerated images and their respective references (full-duration initial scan; no retrospective scan time reduction). A series of images with decreasing acquisition time was reconstructed for each breathing phase and the NMI was calculated. As can be observed in Fig. 3.6, the median NMI values of the wave-CAIPI images were always larger than those of the Cartesian images, indicating a lower loss of information due to scan time reduction for the wave-CAIPI technique. Furthermore, the RMSE calculations revealed that the accelerated wave-CAIPI images exhibit smaller discrepancies to their references than the accelerated Cartesian images (c.f. the scatterplot of RMSE in Fig. 3.5).

These findings are consistent with the phantom-based SNR calculations. The average SNR benefit of $r_{\mathrm{SNR}} = (1.14 \pm 0.31)$ of the wave-CAIPI technique leads to a more stable CG SENSE reconstruction, which ultimately reduces residual artifacts from undersampling. Fig. 3.8a shows that the SNR boost by using the wave-CAIPI sampling is larger in regions of the phantom where the Cartesian g-factor is larger. In regions where the Cartesian g-factor is already close to unity, the SNR benefit is small.

To quantify noise enhancement in the Conjugate Gradient SENSE reconstruction, Fig. 3.9 presents the g-factor map of a simulated 2-minute in vivo measurement. The wave-CAIPI sampling technique clearly leads to a reduced g-factor, compared to Cartesian sampling. In both cases, the g-factor is elevated in the center of the thorax.

In the phantom, the average g-factor of the employed setup was $g_{\mathrm{mean}} = 1.21$ for the wave-CAIPI and $g_{\mathrm{mean}} = 1.34$ for the Cartesian sequence. In [14], the g-factors for the wave-CAIPI method were calculated to be $g_{\mathrm{mean}} = 1.03$, compared to $g_{\mathrm{mean}} = 1.42$ for Cartesian 2D-

CAIPI [32,33] sampling for an acceleration rate of $R = 3 \times 3$, suggesting an average SNR benefit of around 40% for the wave-CAIPI. This study, however, employed a regular 3×3 2D-CAIPI undersampling pattern, instead of a random, density-weighted pattern and the measurements were performed with different sequence parameters. Further, a head channel array coil was used, instead of a combination of a body array coil and a spine array coil. Pulse sequence parameters which influence the g-factor in wave-CAIPI examinations are, for instance, the resolution, the readout bandwidth and the maximum gradient wave amplitude, as was systematically investigated in [17, 18].

The wave-encoding technique was already applied to motion corrected, free breathing abdominal imaging [19]. There, the wave-CAIPI proved superior in reducing aliasing and motion artifacts, compared to Cartesian sampling. Furthermore, the SNR was calculated in a phantom study, using fully sampled wave-CAIPI and fully sampled Cartesian acquisitions. The fully sampled wave-CAIPI showed a 45% higher SNR than the fully sampled Cartesian acquisition. However, the readout duration of the wave-CAIPI scan was 3 times higher than the readout duration of the Cartesian scan, which greatly influences SNR calculations.

Further optimization potential of the current setup lies in the selection of wave-CAIPI parameters. The slew rate limits of the employed MR scanner would allow higher gradient wave amplitudes, which in turn could further reduce the g-factor of the wave-CAIPI technique [17, 18]. However, also the level of nerve stimulation needs to be taken into account, as higher gradient amplitudes (and therefore slew rates) result in an increased probability for nerve stimulation. Issues with nerve stimulation or slew rate limits could be overcome by decreasing the number of wave cycles, thereby reducing the slew rate. In the work by Polak et al. [17], it was shown that the g-factor of the wave-CAIPI is nearly independent of the number of complete wave cycles and the number of wave cycles could be decreased to 3.

The results of the patient examination show that the image quality of accelerated acquisitions can be enhanced by employing the wave-CAIPI technique, while keeping scan time constant. No relevant displacement of the tumor could be observed during respiration in the presented case. These findings have important implications on the planning of radiotherapy treatment. Precise knowledge of the tumor displacement during respiration is crucial, since the therapy of the tumor needs to be conducted with the prescribed dose, but adjacent organs at risk (the lung, liver or the heart, for instance) should be spared. In the process of radiotherapy treatment planning, safety margins around the tumor are defined, ensuring adequate dose deposition. If exact displacement of the tumor during respiration is known, the safety margins around the tumor can be adjusted, leading to a dose reduction for organs at risk [48]. Large margins are necessary, if tumor motion is not determined, bearing an increased risk of radiation induced pneumonitis [49]. In the presented case, it was not necessary to increase the safety margins around the tumor due to respiration, leading to a dose reduction of adjacent, healthy tissue. With self-gated 4D lung MRI, regular breathing patterns can be imaged reliably, since in each respiratory phase, sufficient data is available for adequate reconstruction. Extreme breathing states, such as unusually deep inhalation or coughing, however, cannot be covered with this approach. To avoid excessive motion states, patients can be firmly fixed during irradiation, restricting such motion. For the definition of target volumes for irradiation, several planning concepts exist, which are differently influenced by extreme respiratory states [49, 50].

By employing magnetic resonance imaging in the evaluation of tumor displacement instead of computed tomography, the superior soft-tissue contrast of MRI can lead to further reductions, since tumor identification is more reliable. This has been shown in the identification of moving lesions in the pancreas, for instance [51–54]. For adequate tumor delineation and definition of target volumes, the image quality of the MR scans needs to be sufficiently high. Decreasing the acquisition time has a negative impact on the SNR in the image and may lead to unacceptable image quality. By employing the wave-CAIPI sampling technique, the quality of MR images acquired with a short scan time, can be increased, facilitating tumor delineation.

Previous studies showed that simple, linear phase encoding can lead to large voids in k-space after respiratory gating, which complicates parallel imaging reconstructions and can lead to extensive residual undersampling artifacts in the image domain [42, 43]. In this work, the wave-CAIPI technique was implemented to even further reduce large gaps in k-space, since the wave-CAIPI trajectory inherently leads to a more homogeneous sampling density than Cartesian sampling. In terms of quantitative measures of image quality, the combination of wave-CAIPI and a non-uniform sampling density has proven more efficient than non-uniform sampling with the standard Cartesian trajectory. In the case of the wave-CAIPI, missing k-space samples are more evenly distributed, since all three spatial dimensions are involved in undersampling, as discussed in Sec. 2.2. In contrast to that, the frequency encoding direction is always fully sampled in Cartesian acquisitions, leaving only the two phase encoding directions for undersampling. A consequence of that is a reduced artifact level of the wave-CAIPI, as can be observed in the comparison of short 4D lung scans in Fig. 3.3 and Fig. 3.4. There, residual undersampling artifacts remain in the Cartesian images after the iterative SENSE reconstruction, rendering vessel identification and delineation difficult.

A previous study on 4D lung MRI, which used the Cartesian k-space trajectory, achieved full coverage of the lung in 3 minutes [43]. The image comparison for different acquisition times in Fig. 3.3 and the NMI calculations, presented as boxplots in Fig. 3.6 suggest that the image quality of a 3-minute Cartesian scan could also be achieved by a 2-minute wave-CAIPI scan. The benefit of wave-CAIPI could thus be traded for a reduction in acquisition time, without compromising image quality.

Self-gating is a convenient technique to account for respiratory motion, since it does not require external devices or positioning and calibration of navigator readouts. In this work, the DC-navigator signal was obtained by manually selecting a receive coil element near the lung/liver interface. For an automated workflow, an automatic selection of the correct receive element (or a combination thereof) is necessary. Approaches towards optimized, automatic coil selection for respiratory and cardiac self-gating were investigated by Zhang et al. [55].

An interesting extension of the presented work would be the self-gating realtime tracking of the respiratory phase and to select the phase encoding steps accordingly. Thereby, arbitrary and fixed sampling patterns could be achieved in all breathing states. However, such an approach would come at the price of an unpredictable scan time, which complicates accurate patient planning in clinical routine. Furthermore, adjacent breathing phases of the dynamic dataset differ only slightly. These temporal correlations could be exploited in compressed sensing approaches, in order to further reduce the acquisition time [3–5].

3.5 Conclusion

Quantitative image analysis, involving image similarity measures and SNR calculations, demonstrated an enhanced image quality for the accelerated wave-CAIPI technique, compared to the Cartesian sequence in free-breathing self-gated 4D lung MRI. The benefit of the wave-CAIPI technique can be traded for either enhanced image quality or a reduced acquisition time. In combination with a randomized, density weighted phase encoding scheme, the wave-CAIPI method enables full coverage of the human lung in 8 breathing states within only 2 minutes.

4 | Wave-CAIPI for 4D Flow MRI of the Aorta

This chapter reports on accelerated 4D flow examinations of 11 volunteers (10 healthy volunteers and 1 patient), comparing the wave-CAIPI k-space trajectory to standard Cartesian sampling. Flow velocity is quantified in the aorta and hemodynamic flow patterns are visualized. Discrepancies in several flow parameters, arising from undersampling, are investigated and statistical significance is evaluated.

The majority of the presented findings has been accepted and will be published as a full paper in *Magnetic Resonance in Medicine* by John Wiley & Sons, Inc. with DOI 10.1002/mrm.28605, under the Creative Commons BY-NC 4.0 License[1] [56]. Figures that were replicated in this work (entirely, or in parts) are declared accordingly.

4.1 Background

Magnetic resonance imaging can not only be used to represent static tissue via magnitude images – also flow can be encoded into the MR signal. By applying special velocity encoding gradients, the flow velocity can be encoded into the phase of the MR signal (phase contrast MRI). This information can be exploited for flow quantification in various organs. Conventional phase contrast imaging resolves only the flow velocity perpendicular to a 2D imaging plane. Especially for cardiac applications, it is interesting to examine the 3-directional velocity vector field in a 3D volume, resolved over the cardiac cycle (4D flow MRI). Cardiac 4D flow examinations allow the calculation of several flow parameters, such as the peak flow velocity or the flow rate [7, 57–60]. One advantage of 4D flow MRI over conventional 2D phase contrast methods is its ability to visualize complex hemodynamic patterns and to quantify flow in arbitrary plane orientations and positions after the examination. The dynamic 3D visualization of blood flow can be useful in the identification of heart diseases, since various heart diseases can be associated with blood flow alterations. For instance, patients with aortic valve stenosis exhibit an increased local peak flow velocity along the outer wall of the ascending aorta [60]. 4D flow MRI is also employed for flow quantification in neuro and abdominal applications [8, 61–64].

---

[1] https://creativecommons.org/licenses/by-nc/4.0/

A considerable obstacle for 4D flow examinations to be integrated in daily clinical routine, however, is the extensive scan time that is required. 4D flow examinations require spatial encoding in three dimensions, flow-encoding in three dimensions and resolution of the cardiac cycle. Such an examination is therefore associated with a challenging 7-dimensional encoding problem. Furthermore, sub-optimal respiratory navigators additionally increase scan time. As time slots for clinical MR applications are limited and patient comfort is reduced in lengthy MR scans, parallel imaging techniques can be employed to accelerate the examinations. As was outlined in Sec. 2.1.3, parallel imaging comes at the cost of an increased noise level in the final images, the magnitude of which depends on the acceleration rate, the coil geometry and details about the k-space sampling. It was shown in Chapter 3 that by employing the wave-CAIPI k-space trajectory, instead of Cartesian sampling, the noise enhancement in parallel imaging can be reduced, since the g-factor for wave-CAIPI is smaller than for Cartesian sampling [14]. The wave-CAIPI technique has proven very effective in the reconstruction of highly undersampled 3D MR images for various applications [14–19, 26]. It is therefore a promising technique to accelerate 4D flow acquisitions.

An interesting approach to 4D flow imaging with non-Cartesian k-space trajectories is presented in [65], where a stack-of-spirals trajectory was shown to yield higher SNR than Cartesian 4D flow examinations. However, efficient spiral k-space trajectories usually have a long readout duration, which can cause considerable blurring in the images, related to off-resonance [20, 21] and may require compensation techniques. A generic problem in non-Cartesian MR imaging are gradient system imperfections that can also lead to significant image artifacts. In this case, the general model of the gradient system transfer function [10, 22–24] can be applied to correct for imperfections in the gradient system.

Aside from parallel imaging techniques and optimal k-space sampling, the acquisition time of 4D flow examinations can also be reduced by optimizing the respiratory navigator, which is required to obtain images free of blurring or motion artifacts. Respiratory motion can be taken into account by applying a navigator window at the lung/liver interface and only accepting data measured at a specific respiratory phase. However, such an approach can lead to very low acceptance rates and generally results in unpredictable scan times. Studies on improved navigator acceptance rates were performed, for instance in [7, 66].

In this work, the potential of the wave-CAIPI technique to accelerate 4D flow acquisitions is assessed by means of in vivo examinations of healthy volunteers and one patient with aortic valve stenosis. The results of 4D flow examinations with Cartesian 2D-CAIPI sampling [32, 33] and wave-CAIPI sampling are compared, regarding bias and precision of flow parameters and noise estimates.

4.2 Methods

Setup

4D flow acquisitions were performed, using a spoiled gradient echo pulse sequence with 3-directional flow velocity encoding. The flow velocity $\vec{v}$ is encoded in the phase of the MR signal via a bipolar gradient pair – two gradients of equal moment and opposite orientation, prior to data acquisition. A representation of flow velocity encoding is given in Fig. 4.1. The phase evolution of stationary spins is shown in Fig. 4.1b. In Fig. 4.1c, a spin ensemble is assumed to move from position $x = x_1$ to $x = x_2$. Only the moving spin ensemble acquires a net phase due to the flow encoding gradient. Flow velocity can only be encoded in one direction at a time and requires the measurement of a reference phase, in order to calculate the phase contribution of the flow encoding gradient. Therefore, a total of 4 3D images is required to calculate the 3-dimensional flow velocity vector $\vec{v} = (v_x, v_y, v_z)$.

A pulse sequence diagram with flow encoding is displayed in Fig. 4.2. For time efficiency, the bipolar flow velocity encoding gradients are combined with the readout dephaser gradient and the two phase encoding gradients, respectively. 4D flow examinations were performed with the Cartesian k-space trajectory and the wave-CAIPI method, using sinusoidal gradient wave amplitudes as presented in Fig. 4.2. In this study, the wave-CAIPI parameters were chosen to be: number of complete wave cycles $N_{\text{wave}} = 4$ and maximum gradient wave amplitude $A_{\text{wave}} = 9\,\text{mT/m}$. Further relevant sequence parameters were: FOV $= 320 \times (260{-}320) \times (98{-}180)\,\text{mm}^3$, flip angle $\varphi = 7°$, $T_R = 6.03\,\text{ms}$, $T_E = 3.40\,\text{ms}$, readout bandwidth BW $= 500\,\text{Hz/px}$, maximum encoded flow velocity $v_{\text{ENC}} = (200{-}250)\,\text{cm/s}$. The images were acquired in sagittal orientation with a spatial resolution of $2.5 \times 3.5 \times (3.5{-}5.0)\,\text{mm}^3$ and a k-space matrix of size

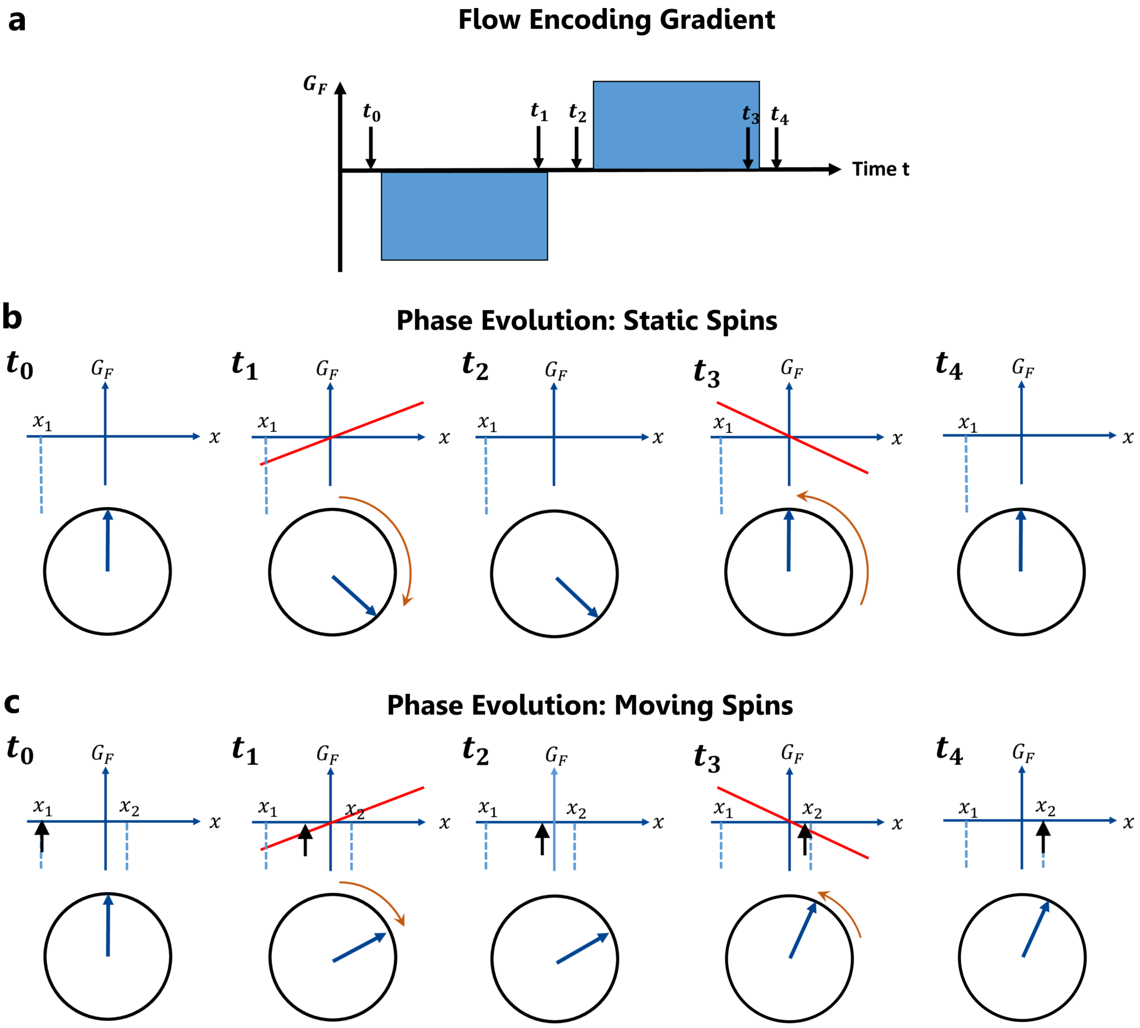
a
Flow Encoding Gradient
G_F
t_0
t_1
t_2
t_3
t_4
Time t
b
Phase Evolution: Static Spins
t_0
t_1
t_2
t_3
t_4
G_F
x_1
x
c
Phase Evolution: Moving Spins
t_0
t_1
t_2
t_3
t_4
G_F
x_1
x_2
x

Figure 4.1: Representation of flow velocity encoding into the phase of the MR signal via a bipolar gradient (a). (b) and (c) show the phase evolution of stationary and moving spins, respectively. Only moving spins acquire a net phase due to the bipolar gradient.

128 × (76−96) × (28−36). Frequency encoding direction was chosen to be in head-feet direction. A slab-selective RF pulse in left-right direction was used for excitation. The imperfect excitation profile of the RF pulse lead to considerable aliasing in the outer slices. For the purpose of time efficiency, no slice oversampling was performed in order to eliminate the aliasing, instead, the aliasing was inherently removed during the iterative SENSE reconstruction. The acquisition was triggered using an external ECG (electrocardiogram) device. Between 11 and 14 cardiac phases were resolved with ECG-gating, leading to an acquisition window of 550−700 ms in each heart beat at a temporal resolution of 48.42 ms.

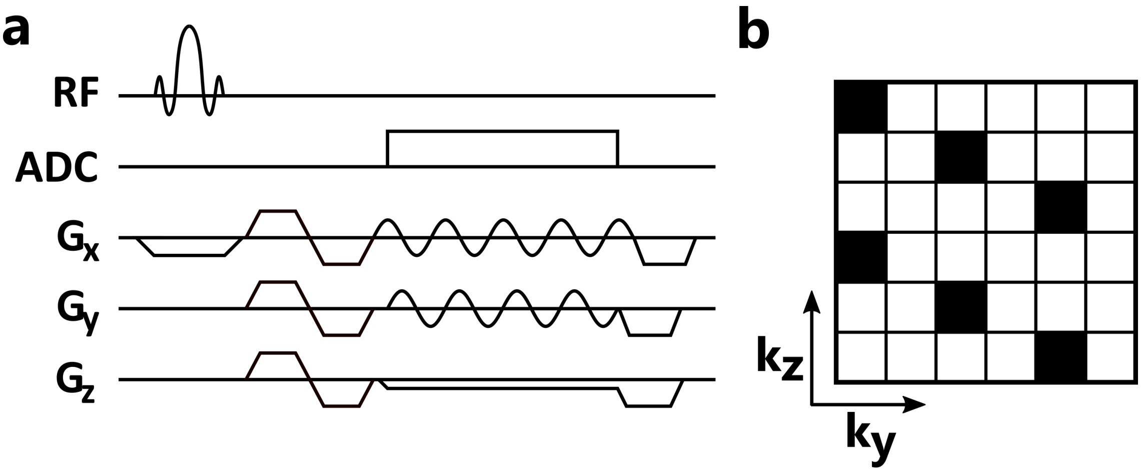

Figure 4.2: (a) Pulse sequence diagram of a spoiled 3D gradient echo with 3-directional flow velocity encoding. The bipolar velocity encoding gradients are combined with the readout dephaser gradient and the two phase encoding gradients. (b) 2D-CAIPI undersampling pattern for an acceleration rate of $R = 2 \times 3 = 6$. Previously published in [56] under the CC BY-NC 4.0 license.

The examination was further respiratory gated by employing a navigator readout, positioned at the lung/liver interface (c.f. Fig. 4.3). Data was acquired in expiration phase. The ReCAR (Respiratory Controlled Adaptive k-space Reordering) technique was employed, in order to increase the acceptance rate of the respiratory navigator [7]. Thereby, the phase encoding order is adjusted in realtime, acquiring data near the k-space center at end-expiration and in the k-space periphery during inspiration. The reordering of the phase encoding scheme according to the respiratory phase allows for a larger navigator acceptance window of 8 mm, without introducing blurring or motion artifacts in the images. Due to respiratory and cardiac gating, the total acquisition time depended on the subject's specific breathing pattern and heart rate. On average, one 4D flow examination required (11:55 ± 02:01) min, with a prospective acceleration rate of $R = 2$ in the anterior-posterior direction.

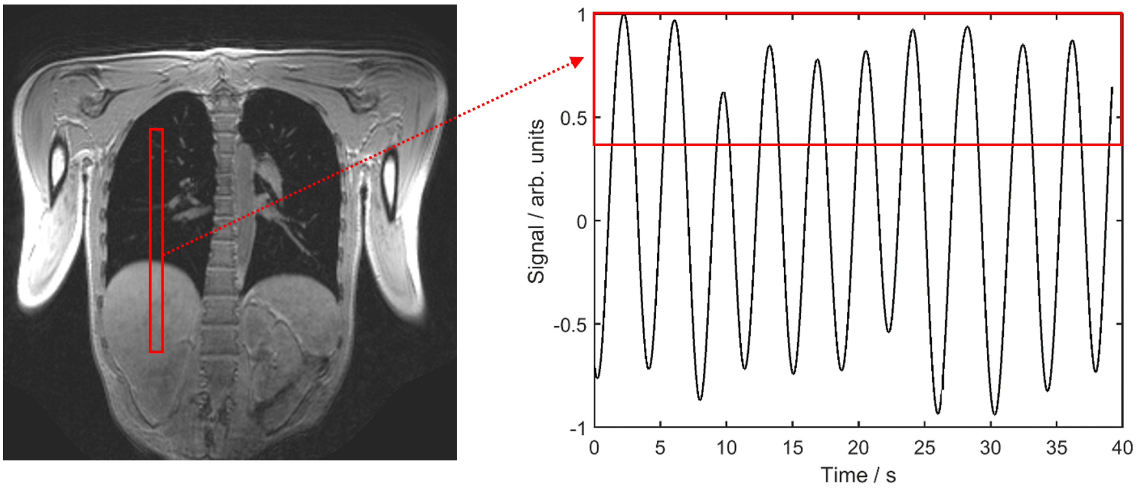

Figure 4.3: Prospective respiratory gating, using a navigator readout positioned at the lung/liver interface. The navigator readout measures the diaphragm position and data is only accepted near expiration.

In this study, 4D flow examinations, performed with Cartesian/2D-CAIPI [32,33] sampling and wave-CAIPI sampling, are compared. To this end, flow parameters were evaluated in 10 healthy volunteers (age: (25.3 ± 2.7) years, 3 male) and one patient (84 years, female) with known aortic valve stenosis. The healthy volunteers were examined with both sampling schemes, the patient was examined only with the wave-CAIPI technique. The acquisition time for the patient measurement was 17:15 min, performed also with a prospective acceleration rate of $R = 2$ in the anterior-posterior direction.

All experiments were performed using a clinical 3 Tesla MR scanner (MAGNETOM Prisma$^{\text{fit}}$, Siemens Healthcare, Erlangen, Germany).

Reconstruction

Image reconstruction of undersampled datasets was performed in analogy to Sec. 3.2, i.e., an iterative Conjugate Gradient SENSE algorithm was employed. Sensitivity maps were calculated with ESPIRiT [46], as implemented in the Berkeley Advanced Reconstruction Toolbox [47], using an additional low-resolution Cartesian scan with increased FOV in the coronal plane. Gradient system imperfections were taken into account in retrospective, i.e., during the reconstruction using the gradient system transfer function that was presented in Sec. 2.3.

Flow and Image Analysis

The noise levels in the 6-fold accelerated 2D-CAIPI and wave-CAIPI images were calculated using the pseudo multiple replica approach [31]. To this end, noise correlations were measured in a short pre-scan. For both sampling strategies, 500 reconstructions were performed with additional noise added to the data and image noise was determined as the standard deviation in each pixel across the different replicas.

In order to assess the precision of flow parameters for accelerated Cartesian and wave-CAIPI 4D flow acquisitions, the datasets were retrospectively undersampled (acceleration rates between $R = 2$ and $R = 8$). The maximum possible undersampling rate was determined to be $R = 6$, using the possibility of clear delineation and segmentation of the aorta as a criterion. Finally, the 4D flow sets were retrospectively undersampled in partition encoding direction by an acceleration rate of 3 (total undersampling factor $R = 2 \times 3 = 6$). This corresponds to a simulated scan time reduction from (11:55 ± 02:01) min to (03:58 ± 00:40) min. For the 10 healthy volunteers, the flow rate Q, the net flow per cycle Q_{net}, the peak velocity v_{max} and the net average through-plane velocity $\bar{v}^{\perp}$ were calculated in 8 planes along the ascending and descending aorta. The values of the flow parameters from the retrospectively accelerated scans ($R = 6$) were then compared to those of the reference scan ($R = 2$). The estimated error in flow parameters due to undersampling was calculated and compared for the wave-CAIPI and 2D-CAIPI sampling scheme. Errors are reported as the mean signed difference (denoted by angular brackets $\langle\cdot\rangle$) and the mean absolute difference (L_1-norm) in flow parameters between the 6-fold accelerated scan and the corresponding reference scan ($R = 2$). The error measures are used to assess bias and precision, respectively. For the flow rate Q, e.g., the errors are calculated as follows:

$$\begin{aligned}
L_1(\Delta Q) &= \frac{1}{N_{\mathrm{phases}} N_{\mathrm{planes}}} \sum_{i}^{N_{\mathrm{planes}}} \sum_{j}^{N_{\mathrm{phases}}} \left|\Delta Q_{i,j}\right| \\
&= \frac{1}{N_{\mathrm{phases}} N_{\mathrm{planes}}} \sum_{i}^{N_{\mathrm{planes}}} \sum_{j}^{N_{\mathrm{phases}}} \left|Q_{i,j}^{\mathrm{R=6}} - Q_{i,j}^{\mathrm{R=2}}\right| \qquad (4.1) \\
\langle \Delta Q \rangle &= \frac{1}{N_{\mathrm{phases}} N_{\mathrm{planes}}} \sum_{i}^{N_{\mathrm{planes}}} \sum_{j}^{N_{\mathrm{phases}}} \left(Q_{i,j}^{\mathrm{R=6}} - Q_{i,j}^{\mathrm{R=2}}\right),
\end{aligned}$$

where N_{planes} denotes the number of analysis planes and N_{phases} is the number of cardiac phases. Differences between the 2-fold and the 6-fold accelerated scans (i.e., ΔQ, ΔQ_{net}, Δv_{max} and $\Delta\bar{v}^{\perp}$) were tested for statistical significance, using the paired Wilcoxon signed rank test at the 5% significance level.

Possible discrepancies between flow parameters obtained from Cartesian and wave-CAIPI examinations were investigated by linear regressions of the parameter values for an acceleration rate of $R = 2$. Furthermore, a paired Wilcoxon signed rank test was employed to assess the statistical significance of the discrepancies between wave-CAIPI and Cartesian sampling at the 5% significance level.

Hemodynamic patterns were visualized by means of streamlines, particle traces and velocity vectors. In addition to the quantitative comparison of calculated uncertainties in flow parameters to investigate differences between Cartesian/2D-CAIPI and wave-CAIPI scans, a qualitative comparison of flow visualization was performed. For all volunteers, the same aorta segmentation was used for the wave-CAIPI and Cartesian/2D-CAIPI images, to ensure adequate comparability.

The 4D flow datasets were evaluated and visualized with a prototype software (4D Flow V2.4, Siemens Healthcare, Erlangen, Germany). Image processing involved background phase correction, correction of velocity-aliasing and vessel segmentation.

4.3 Results

Magnitude wave-CAIPI images are shown in Fig. 4.4a for a healthy volunteer during early systole, comparing different acceleration rates. In Fig. 4.4b, pixel-based velocity errors are displayed for a wave-CAIPI and a 2D-CAIPI 4D flow acquisition with a retrospective undersampling factor of $R = 6$. The 2-fold accelerated acquisition was used as a reference. Velocity encoding was performed in left-right, anterior-posterior and head-feet direction, respectively.

Magnitude and 3-directional flow encoded phase contrast images of a healthy volunteer are displayed in Fig. 4.5, where wave-CAIPI images are compared to Cartesian/2D-CAIPI images. Images are shown for a retrospective acceleration of $R = 6$ and the initially acquired, 2-fold accelerated reference scans.

The calculation of the noise level in the 6-fold accelerated wave-CAIPI and 2D-CAIPI 4D flow MRIs of a healthy volunteer are displayed in Fig. 4.6. In the region of the highest noise amplitude, the noise level of the 2D-CAIPI scan was 3.35 times higher than the noise

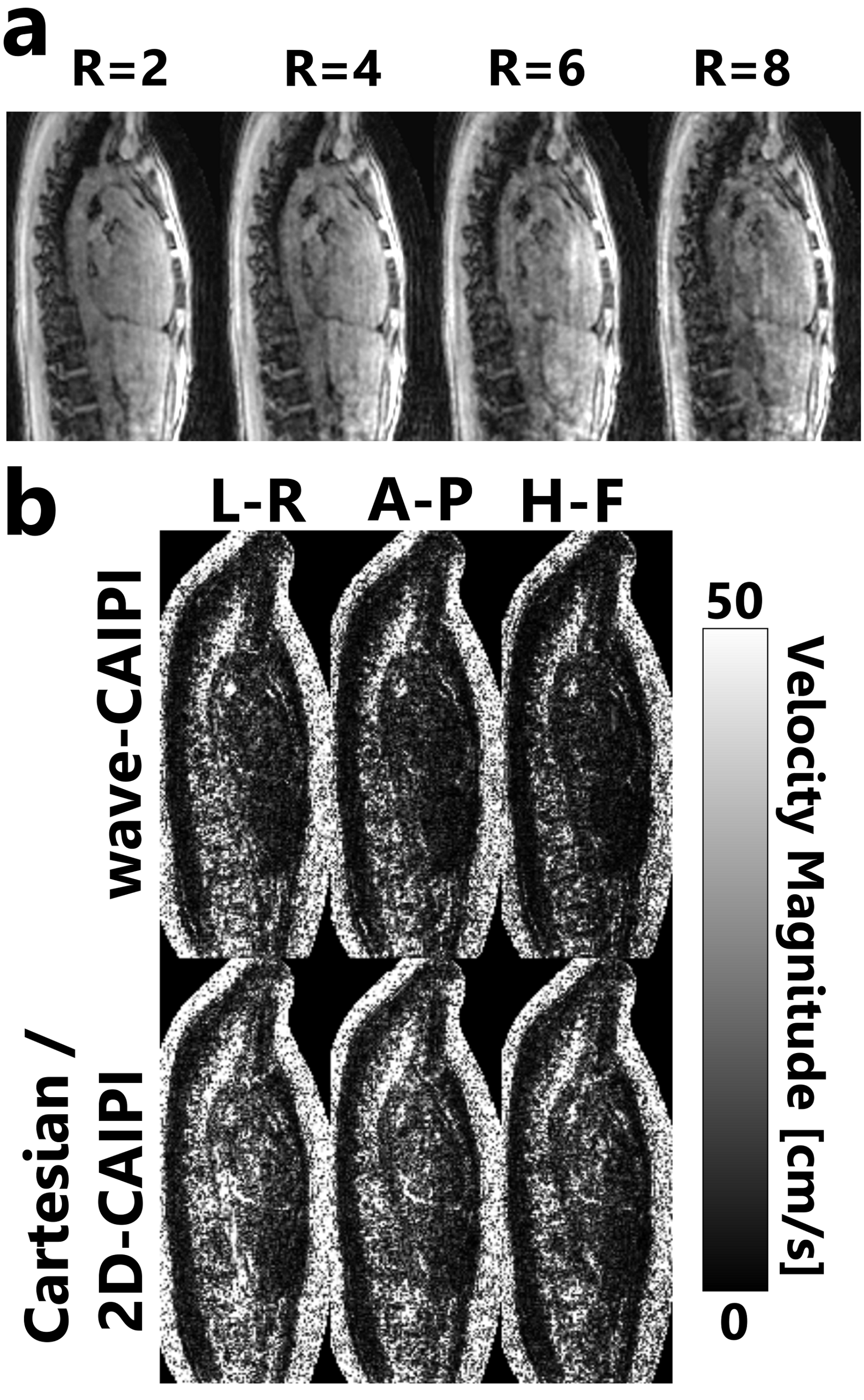
a
R=2
R=4
R=6
R=8
b
L-R
A-P
H-F
wave-CAIPI
Cartesian /
2D-CAIPI
50
Velocity Magnitude [cm/s]
0

Figure 4.4: (a) Magnitude wave-CAIPI images of a healthy volunteer during early systole for different acceleration rates. (b) Pixel-based velocity differences between $R = 2$ and $R = 6$ in left-right, anterior-posterior and head-feet direction for wave-CAIPI and 2D-CAIPI 4D flow acquisitions. An image mask has been applied in both (a) and (b). Previously published in [56] under the CC BY-NC 4.0 license (modified).

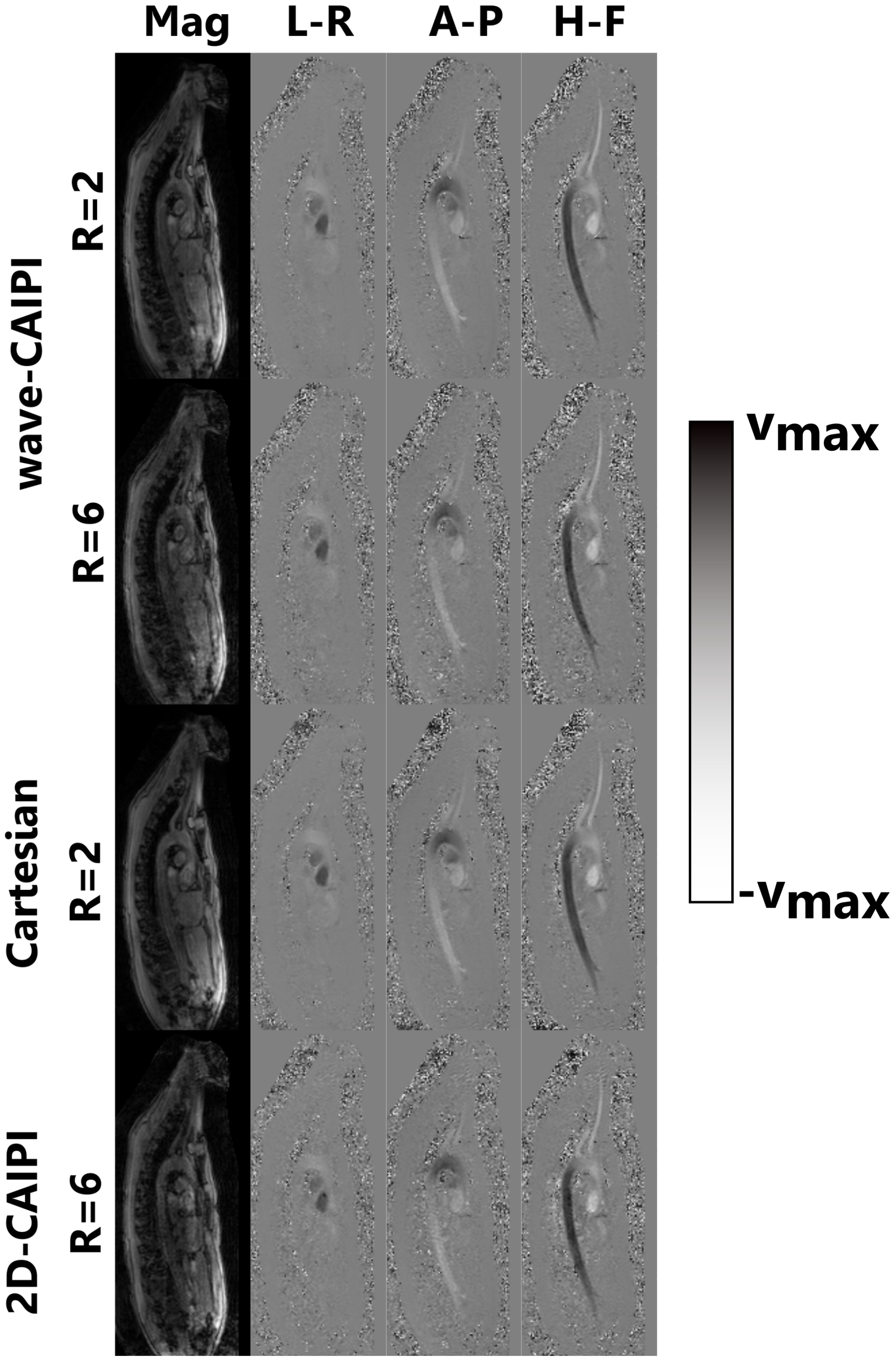
Mag
L-R
A-P
H-F
wave-CAIPI
R=2
R=6
Cartesian
R=2
2D-CAIPI
R=6
vmax
-vmax

Figure 4.5: Results of 4D flow examinations of a healthy volunteer, using wave-CAIPI and Cartesian/2D-CAIPI sampling. The first column represents magnitude images for the different sampling schemes and for accelerations of $R = 2$ and $R = 6$. The subsequent columns show phase contrast images, encoding flow velocity in left-right, anterior-posterior and head-feet direction, respectively. Previously published in [56] under the CC BY-NC 4.0 license (modified).

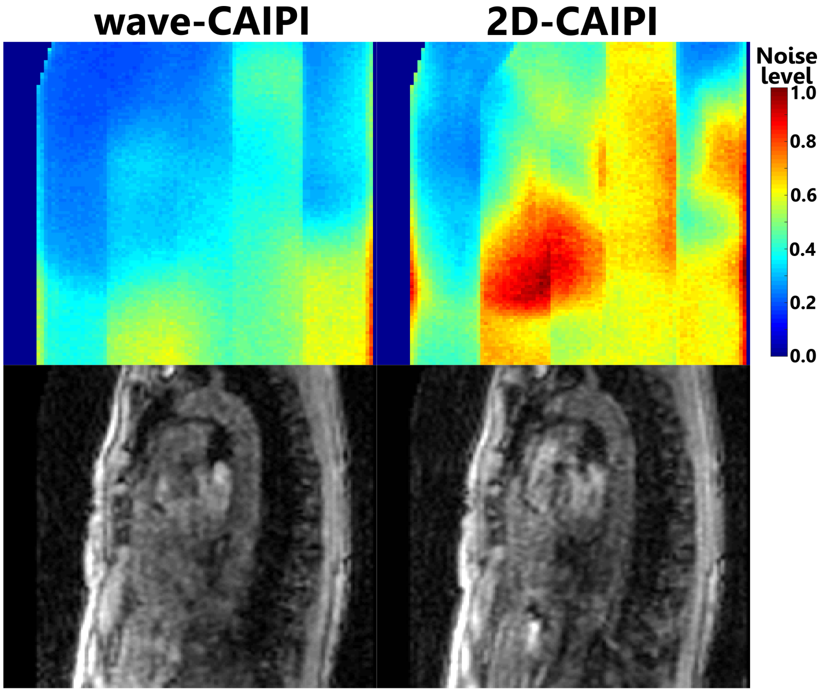
wave-CAIPI
2D-CAIPI
Noise level
1.0
0.8
0.6
0.4
0.2
0.0

Figure 4.6: Noise level calculated in wave-CAIPI (left) and 2D-CAIPI (right) 4D flow MRIs with an acceleration factor of $R = 6$. The upper row displays the noise maps, the lower row the corresponding magnitude images during diastole. Previously published in [56] under the CC BY-NC 4.0 license.

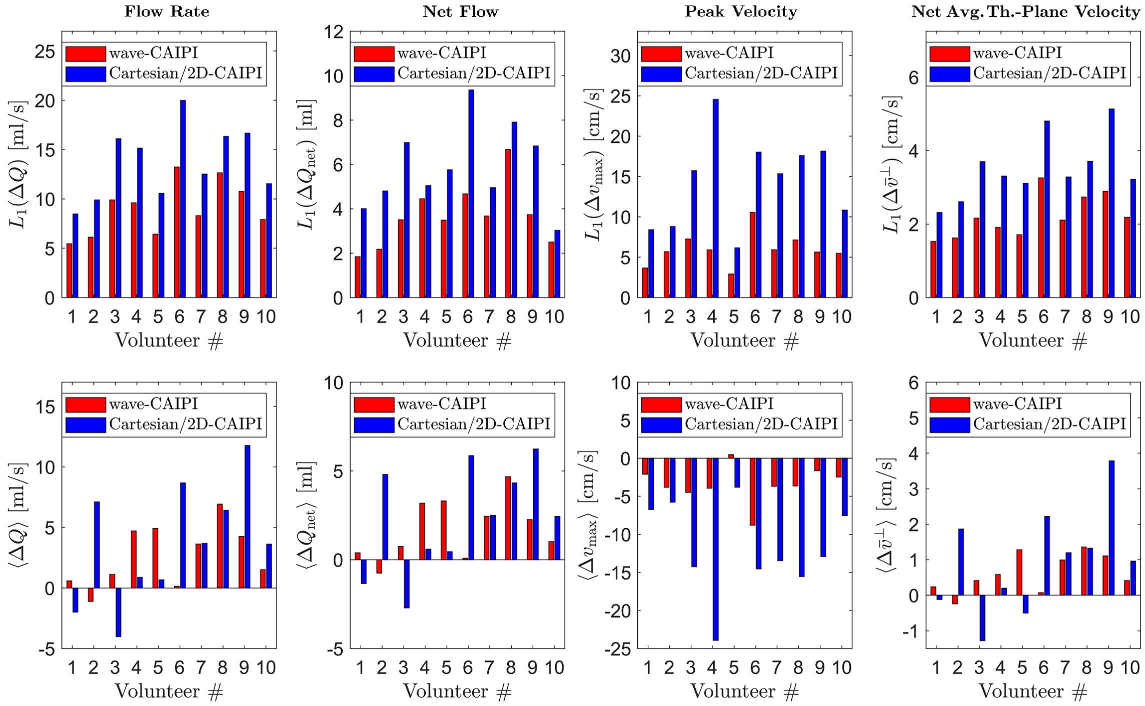

Figure 4.7: Mean absolute differences in the flow parameters Q, Q_{net}, $v_{\max}$ and $\bar{v}^{\perp}$ of 6-fold accelerated 4D flow examinations, compared to the reference (2-fold accelerated 4D flow scan) for wave-CAIPI and Cartesian/2D-CAIPI sampling. The results are presented for each of the 10 healthy volunteers individually. Previously published in [56] under the CC BY-NC 4.0 license.

level of the wave-CAIPI scan. On average, the noise level of the 2D-CAIPI scan was $(43 \pm 38)\%$ higher than that of the wave-CAIPI examination.

In Fig. 4.7, the estimated errors in the flow parameters Q, Q_{net}, $v_{\max}$ and $\bar{v}^{\perp}$ of the 6-fold accelerated wave-CAIPI and 2D-CAIPI scans are presented for the examinations of the healthy volunteers. Errors are reported as the mean absolute difference (L_1-norm) and the mean signed difference ($\langle\cdot\rangle$) in flow parameters between the 6-fold accelerated scan and the corresponding reference scan ($R = 2$), according to Eqs. 4.1. In every case, the mean absolute difference of wave-CAIPI flow parameters is lower than the mean absolute difference of the 2D-CAIPI flow parameters. For the flow rate, the mean absolute difference was $(34.5 \pm 4.8)\%$ lower, for the net flow, the difference

	$\langle\Delta Q\rangle$ [ml/s]	$\langle\Delta Q_{\mathrm{net}}\rangle$ [ml]	$\langle\Delta v_{\max}\rangle$ [cm/s]	$\langle\Delta\bar{v}^{\perp}\rangle$ [cm/s]
Wave-CAIPI	2.63 ± 12.73	1.74 ± 4.47	-3.45 ± 8.45	0.61 ± 3.09
Cartesian/2D-CAIPI	3.51 ± 19.13	2.32 ± 7.11	-11.82 ± 18.16	0.90 ± 5.13
	$L_1(\Delta Q)$ [ml/s]	$L_1(\Delta Q_{\mathrm{net}})$ [ml]	$L_1(\Delta v_{\max})$ [cm/s]	$L_1(\Delta\bar{v}^{\perp})$ [cm/s]
Wave-CAIPI	9.03 ± 2.67	3.67 ± 1.40	6.02 ± 2.08	2.21 ± 0.58
Cartesian/2D-CAIPI	13.73 ± 3.66	5.87 ± 1.91	14.36 ± 5.68	3.52 ± 0.88

Table 4.1: Discrepancies in flow rate Q, net flow Q_{net}, peak velocity $v_{\max}$ and net average through-plane velocity $\bar{v}^{\perp}$ between 2-fold and 6-fold accelerated scans (for both wave-CAIPI and Cartesian/2D-CAIPI sampling). The results are averaged over all volunteer examinations and are reported as mean difference ($\langle\cdot\rangle$) and mean absolute difference ($L_1(\cdot)$) to report on bias and precision, respectively.

was (36.4 ± 17.0)% lower, for the peak velocity, the difference was (55.4 ± 12.1)% lower and for the net average through-plane velocity, the difference was (37.0 ± 6.0)% lower. In most of the cases, the mean signed differences in flow parameters are lower for wave-CAIPI sampling, with respect to 2D-CAIPI sampling. The mean absolute difference and the mean signed difference, averaged over all healthy volunteer examinations, are displayed in Tab. 4.1.

A comparison of the calculated flow rates for Cartesian and wave-CAIPI sampling is shown in Fig. 4.8 for the examinations of the 10 healthy volunteers, in the case of 2-fold undersampling. The linear regression of the individual flow rate values indicates good accordance between both sampling techniques (slope of regression line: 0.987). The differences of the flow rate in the Bland-Altman plot of Fig. 4.8b are symmetrically distributed around the mean value. The (signed) mean difference, averaged over all volunteers, is $\Delta Q = (0.7 \pm 13.7)\,\mathrm{ml/s}$. For the net flow per cycle, the mean difference is $\Delta Q_{\mathrm{net}} = (0.46 \pm 3.84)\,\mathrm{ml}$. For the peak velocity, the mean difference is $\Delta v_{\max} = (1.9 \pm 7.1)\,\mathrm{cm/s}$ and for the net average through plane velocity $\Delta\bar{v}^{\perp} = (0.2 \pm 3.4)\,\mathrm{cm/s}$. The correlation plots and Bland-Altman

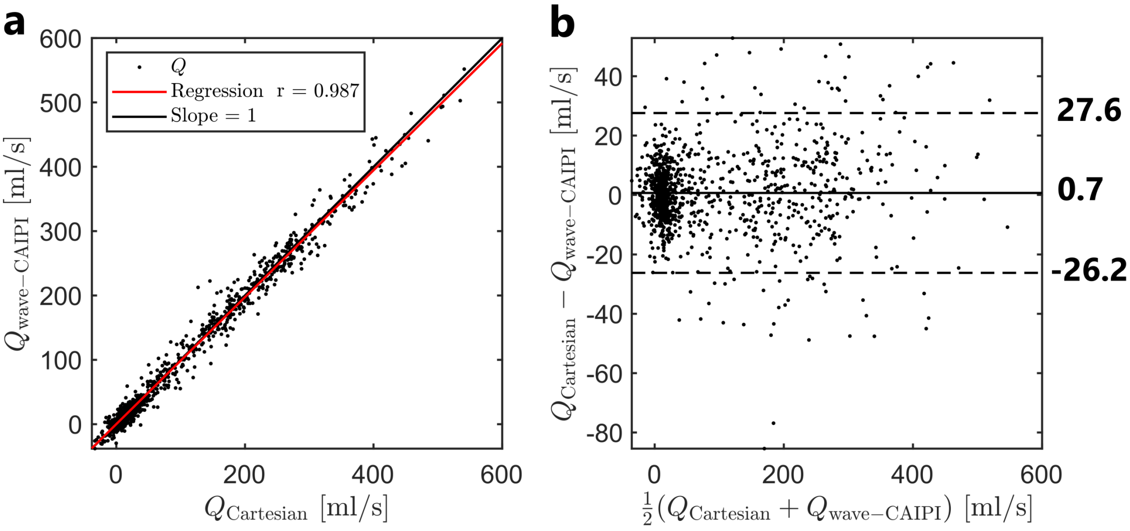

Figure 4.8: (a) Correlation plot and linear regression, comparing the individual flow rate values of 2-fold accelerated wave-CAIPI and Cartesian 4D flow scans for 10 healthy volunteers. (b) Bland-Altman plot, comparing the flow rate of 2-fold accelerated wave-CAIPI and Cartesian 4D flow scans. Previously published in [56] under the CC BY-NC 4.0 license (modified).

plots of Q_{net}, $v_{\max}$ and $\bar{v}^{\perp}$ are presented in Figs. 4.9, 4.10 and 4.11, respectively. A paired Wilcoxon signed rank test was performed to investigate whether the differences are statistically significant. The Null-Hypothesis that the individual differences in flow parameters originate from a distribution with zero mean was rejected in 3/10 volunteers for Q, in 1/10 volunteers for Q_{net}, in 8/10 volunteers for $v_{\max}$ and in 3/10 volunteers for $\bar{v}^{\perp}$ at the 5% significance level. Table 4.2 summarizes the mean differences in flow parameters and reports on the statistical significance for all 10 volunteers.

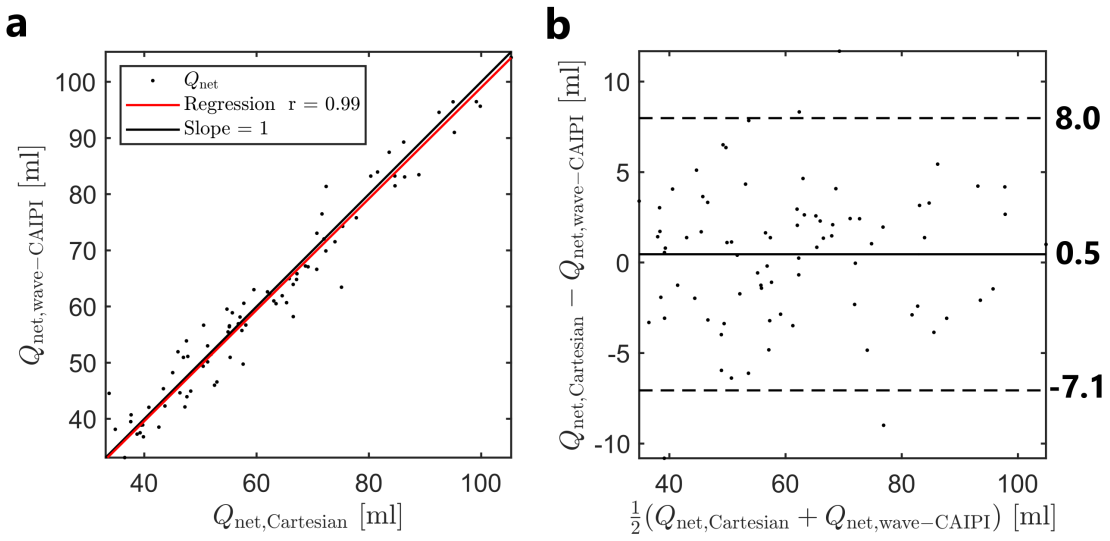

Figure 4.9: (a) Correlation plot and linear regression, comparing the individual net flow values of 2-fold accelerated wave-CAIPI and Cartesian 4D flow scans for 10 healthy volunteers. (b) Bland-Altman plot, comparing the net flow of 2-fold accelerated wave-CAIPI and Cartesian 4D flow scans. Previously published in [56] under the CC BY-NC 4.0 license (modified).

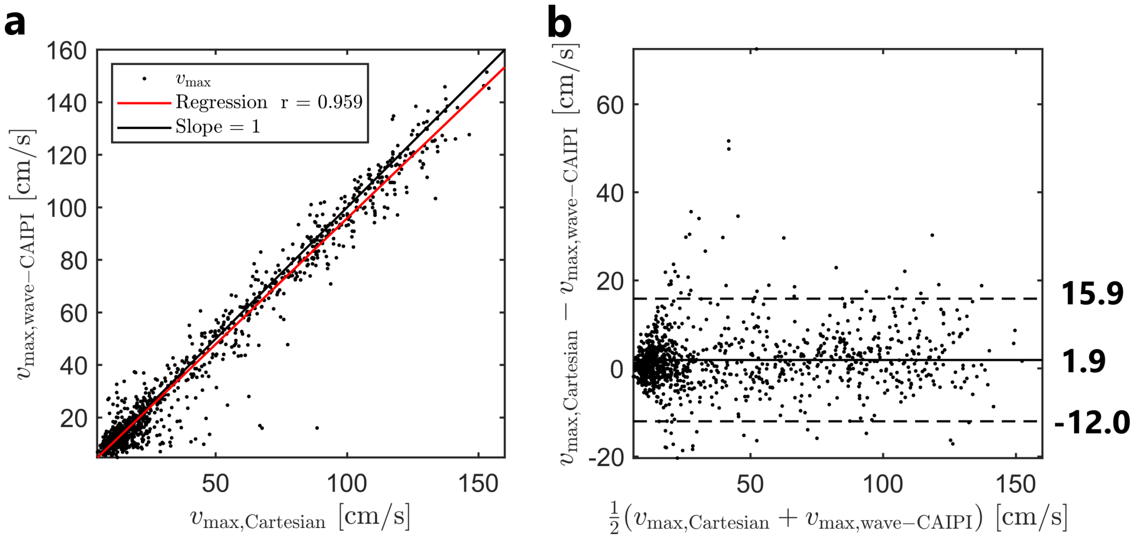

Figure 4.10: (a) Correlation plot and linear regression, comparing the individual peak velocity values of 2-fold accelerated wave-CAIPI and Cartesian 4D flow scans for 10 healthy volunteers. (b) Bland-Altman plot, comparing the peak velocity of 2-fold accelerated wave-CAIPI and Cartesian 4D flow scans. Previously published in [56] under the CC BY-NC 4.0 license (modified).

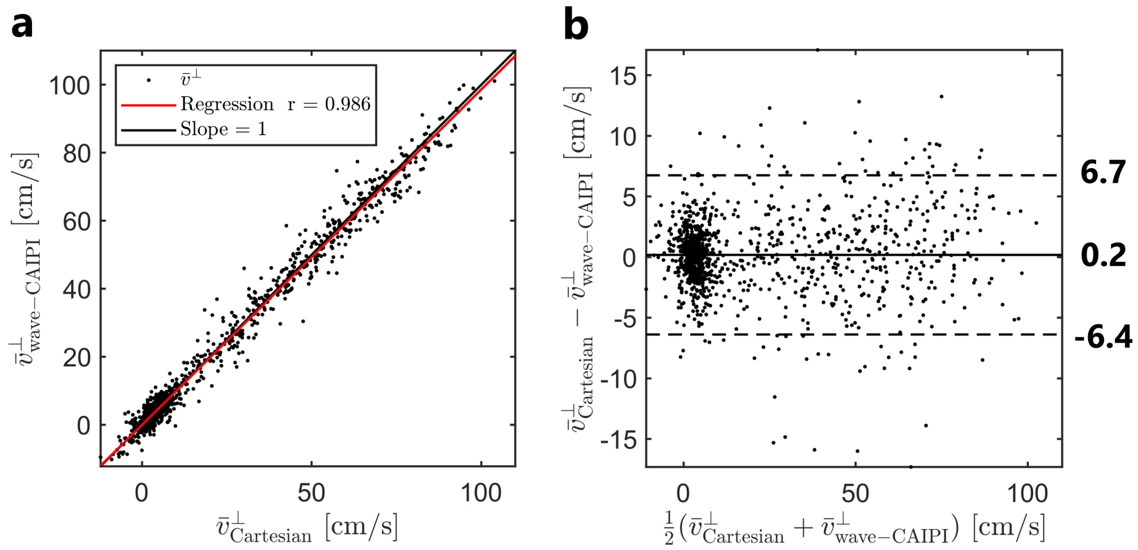

Figure 4.11: (a) Correlation plot and linear regression, comparing the individual values of the net average through-plane velocity of 2-fold accelerated wave-CAIPI and Cartesian 4D flow scans for 10 healthy volunteers. (b) Bland-Altman plot, comparing the net average through-plane velocity of 2-fold accelerated wave-CAIPI and Cartesian 4D flow scans. Previously published in [56] under the CC BY-NC 4.0 license (modified).

# Vol.	ΔQ [ml/s]	ΔQ_{net} [ml]	Δv_{max} [cm/s]	$\Delta \bar{v}^{\perp}$ [cm/s]
1	-0.61 ± 7.97	0.41 ± 2.05	0.34 ± 3.25	-0.23 ± 2.10
2	$3.52 \pm 9.84^*$	-2.38 ± 3.01	$1.41 \pm 4.77^*$	$0.97 \pm 2.42^*$
3	0.91 ± 16.63	-0.62 ± 4.36	$2.61 \pm 7.81^*$	0.33 ± 3.50
4	$2.05 \pm 10.31^*$	-1.39 ± 2.96	$2.25 \pm 5.10^*$	$0.43 \pm 2.10^*$
5	-0.68 ± 9.72	0.46 ± 2.17	$0.60 \pm 4.16^*$	-0.14 ± 2.65
6	$5.58 \pm 21.75^*$	$-3.77 \pm 4.35^*$	$3.86 \pm 8.35^*$	$1.46 \pm 4.89^*$
7	-0.62 ± 10.59	0.42 ± 3.77	$2.28 \pm 6.78^*$	-0.14 ± 2.79
8	-1.24 ± 13.58	0.84 ± 4.69	-1.10 ± 5.40	-0.30 ± 3.05
9	-0.19 ± 10.36	0.10 ± 3.05	$4.16 \pm 12.88^*$	-0.11 ± 2.78
10	-1.96 ± 17.85	1.32 ± 5.44	$3.35 \pm 7.82^*$	-0.54 ± 5.11

Table 4.2: Average differences in flow parameters Q, Q_{net}, v_{max} and $\bar{v}^{\perp}$ between wave-CAIPI and Cartesian 4D flow acquisitions with $R = 2$ for 10 healthy volunteers. The asterisk* denotes a statistically significant difference (5% significance level)

Fig. 4.12 shows correlation and Bland-Altman plots, comparing the flow rate measured in 10 healthy volunteers for an acceleration factor of $R = 6$ and $R = 2$ in the case of wave-CAIPI and Cartesian/2D-CAIPI sampling. The correlation and Bland-Altman plots for the net flow, the peak velocity and the net average through-plane velocity are presented in Figs. 4.13, 4.14 and 4.15, respectively. For each volunteer examination, a paired Wilcoxon signed rank test was performed to investigate the statistical significance of the difference in flow parameters between the 2-fold and the 6-fold accelerated scans, for wave-CAIPI and Cartesian/2D-CAIPI sampling. The mean and the standard deviation of the difference in flow parameters for the 10 volunteer examinations are presented in Tab. 4.3 (wave-CAIPI) and Tab. 4.4 (Cartesian/2D-CAIPI), along with the evaluation of statistical significance of the difference. For the wave-CAIPI, the null hypothesis was rejected in 4/10 cases for Q, in 1/10 cases for Q_{net}, in 9/10 cases for v_{max} and in 4/10 cases for $\bar{v}^{\perp}$. For the Cartesian/2D-CAIPI acquisition, the null hypothesis was rejected in 7/10 cases for Q, in 2/10 cases for Q_{net}, in 10/10 cases for v_{max} and in 6/10 cases for $\bar{v}^{\perp}$.

# Vol.	ΔQ [ml/s]	ΔQ_{net} [ml]	Δv_{max} [cm/s]	$\Delta \bar{v}^{\perp}$ [cm/s]
1	0.59 ± 7.56	0.40 ± 2.54	$-2.09 \pm 4.31^{*}$	0.24 ± 2.30
2	0.12 ± 7.52	-0.75 ± 2.50	$-3.81 \pm 6.56^{*}$	0.24 ± 2.04
3	0.11 ± 14.73	0.75 ± 4.69	$-4.49 \pm 10.18^{*}$	0.41 ± 3.11
4	$0.71 \pm 11.67^{*}$	3.18 ± 4.81	$-3.93 \pm 6.89^{*}$	$0.58 \pm 2.33^{*}$
5	$0.91 \pm 7.62^{*}$	$3.32 \pm 3.05^{*}$	0.49 ± 3.91	$1.28 \pm 1.82^{*}$
6	0.13 ± 17.73	0.09 ± 5.43	$-8.81 \pm 12.02^{*}$	0.07 ± 4.54
7	$0.63 \pm 10.75^{*}$	2.45 ± 4.19	$-3.70 \pm 8.72^{*}$	$1.00 \pm 2.77^{*}$
8	$0.93 \pm 16.64^{*}$	4.68 ± 6.72	$-3.66 \pm 8.69^{*}$	$1.36 \pm 3.64^{*}$
9	0.27 ± 16.32	2.27 ± 5.19	$-1.64 \pm 7.59^{*}$	1.11 ± 4.15
10	0.51 ± 9.95	1.02 ± 2.97	$-2.48 \pm 7.01^{*}$	0.42 ± 2.96

Table 4.3: Average differences in flow parameters Q, Q_{net}, v_{max} and $\bar{v}^{\perp}$ between wave-CAIPI 4D flow acquisitions with $R = 2$ and $R = 6$ for 10 healthy volunteers. The asterisk* denotes a statistically significant difference (5% significance level)

# Vol.	ΔQ [ml/s]	ΔQ_{net} [ml]	Δv_{max} [cm/s]	$\Delta \bar{v}^{\perp}$ [cm/s]
1	$-1.99 \pm 11.50^*$	-1.34 ± 5.14	$-6.73 \pm 10.55^*$	-0.12 ± 3.42
2	$7.11 \pm 11.08^*$	$4.80 \pm 2.16^*$	$-5.78 \pm 10.36^*$	$1.87 \pm 3.07^*$
3	-4.03 ± 24.47	-2.72 ± 8.24	$-14.24 \pm 20.06^*$	-1.28 ± 5.90
4	0.88 ± 20.06	0.60 ± 6.36	$-23.93 \pm 30.21^*$	0.20 ± 4.41
5	0.68 ± 15.03	0.46 ± 6.85	$-3.81 \pm 7.60^*$	-0.50 ± 4.57
6	$8.68 \pm 24.79^*$	5.96 ± 10.27	$-14.54 \pm 18.74^*$	$2.22 \pm 6.21^*$
7	$3.69 \pm 16.02^*$	2.49 ± 6.92	$-13.45 \pm 15.95^*$	$1.20 \pm 4.40^*$
8	$6.41 \pm 21.35^*$	4.33 ± 8.53	$-15.54 \pm 17.09^*$	$1.33 \pm 5.02^*$
9	$11.77 \pm 22.32^*$	$6.25 \pm 7.47^*$	$-12.91 \pm 19.36^*$	$3.78 \pm 7.46^*$
10	$3.61 \pm 14.32^*$	2.44 ± 2.52	$-7.54 \pm 12.10^*$	$0.96 \pm 4.27^*$

Table 4.4: Average differences in flow parameters Q, Q_{net}, v_{max} and $\bar{v}^{\perp}$ between Cartesian/2D-CAIPI 4D flow acquisitions with $R = 2$ and $R = 6$ for 10 healthy volunteers. The asterisk* denotes a statistically significant difference (5% significance level)

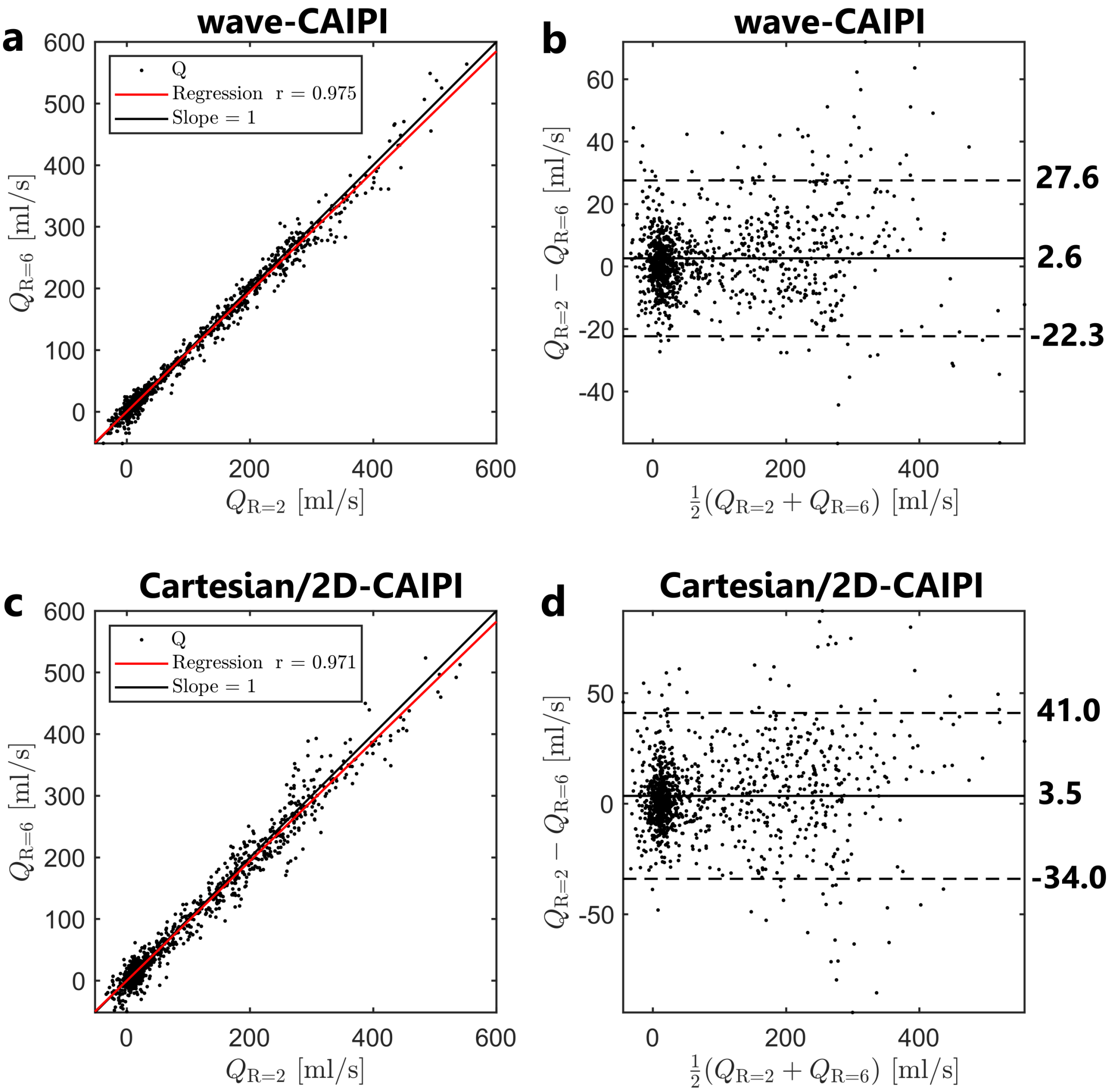

Figure 4.12: Comparison of flow rate calculations from 6-fold and 2-fold accelerated 4D flow MRIs. (a) and (c) show correlations plots and linear regressions of the individual flow rate values for wave-CAIPI and Cartesian/2D-CAIPI sampling, respectively. (b) and (d) show Bland-Altman plots of the flow rates for wave-CAIPI and Cartesian/2D-CAIPI sampling, respectively. Previously published in [56] under the CC BY-NC 4.0 license (modified).

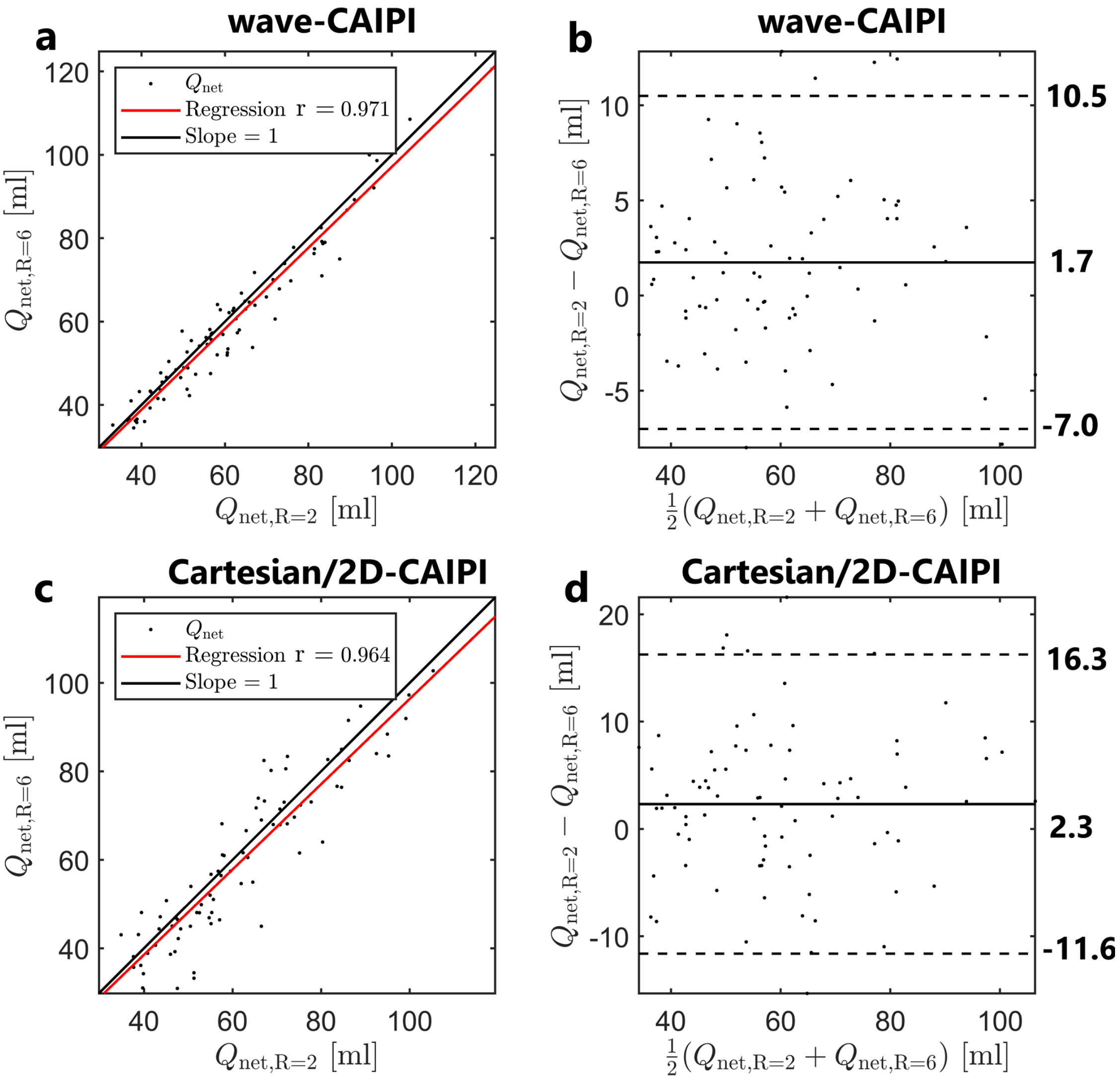

Figure 4.13: Comparison of net flow calculations from 6-fold and 2-fold accelerated 4D flow MRIs. (a) and (c) show correlations plots and linear regressions of the individual net flow values for wave-CAIPI and Cartesian/2D-CAIPI sampling, respectively. (b) and (d) show Bland-Altman plots of the net flow for wave-CAIPI and Cartesian/2D-CAIPI sampling, respectively. Previously published in [56] under the CC BY-NC 4.0 license (modified).

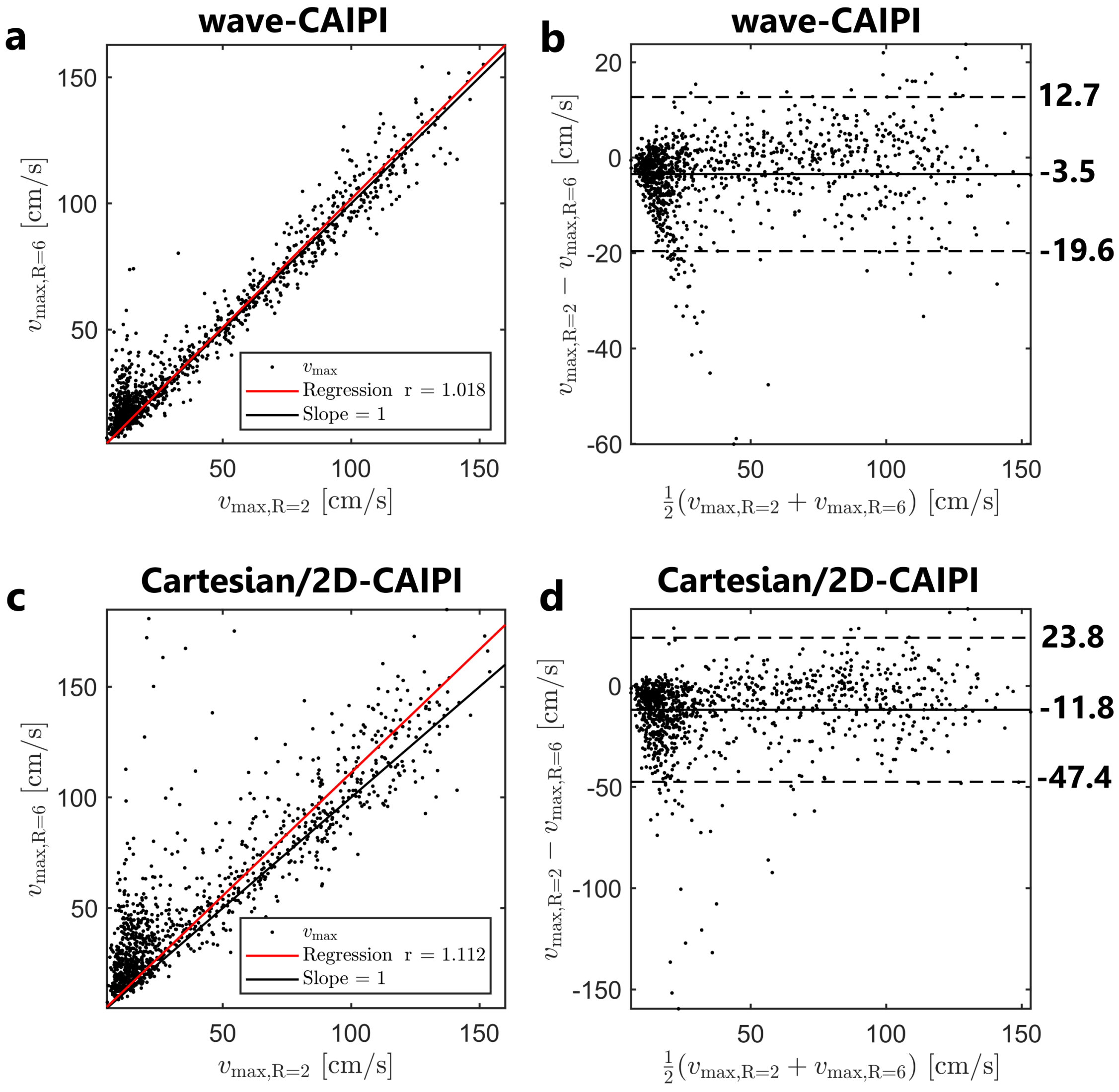

Figure 4.14: Comparison of peak velocity calculations from 6-fold and 2-fold accelerated 4D flow MRIs. (a) and (c) show correlations plots and linear regressions of the individual peak velocity values for wave-CAIPI and Cartesian/2D-CAIPI sampling, respectively. (b) and (d) show Bland-Altman plots of the peak velocity for wave-CAIPI and Cartesian/2D-CAIPI sampling, respectively. Previously published in [56] under the CC BY-NC 4.0 license.

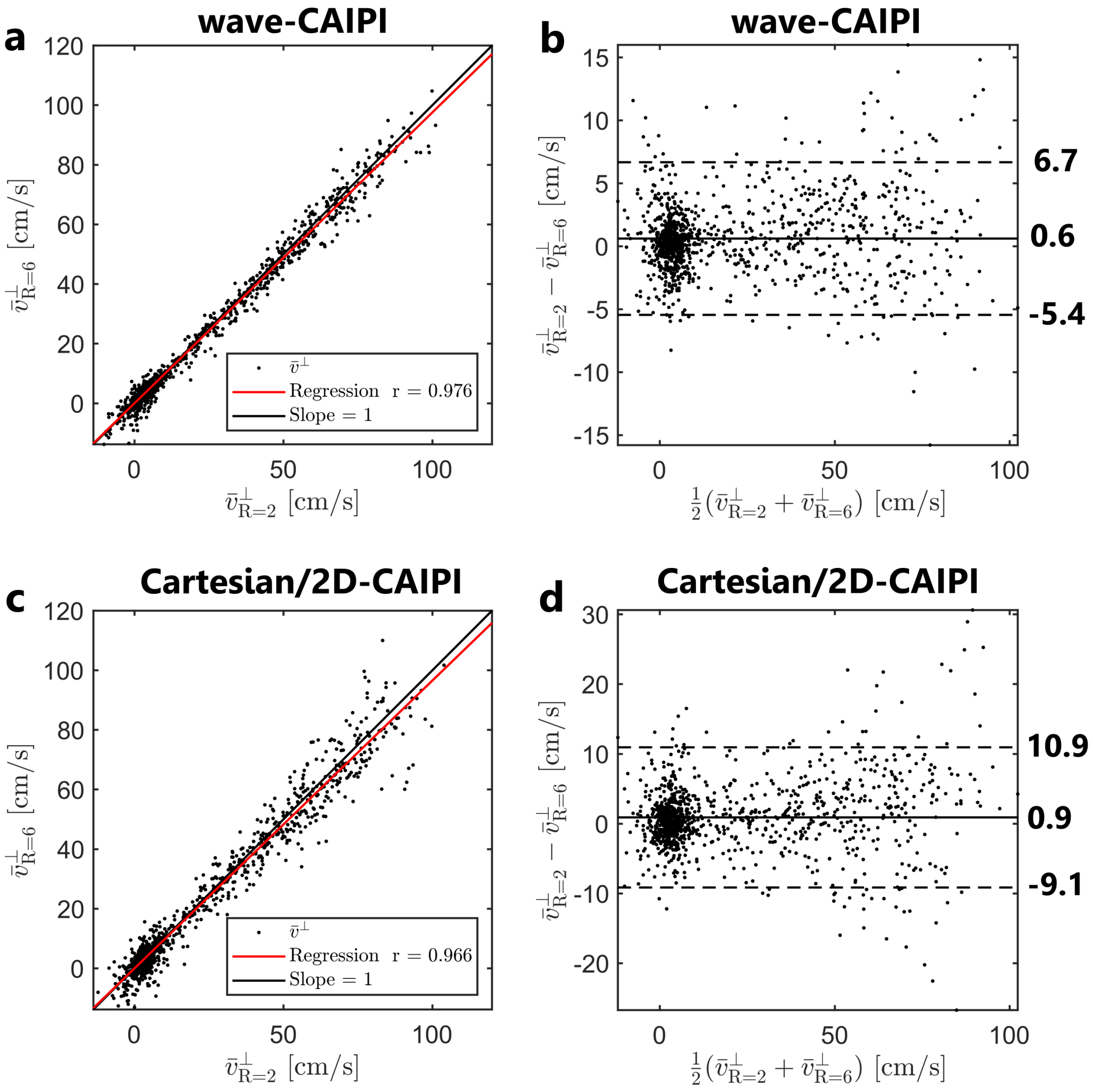

Figure 4.15: Comparison of net average through-plane velocity calculations from 6-fold and 2-fold accelerated 4D flow MRIs. (a) and (c) show correlations plots and linear regressions of the individual $\bar{v}^{\perp}$ values for wave-CAIPI and Cartesian/2D-CAIPI sampling, respectively. (b) and (d) show Bland-Altman plots of the $\bar{v}^{\perp}$ values for wave-CAIPI and Cartesian/2D-CAIPI sampling, respectively. Previously published in [56] under the CC BY-NC 4.0 license.

The measured flow in the aorta was visualized by means of streamlines for an exemplary volunteer examination in Fig. 4.16a. Streamline visualizations during systole are shown for the retrospectively 6-fold accelerated scan and the 2-fold accelerated reference scan. In the case of Cartesian sampling, differences in the flow pattern can be observed, especially in the descending aorta. For wave-CAIPI sampling, the streamline visualizations for $R = 2$ and $R = 6$ are very similar and exhibit only minor discrepancies. Fig. 4.16b presents particle traces during systole, where particle generation was performed in a plane near the aortic root. The 6-fold accelerated Cartesian acquisition underestimates the flow velocity near the aortic root, in comparison to the 2-fold accelerated scan. For wave-CAIPI sampling, the particle trace representations for $R = 2$ and $R = 6$ are very similar.

In Fig. 4.17, flow velocity is represented as velocity vectors in the same volunteer examination as in Fig. 4.16 during systole. The 6-fold accelerated wave-CAIPI acquisition yields velocity vectors very similar to those of the 2-fold accelerated scan. In the Cartesian/2D-CAIPI case, the velocity vectors reveal an underestimation of flow velocity near the aortic root (as in Fig. 4.16b) and an overestimation of flow velocity in the descending aorta (as in Fig. 4.16a). Also the calculated flow curves (in plane 1 and plane 8) show severe discrepancies between $R = 2$ and $R = 6$ for Cartesian/2D-CAIPI sampling. In case of the wave-CAIPI trajectory, deviations in flow curves are considerably smaller.

Velocity vectors and streamlines that were calculated from the examination of the patient with known aortic valve stenosis are shown in Fig. 4.18 for 2-fold and 6-fold acceleration. The patient was examined only with the wave-CAIPI 4D flow pulse sequence. The streamline visualization clearly shows an increased localized flow velocity along the outer wall of the ascending aorta, which is typical for patients with aortic valve stenosis. In the vector representation, as well as in

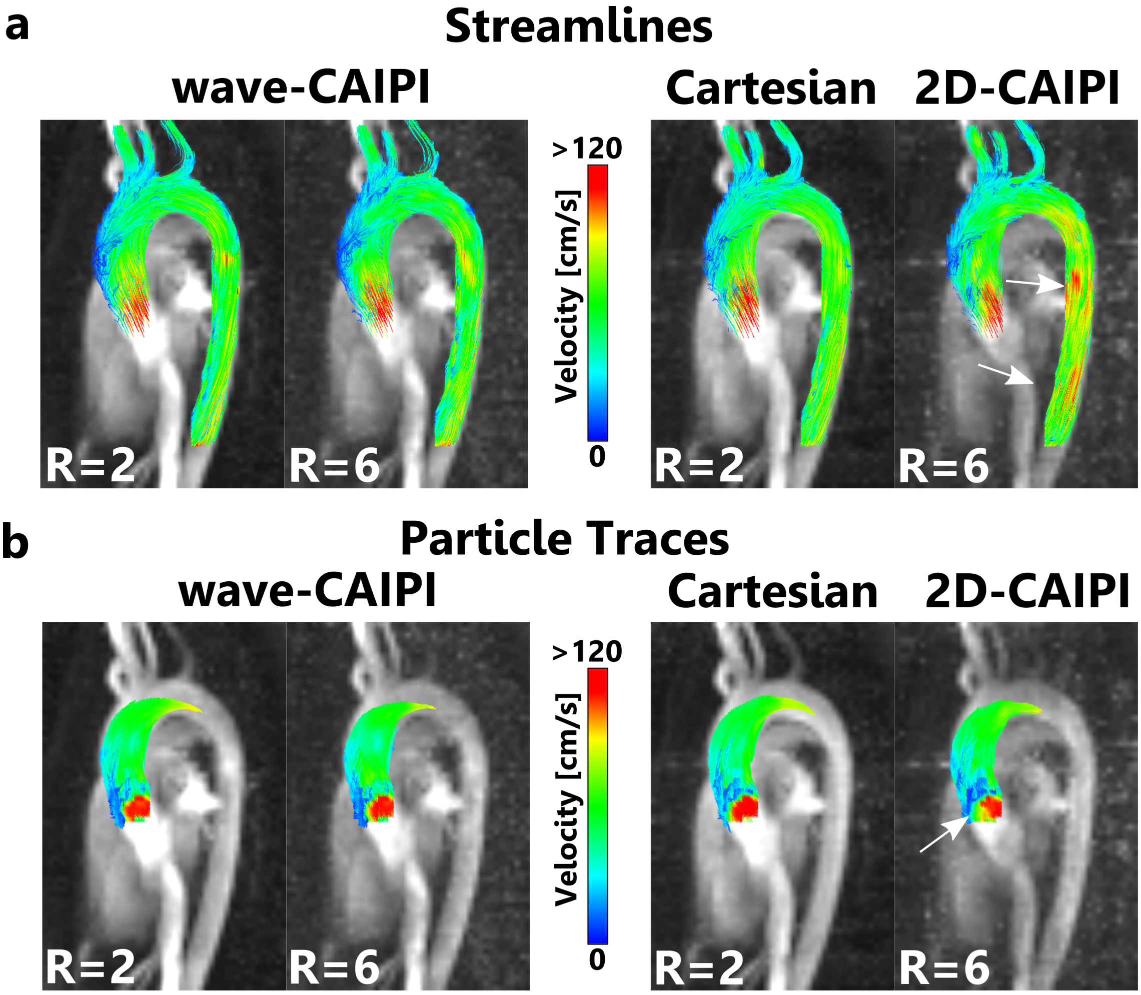
a
Streamlines
wave-CAIPI
Cartesian
2D-CAIPI
>120
Velocity [cm/s]
0
R=2
R=6
R=2
R=6
b
Particle Traces
wave-CAIPI
Cartesian
2D-CAIPI
>120
Velocity [cm/s]
0
R=2
R=6
R=2
R=6

Figure 4.16: Comparison of streamline visualizations (a) and particle trace representations (b) of flow velocity in the aorta of a healthy volunteer for 2-fold and 6-fold accelerated scans in sagittal orientation. White arrows point to regions in the 6-fold accelerated scans that exhibit noticeable discrepancies to the 2-fold accelerated scans. Previously published in [56] under the CC BY-NC 4.0 license.

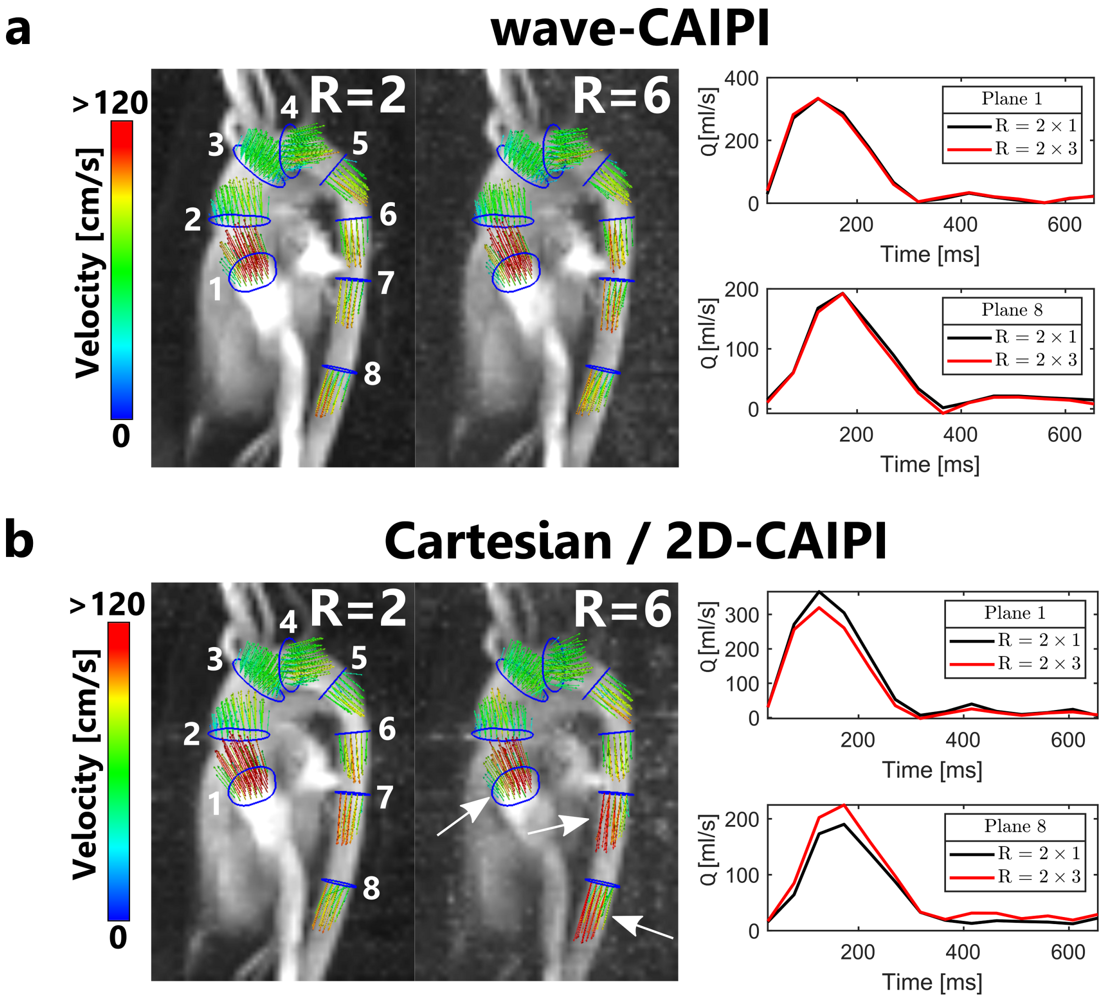
a
wave-CAIPI
>120
Velocity [cm/s]
0
R=2
R=6
1
2
3
4
5
6
7
8
Q [ml/s]
Time [ms]
Plane 1
R = 2 × 1
R = 2 × 3
Plane 8
0
100
200
300
400
600
b
Cartesian / 2D-CAIPI

Figure 4.17: Vector representation of aortic flow velocity in 8 planes for wave-CAIPI (a) and Cartesian/2D-CAIPI sampling (b) during systole, in sagittal orientation. The flow visualizations are compared for a 2-fold and a 6-fold retrospectively accelerated scan. Flow rates are calculated in plane 1 and plane 8 and are presented as flow curves. White arrows point to regions in the 6-fold accelerated scans that exhibit noticeable discrepancies to the 2-fold accelerated scans. Previously published in [56] under the CC BY-NC 4.0 license.

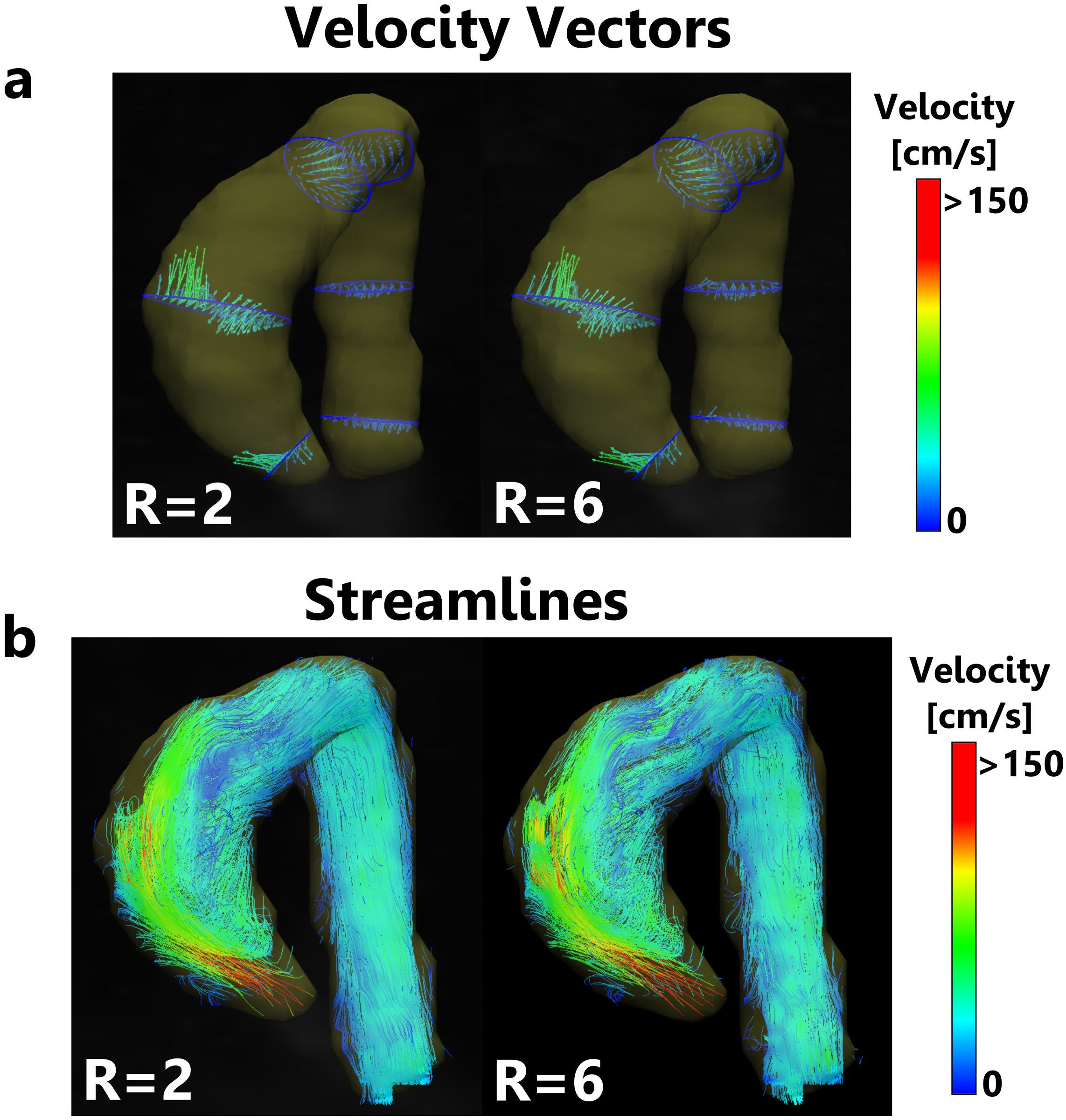
Velocity Vectors
a
R=2
R=6
Velocity
[cm/s]
>150
0
Streamlines
b
R=2
R=6
Velocity
[cm/s]
>150
0

Figure 4.18: Flow velocity vectors (a) and streamlines (b), calculated from a wave-CAIPI 4D flow examination of a patient with known aortic valve stenosis. Visualizations are compared for the 2-fold accelerated reference scan and the 6-fold retrospectively accelerated scan. Previously published in [56] under the CC BY-NC 4.0 license.

the streamline visualization, differences between the retrospectively 6-fold accelerated scan and the 2-fold accelerated reference are minor. The peak flow velocity near the aortic root was calculated to be $v_{\max} = 237.2\,\mathrm{cm/s}$ in the 2-fold accelerated scan and $v_{\max} = 225.9\,\mathrm{cm/s}$ in the 6-fold accelerated reference, which corresponds to an underestimation of 4.8%. Mean absolute differences and mean signed differences in flow parameters between $R = 2$ and $R = 6$ are shown in Tab. 4.5 for the patient examination.

$\langle \Delta Q \rangle$ [ml/s]	$\langle \Delta Q_{\mathrm{net}} \rangle$ [ml]	$\langle \Delta v_{\max} \rangle$ [cm/s]	$\langle \Delta \bar{v}^{\perp} \rangle$ [cm/s]
2.8 ± 10.9	1.9 ± 3.0	-4.8 ± 9.2	0.42 ± 2.11
$L_1(\Delta Q)$ [ml/s]	$L_1(\Delta Q_{\mathrm{net}})$ [ml]	$L_1(\Delta v_{\max})$ [cm/s]	$L_1(\Delta \bar{v}^{\perp})$ [cm/s]
8.5 ± 7.4	2.7 ± 2.1	6.8 ± 7.8	1.7 ± 1.4

Table 4.5: Mean signed and absolute differences in flow parameters of a wave-CAIPI 4D flow examination of a patient with aortic valve stenosis between $R = 2$ and $R = 6$.

4.4 Discussion

The calculations of noise levels in 6-fold accelerated images clearly demonstrate a reduced noise level in the wave-CAIPI images after the iterative SENSE reconstruction (c.f. Fig. 4.6). Since the image was masked, setting sensitivity maps to zero outside of the imaged object, edges are visible in Fig. 4.6 that arise from aliasing of the image mask. The reduced noise level of the wave-CAIPI technique leads to more precise reconstructions of accelerated 4D flow acquisition and ultimately results in lower uncertainties in flow parameters, compared to Cartesian 4D flow acquisitions with the same acquisition time. The reduction of image noise by employing wave-CAIPI sampling can also be noted in the phase contrast images in Fig. 4.4. The 6-fold accelerated wave-CAIPI phase contrast images exhibit smaller discrepancies to the 2-fold accelerated phase contrast images, compared to Cartesian/2D-

CAIPI sampling. Flow quantification is therefore more precise in the wave-CAIPI case.

In most cases, the uncertainties in Q, Q_{net}, $v_{\max}$ and $\bar{v}^{\perp}$ are lower for the wave-CAIPI technique, as displayed in Fig. 4.7 by means of bar charts. In order to investigate possible systematic discrepancies between wave-CAIPI and Cartesian 4D flow examinations, the flow parameters from 2-fold accelerated wave-CAIPI and Cartesian scans were compared in Figs. 4.8, 4.9, 4.10 and 4.11. In part of the volunteer examinations, statistically significant differences in the calculated flow parameters were found between the wave-CAIPI and the Cartesian scan at 2-fold acceleration. The mean difference, however, was in most cases close to zero and in all cases smaller than the standard deviation (cf. Tab. 4.2). As this comparison involves two separate examinations, discrepancies in flow parameters could partly be explained by physiological differences [67].

Systematic differences between wave-CAIPI 4D flow acquisitions with $R = 2$ and $R = 6$ are also, in part, statistically significant (cf. Tab. 4.3). The magnitudes of the systematic differences between wave-CAIPI $R = 2$ and $R = 6$ are comparable to the differences between wave-CAIPI $R = 2$ and Cartesian $R = 2$. In the Cartesian case, systematic discrepancies between $R = 2$ and $R = 6$ are larger (Tab. 4.4). Tab. 4.1 shows that by using wave-CAIPI sampling instead of 2D-CAIPI sampling, the precision of calculated flow parameters can be enhanced in retrospectively 6-fold accelerated 4D flow MRI and the bias, introduced by undersampling, can be reduced. The observed range of variability in flow parameters of the 6-fold accelerated 4D flow acquisitions is comparable to previous reports on undersampled 4D flow MRI [65, 68].

Visualizations of aortic blood flow by means of streamlines, particle traces and velocity vectors (cf. Figs. 4.16 and 4.17) demonstrate a reduced error rate for the accelerated wave-CAIPI scans, compared to

Cartesian/2D-CAIPI sampling. As the noise level in the 6-fold accelerated wave-CAIPI scans is about 43% lower than in the corresponding Cartesian scans, alterations in flow representation due to undersampling are reduced. Furthermore, due to the incoherent appearance of aliasing artifacts of the wave-CAIPI sampling technique, any residual aliasing may not be as prominent as in the Cartesian case (cf. Fig. 2.5 in Chapter 2).

The wave-CAIPI 4D flow examination of the patient suffering from aortic valve stenosis clearly displays the typical localized flow acceleration at the outer wall of the ascending aorta (Fig. 4.18). Furthermore, an asymmetric flow profile is visible near the analysis plane at the aortic root. These flow alterations can be identified in the 2-fold and in the retrospectively 6-fold accelerated dataset. The 6-fold accelerated scan underestimated the peak velocity near the aortic root by 4.8%. Estimated uncertainties in the flow parameters Q, Q_{net}, v_{max} and $\bar{v}^{\perp}$ (Tab. 4.5) are within the expected range of variability, judging from the examinations of the healthy volunteers (Tab. 4.1 and Fig. 4.7).

In the presented work, the retrospective acceleration of the acquired data was limited to a total acceleration rate of $R = 6$. The choice of 6-fold undersampling was motivated by the objective of generating high-quality MR images. Image quality was compared in Fig. 4.4a for different acceleration rates. While clear delineation of the aorta is still possible for $R = 6$, higher acceleration complicates delineation as well as segmentation of the aorta. In previously reported brain and abdominal applications that use the wave-CAIPI technique, acceleration rates between $R = 6$ and $R = 16$ were used [14–19, 26, 69, 70]. The employed slab-selective RF excitation pulse in the presented work exhibited an imperfect excitation profile, i.e., the excited slab was considerably larger than the encoded FOV in slice direction. The difference between the encoded FOV and the excited FOV is visualized in Fig. 4.19 and is estimated to be around 33%. This leads to aliasing in the slice direction and therefore adds to the net undersampling factor. In order to prevent or reduce this aliasing, a longer excitation pulse, with a more defined excitation profile could be used. Alternatively, slice oversampling could be employed to increase the encoded FOV in slice direction. Both of these approaches, however, inherently imply an increased acquisition time.

In GRAPPA-based reconstructions, rather than the employed iterative SENSE algorithm, the aliasing in slice direction can be ignored, since GRAPPA also works reliably in cases where the imaged object is larger than the encoded FOV [71–73]. A GRAPPA-based reconstruction for wave-CAIPI was introduced in [69] for brain applications. However, this approach works best when a large number of wave cycles is chosen in the trajectory implementation. Since it is known that for the purpose of g-factor optimization, a large gradient wave amplitude is preferable [17, 18], choosing many wave cycles in the current setup may not be possible due to slew rate limitations. This could be mitigated by significantly reducing the readout bandwidth (thereby increasing the readout duration), which is not desirable for fast 4D flow acquisitions.

Recently, an interesting approach towards optimal scan efficiency regarding the respiratory motion navigator in 4D flow MRI was presented [66], using self-gating and retrospective image registration. Self-gating techniques for 4D flow MRI were also previously studied in [65, 74]. Retrospective self-gating has the advantage of retrospective adjustment of gating parameters and does not require manual placement of image-based navigator windows, as was the case in the presented work. Due to the employed prospective, image-based respiratory navigator, the total scan time was unpredictable, since it depended on the subject's specific breathing pattern, as well as the heart rate. Combining the wave-CAIPI 4D flow technique with respiratory self-gating would also facilitate examination scheduling, as the

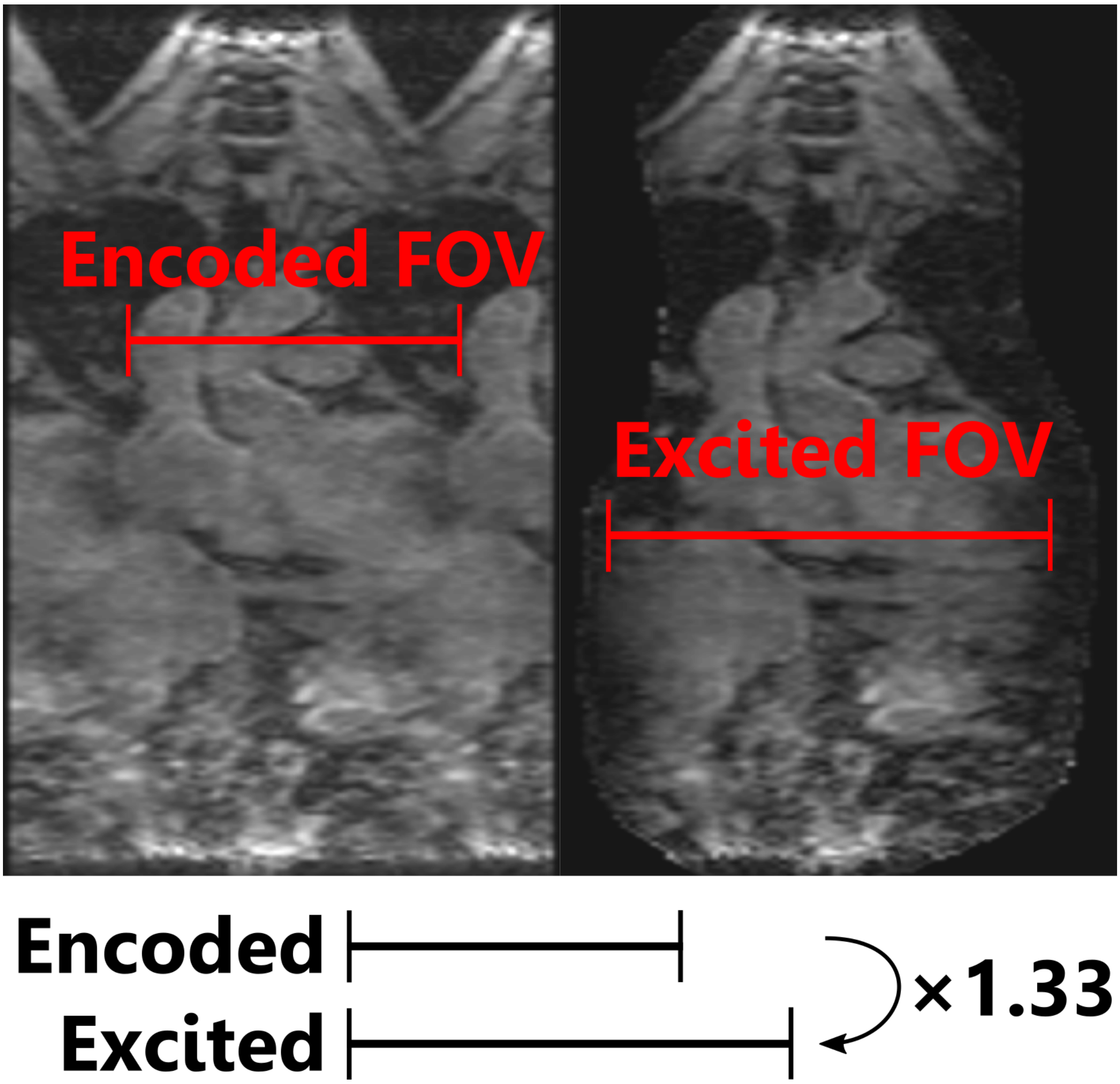
Encoded FOV
Excited FOV
Encoded
Excited
×1.33

Figure 4.19: Estimations of encoded and excited FOV in a 4D flow examination of a healthy volunteer. The encoded field of view can be estimated by measuring the distance between aliasing structures in the left image before the parallel imaging reconstruction. The excited field of view is estimated in the right image by measuring the extent of the imaged subject in left-right direction.

acquisition time could be reduced and could be predictable (at the expense of unknown sampling patterns).

To make use of temporal correlations in 4D flow datasets, k-t GRAPPA reconstructions can be employed [68, 75]. In [68], up to 8-fold acceleration of k-t GRAPPA 4D flow acquisitions were achieved. Similar to Compressed Sensing [3, 4] approaches, k-t GRAPPA bears the risk of reducing temporal fidelity of the image series, resulting, for instance, in an underestimation of peak velocities [68]. Several works on Compressed Sensing reconstructions for dynamic applications, such as 4D flow, were studied previously [5, 7, 9, 63]. By taking into account spatial and temporal correlations, high acceleration factor are achievable. In [7], for instance, 14.1-fold acceleration using a Cartesian spiral phyllotaxis sampling pattern was achieved, where high undersampling rates, however, also lead to increased blurring in the temporal domain. A promising combination of wave-CAIPI encoding and Compressed Sensing reconstructions is presented in [76], for brain applications. An interesting extension of the presented work would be the reconstruction of wave-CAIPI 4D flow examinations using a Compressed Sensing model that takes into account temporal correlations, such as the L+S (Low rank + Sparse) model [77]. In order to create different incoherent undersampling artifacts for each cardiac phase, the sampling pattern of the current setup would have to be adjusted.

The study population of this work was predominantly comprised of young, healthy volunteers. When applying the proposed method to patients, challenges can arise. Different patient body habitus may require adjustment of sampling parameters. Furthermore, pathological hemodynamic patterns may be more difficult to capture with 4D flow MRI. In patients with aortic valve stenosis, for instance, increased flow velocities may require a larger maximum encoded flow velocity, which leads to overall increased noise in flow quantification.

The current setup is limited by its offline reconstruction. For the presented method to be integrated into clinical routine, reconstruction needs to be implemented directly at the MR scanner. Moreover, the long reconstruction times (about one hour for a 6-fold accelerated 4D flow acquisition) need to be reduced to a clinically acceptable range. For artifact-free wave-CAIPI reconstructions, the gradient system transfer function was employed, which requires additional characterization of the scanner's gradient system using phantom measurements. For an automated workflow, an autocalibrating approach could be implemented, using data consistency to estimate gradient errors [17].

4.5 Conclusion

In conclusion, the wave-CAIPI technique enables parallel imaging reconstructions of 4D flow acquisitions with reduced noise enhancement, leading to higher SNR in undersampled images. As a consequence, the uncertainties in flow parameters could be reduced by up to 55% in 6-fold accelerated 4D flow examinations. Differences in flow parameters between Cartesian and wave-CAIPI acquisitions, as well as between 2-fold and 6-fold accelerated wave-CAIPI acquisitions are small but – in part – statistically significant. Only minor differences in blood flow visualization occur in accelerated wave-CAIPI examinations.

5 | Summary

In summary, the wave-CAIPI k-space trajectory presents an efficient sampling strategy for accelerated MR acquisitions. Using wave-CAIPI in parallel imaging reconstructions leads to a reduced noise level in the reconstructed images, compared to the Cartesian standard trajectory. This effect could be quantified by means of noise and SNR calculations. An SNR gain can be traded for a reduced scan time, i.e., additional undersampling, or for an enhanced image quality, keeping scan time constant.

Acceleration of MR imaging is especially important in dynamic applications, since these examinations are inherently time-consuming. The impact of wave-CAIPI sampling on image quality and its potential for scan time reduction was investigated for two dynamic applications: self-gated dynamic 3D lung MRI during free breathing and cardiac 4D flow MRI.

Dynamic 3D Lung MRI

By employing wave-CAIPI sampling in self-gated, free-breathing dynamic 3D lung MRI for the purpose of radiotherapy treatment planning, the image quality of accelerated scans could be enhanced. Volunteer examinations were used to quantify image quality by means of similarity between accelerated and reference images. To this end, the normalized mutual information and the root-mean-square error were chosen as quantitative image similarity measures.

The wave-CAIPI sampling was shown to exhibit superior quality, especially for short scan times. The values of the normalized mutual information were $(10.2 \pm 7.3)\%$ higher in the wave-CAIPI case – the root-mean-square error was $(18.9 \pm 13.2)\%$ lower on average. SNR calculations suggest an average SNR benefit of around 14% for the wave-CAIPI, compared to Cartesian sampling.

Resolution of the lung in 8 breathing states can be achieved in only 2 minutes. By using the wave-CAIPI k-space trajectory, precise tumor delineation and assessment of respiration-induced displacement is facilitated.

Cardiac 4D Flow MRI

In 4D flow MRI, acceleration of the image acquisition is essential to incorporate the corresponding scan protocols into clinical routine. In this work, a retrospective 6-fold acceleration of the image acquisition was realized. Cartesian and wave-CAIPI 4D flow examinations of healthy volunteers were used to quantify uncertainties in flow parameters for the respective sampling schemes.

By employing wave-CAIPI sampling, the estimated errors in flow parameters in 6-fold accelerated scans could be reduced by up to 55%. Noise calculations showed that the noise level in 6-fold accelerated 4D flow acquisitions with wave-CAIPI is 43% lower, compared to Cartesian sampling. Comparisons between Cartesian and wave-CAIPI 4D flow examinations with a prospective acceleration factor $R = 2$ revealed small, but partly statistically significant discrepancies. Differences between 2-fold and 6-fold accelerated wave-CAIPI scans are comparable to the differences between Cartesian and wave-CAIPI examinations at $R = 2$.

Wave-CAIPI 4D flow acquisitions of the aorta could be performed with an average, simulated scan time of under 4 minutes, with reduced uncertainties in flow parameters. Important visualizations of hemodynamic flow patterns in the aorta were only slightly affected by undersampling in the wave-CAIPI case, whereas for Cartesian sampling, considerable discrepancies were observed.

6 | Zusammenfassung

Die wave-CAIPI k-Raum Trajektorie stellt eine effiziente Methode für beschleunigte MRT Akquisitionen dar. Die Benutzung der wave-CAIPI Trajektorie anstelle der kartesischen Standardmethode in der parallelen Bildgebung führt zu einem reduzierten Rausch-Niveau in den rekonstruierten Bildern. Dieser Effekt kann durch Berechnungen des Rauschpegels und des Signal-zu-Rausch Verhältnisses (SNR) quantifiziert werden. Das höhere Signal-zu-Rausch Verhältnis kann genutzt werden, um entweder die Akquisition durch eine höhere Unterabtastung zu beschleunigen, oder um die Bildqualität zu verbessern.

Die Beschleunigung von MRT Akquisitionen ist besonders in dynamischen Anwendungen wichtig, da diese Untersuchungen inhärent sehr zeitaufwendig sind. Der Einfluss der wave-CAIPI Methode auf die Bildqualität und das Beschleunigungspotenzial der Messung wurde in dieser Arbeit sowohl für selbst-navigierte, dynamische 3D Lungenbildgebung, als auch für 4D Fluss MRTs des Herzens untersucht

Dynamische 3D Lungen MRT

Durch die Verwendung der wave-CAIPI Samplingmethode konnte die Bildqualität von selbst-navigierten, dynamischen 3D Lungen MRTs bei freier Atmung verbessert werden. Eine wichtige Anwendung dieser Technik liegt im Bereich der Strahlentherapieplanung. Dabei wurde im Rahmen einer Probandenstudie die Bildqualität anhand der Ähnlichkeit zwischen beschleunigten Bildern und den jeweiligen Referenzen quantifiziert. Zu diesem Zweck wurden die normalized mutual information und der root-mean-square error als quantitative Maße gewählt.

Es konnte gezeigt werden, dass – besonders bei kurzen Akquisitionszeiten – die wave-CAIPI Methode zu besserer Bildqualität führte, verglichen mit dem kartesischen Standard. Berechnungen der normalized mutual information ergaben im Mittel $(10.2 \pm 7.3)\%$ höhere Werte für die wave-CAIPI Methode – der root-mean-square error war $(18.9 \pm 13.2)\%$ geringer. Darüber hinaus lieferte die wave-CAIPI ein um etwa 14% höheres mittleres SNR.

In 2 Minuten konnte die Atembewegung der Lunge in 8 Atemzustände aufgelöst werden. Eine präzise Tumor-Abgrenzung und die Evaluierung von respirationsinduzierten Tumorbewegungen wird durch die Verwendung der wave-CAIPI Methode vereinfacht.

4D Fluss Herz MRT

Die Beschleunigung von 4D Fluss MRTs ist essentiell, um solche Untersuchungen in die klinische Routine zu integrieren. In der präsentierten Arbeit wurde eine 6-fache retrospektive Beschleunigung realisiert. 4D Fluss Untersuchungen von gesunden Probanden mit der wave-CAIPI und mit der kartesischen Samplingmethode wurden verwendet, um Unsicherheiten in verschiedenen Flussparametern für die beiden Samplingmethoden zu berechnen.

Dabei zeigte sich, dass die geschätzten Fehler in den Flussparametern der 6-fach beschleunigten wave-CAIPI Untersuchungen bis zu 55% geringer sind als die Fehler der kartesischen Messungen. Ferner zeigten Rausch-Analysen, dass die beschleunigten wave-CAIPI Aufnahmen ein um 43% geringeres Rausch-Niveau aufweisen. Vergleiche zwischen Flussparametern, die aus 2-fach beschleunigten wave-CAIPI und kartesischen Messungen berechnet wurden, zeigten kleine, aber teilweise statistisch signifikante Unterschiede zwischen den beiden Methoden. Unterschiede zwischen 2-fach und 6-fach beschleunigten wave-CAIPI Aufnahmen sind vergleichbar mit den Unterschieden zwischen der wave-CAIPI Methode und der kartesischen Methode bei $R = 2$.

Wave-CAIPI 4D Fluss Aufnahmen des Herzens konnten mit einer mittleren, simulierten Aufnahmezeit von unter 4 Minuten durchgeführt werden. Die effizientere Samplingmethode ermöglichte dabei erheblich reduzierte Unsicherheiten in den berechneten Flussparametern. Wichtige Visualisierungen des Blutflusses in der Aorta wurden im Falle der wave-CAIPI Methode kaum von der Unterabtastung beeinflusst. Hingegen wiesen die Visualisierungen der beschleunigten kartesischen Messungen erhebliche Diskrepanzen auf.

7 | Bibliography

[1] K. P. Pruessmann, M. Weiger, M. B. Scheidegger, and P. Boesiger, “SENSE: Sensitivity encoding for fast MRI”, *Magnetic Resonance in Medicine*, vol. 42, pp. 952–962, Nov. 1999.

[2] M. A. Griswold, P. M. Jakob, R. M. Heidemann, M. Nittka, V. Jellus, J. Wang, B. Kiefer, and A. Haase, “Generalized autocalibrating partially parallel acquisitions (GRAPPA)”, *Magnetic Resonance in Medicine*, vol. 47, pp. 1202–1210, June 2002.

[3] M. Lustig, D. Donoho, and J. M. Pauly, “Sparse MRI: The application of compressed sensing for rapid MR imaging”, *Magnetic Resonance in Medicine*, vol. 58, pp. 1182–1195, Dec. 2007.

[4] M. Lustig, D. L. Donoho, J. M. Santos, and J. M. Pauly, “Compressed sensing MRI”, *IEEE Signal Processing Magazine*, vol. 25, pp. 72–82, Mar. 2008.

[5] U. Gamper, P. Boesiger, and S. Kozerke, “Compressed sensing in dynamic MRI”, *Magnetic Resonance in Medicine*, vol. 59, pp. 365–373, Feb. 2008.

[6] T. Wech, A. Lemke, D. Medway, L.-A. Stork, C. A. Lygate, S. Neubauer, H. Köstler, and J. E. Schneider, “Accelerating cine-MR imaging in mouse hearts using compressed sensing”, *Journal of Magnetic Resonance Imaging*, vol. 34, pp. 1072–1079, Nov. 2011.

[7] L. E. Ma, M. Markl, K. Chow, H. Huh, C. Forman, A. Vali, A. Greiser, J. Carr, S. Schnell, A. J. Barker, and N. Jin, “Aortic 4d flow MRI in 2 minutes using compressed sensing, respiratory controlled adaptive k-space reordering, and inline reconstruction”, *Magnetic Resonance in Medicine*, vol. 81, pp. 3675–3690, June 2019.

[8] H. Dyvorne, A. Knight-Greenfield, G. Jajamovich, C. Besa, Y. Cui, A. Stalder, M. Markl, and B. Taouli, “Abdominal 4d Flow MR Imaging in a Breath Hold: Combination of Spiral Sampling and Dynamic Compressed Sensing for Highly Accelerated Acquisition”, *Radiology*, vol. 275, pp. 245–254, Oct. 2014.

[9] G. Valvano, N. Martini, A. Huber, C. Santelli, C. Binter, D. Chiappino, L. Landini, and S. Kozerke, “Accelerating 4d flow MRI by exploiting low-rank matrix structure and hadamard sparsity”, *Magnetic Resonance in Medicine*, vol. 78, no. 4, pp. 1330–1341, 2017.

[10] M. Stich, T. Wech, A. Slawig, R. Ringler, A. Dewdney, A. Greiser, G. Ruyters, T. A. Bley, and H. Köstler, “Gradient waveform preemphasis based on the gradient system transfer function”, *Magnetic Resonance in Medicine*, vol. 80, pp. 1521–1532, Oct. 2018.

[11] G. H. Glover and J. M. Pauly, “Projection Reconstruction Techniques for Reduction of Motion Effects in MRI”, *Magnetic Resonance in Medicine*, vol. 28, pp. 275–289, Dec. 1992.

[12] K. M. Johnson, S. B. Fain, M. L. Schiebler, and S. Nagle, “Optimized 3d ultrashort echo time pulmonary MRI”, *Magnetic Resonance in Medicine*, vol. 70, pp. 1241–1250, Nov. 2013.

[13] L. Mendes Pereira, T. Wech, A. Weng, C. Kestler, S. Veldhoen, T. Bley, and H. Köstler, “UTE-SENCEFUL: first results for 3d

high-resolution lung ventilation imaging", *Magnetic Resonance in Medicine*, vol. 81, pp. 2464–2473, Apr. 2019.

[14] B. Bilgic, B. A. Gagoski, S. F. Cauley, A. P. Fan, J. R. Polimeni, P. E. Grant, L. L. Wald, and K. Setsompop, "Wave-CAIPI for highly accelerated 3d imaging", *Magnetic Resonance in Medicine*, vol. 73, pp. 2152–2162, June 2015.

[15] S. F. Cauley, K. Setsompop, B. Bilgic, H. Bhat, B. Gagoski, and L. L. Wald, "Autocalibrated wave-CAIPI reconstruction; Joint optimization of k-space trajectory and parallel imaging reconstruction", *Magnetic Resonance in Medicine*, vol. 78, no. 3, pp. 1093–1099, 2017.

[16] D. Polak, K. Setsompop, S. F. Cauley, B. A. Gagoski, H. Bhat, F. Maier, P. Bachert, L. L. Wald, and B. Bilgic, "Wave-CAIPI for highly accelerated MP-RAGE imaging", *Magnetic Resonance in Medicine*, vol. 79, pp. 401–406, Jan. 2018.

[17] D. Polak, S. Cauley, S. Y. Huang, M. G. Longo, J. Conklin, B. Bilgic, N. Ohringer, E. Raithel, P. Bachert, L. L. Wald, and K. Setsompop, "Highly-accelerated volumetric brain examination using optimized wave-CAIPI encoding", *Journal of Magnetic Resonance Imaging*, Feb. 2019.

[18] H. Wang, Z. Qiu, S. Su, S. Jia, Y. Li, X. Liu, H. Zheng, and D. Liang, "Parameter optimization framework on wave gradients of Wave-CAIPI imaging", *Magnetic Resonance in Medicine*, vol. 83, Oct. 2019.

[19] F. Chen, T. Zhang, J. Y. Cheng, X. Shi, J. M. Pauly, and S. S. Vasanawala, "Autocalibrating motion-corrected wave-encoding for highly accelerated free-breathing abdominal MRI", *Magnetic Resonance in Medicine*, vol. 78, pp. 1757–1766, Nov. 2017.

[20] L.-C. Man, J. M. Pauly, and A. Macovski, “Improved automatic off-resonance correction without a field map in spiral imaging”, *Magnetic Resonance in Medicine*, vol. 37, pp. 906–913, June 1997.

[21] W. Chen and C. H. Meyer, “Semiautomatic off-resonance correction in spiral imaging”, *Magnetic Resonance in Medicine*, vol. 59, pp. 1212–1219, May 2008.

[22] S. J. Vannesjo, M. Haeberlin, L. Kasper, M. Pavan, B. J. Wilm, C. Barmet, and K. P. Pruessmann, “Gradient system characterization by impulse response measurements with a dynamic field camera”, *Magnetic Resonance in Medicine*, vol. 69, pp. 583–593, Feb. 2013.

[23] S. J. Vannesjo, N. N. Graedel, L. Kasper, S. Gross, J. Busch, M. Haeberlin, C. Barmet, and K. P. Pruessmann, “Image reconstruction using a gradient impulse response model for trajectory prediction”, *Magnetic Resonance in Medicine*, vol. 76, pp. 45–58, July 2016.

[24] A. E. Campbell-Washburn, H. Xue, R. J. Lederman, A. Z. Faranesh, and M. S. Hansen, “Real-time distortion correction of spiral and echo planar images using the gradient system impulse response function”, *Magnetic Resonance in Medicine*, vol. 75, pp. 2278–2285, June 2016.

[25] M. A. Bernstein, K. F. King, and X. J. Zhou, *Handbook of MRI pulse sequences.* Elsevier, 2004.

[26] J. A. J. Richter, T. Wech, A. M. Weng, M. Stich, S. Weick, K. Breuer, T. A. Bley, and H. Köstler, “Free-breathing self-gated 4d lung MRI using wave-CAIPI”, *Magnetic Resonance in Medicine*, vol. 84, pp. 3223–3233, July 2020.

[27] J. W. Cooley and J. W. Tukey, “An algorithm for the machine calculation of complex Fourier series”, *Mathematics of Computation*, vol. 19, no. 90, pp. 297–301, 1965.

[28] J. I. Jackson, C. H. Meyer, D. G. Nishimura, and A. Macovski, “Selection of a convolution function for Fourier inversion using gridding [computerised tomography application]”, *IEEE transactions on medical imaging*, vol. 10, no. 3, pp. 473–478, 1991.

[29] K. P. Pruessmann, M. Weiger, P. Börnert, and P. Boesiger, “Advances in sensitivity encoding with arbitrary k-space trajectories”, *Magnetic Resonance in Medicine*, vol. 46, pp. 638–651, Oct. 2001.

[30] P. Qu, K. Zhong, B. Zhang, J. Wang, and G. X. Shen, “Convergence behavior of iterative SENSE reconstruction with non-Cartesian trajectories”, *Magnetic Resonance in Medicine*, vol. 54, pp. 1040–1045, Oct. 2005.

[31] P. M. Robson, A. K. Grant, A. J. Madhuranthakam, R. Lattanzi, D. K. Sodickson, and C. A. McKenzie, “Comprehensive Quantification of Signal-to-Noise Ratio and g-Factor for Image-Based and k-Space-Based Parallel Imaging Reconstructions”, *Magnetic Resonance in Medicine*, vol. 60, pp. 895–907, Oct. 2008.

[32] F. A. Breuer, M. Blaimer, R. M. Heidemann, M. F. Mueller, M. A. Griswold, and P. M. Jakob, “Controlled aliasing in parallel imaging results in higher acceleration (CAIPIRINHA) for multi-slice imaging”, *Magnetic Resonance in Medicine*, vol. 53, pp. 684–691, Mar. 2005.

[33] F. A. Breuer, M. Blaimer, M. F. Mueller, N. Seiberlich, R. M. Heidemann, M. A. Griswold, and P. M. Jakob, “Controlled aliasing in volumetric parallel imaging (2d CAIPIRINHA)”, *Magnetic Resonance in Medicine*, vol. 55, pp. 549–556, Mar. 2006.

[34] M. v. Siebenthal, G. Székely, U. Gamper, P. Boesiger, A. Lomax, and P. Cattin, "4d MR imaging of respiratory organ motion and its variability", *Physics in Medicine and Biology*, vol. 52, pp. 1547–1564, Feb. 2007.

[35] J. Tokuda, S. Morikawa, H. A. Haque, T. Tsukamoto, K. Matsumiya, H. Liao, K. Masamune, and T. Dohi, "Adaptive 4d MR imaging using navigator-based respiratory signal for MRI-guided therapy", *Magnetic Resonance in Medicine*, vol. 59, pp. 1051–1061, May 2008.

[36] J. F. Arnold, P. Mörchel, E. Glaser, E. D. Pracht, and P. M. Jakob, "Lung MRI using an MR-compatible active breathing control (MR-ABC)", *Magnetic Resonance in Medicine*, vol. 58, pp. 1092–1098, Dec. 2007.

[37] Peter Speier, Matthias Fenchel, and Robert Rehner, "Pt-nav: A novel respiratory navigation method for continuous acquisition based on modulation of a pilot tone on the mr-receiver", in *Proc ESMRMB*, vol. 32, 2015.

[38] Lea Schroeder, Jens Wetzl, Andreas Maier, Robert Rehner, Matthias Fenchel, and Peter Speier, "Two-dimensional respiratory-motion characterization for continuous mr measurements using pilot tone navigation", in *Proc. Intl. Soc. Mag. Reson. Med.*, vol. 24, 2016.

[39] A. Fischer, S. Weick, C. O. Ritter, M. Beer, C. Wirth, H. Hebestreit, P. M. Jakob, D. Hahn, T. Bley, and H. Köstler, "SElf-gated Non-Contrast-Enhanced FUnctional Lung imaging (SENCEFUL) using a quasi-random fast low-angle shot (FLASH) sequence and proton MRI", *NMR in Biomedicine*, vol. 27, pp. 907–917, Aug. 2014.

[40] S. Weick, F. A. Breuer, P. Ehses, M. Völker, C. Hintze, J. Biederer, and P. M. Jakob, "DC-gated high resolution three-dimensional lung imaging during free-breathing", *Journal of Magnetic Resonance Imaging*, vol. 37, no. 3, pp. 727–732, 2013.

[41] M. E. Crowe, A. C. Larson, Q. Zhang, J. Carr, R. D. White, D. Li, and O. P. Simonetti, "Automated rectilinear self-gated cardiac cine imaging", *Magnetic Resonance in Medicine*, vol. 52, pp. 782–788, Oct. 2004.

[42] S. Weick, M. Völker, K. Hemberger, C. Meyer, P. Ehses, B. Polat, F. A. Breuer, M. Blaimer, C. Fink, L. R. Schad, O. A. Sauer, M. Flentje, and P. M. Jakob, "Desynchronization of Cartesian k-space sampling and periodic motion for improved retrospectively self-gated 3d lung MRI using quasi-random numbers", *Magnetic Resonance in Medicine*, vol. 77, no. 2, pp. 787–793, 2017.

[43] K. Breuer, C. B. Meyer, F. A. Breuer, A. Richter, F. Exner, A. M. Weng, S. Ströhle, B. Polat, P. M. Jakob, O. A. Sauer, M. Flentje, and S. Weick, "Stable and efficient retrospective 4d-MRI using non-uniformly distributed quasi-random numbers", *Physics in Medicine and Biology*, vol. 63, no. 7, p. 075002, 2018.

[44] J. Y. Cheng, T. Zhang, N. Ruangwattanapaisarn, M. T. Alley, M. Uecker, J. M. Pauly, M. Lustig, and S. S. Vasanawala, "Free-breathing pediatric MRI with nonrigid motion correction and acceleration", *Journal of Magnetic Resonance Imaging*, vol. 42, pp. 407–420, Aug. 2015.

[45] M. Matsumoto and T. Nishimura, "Mersenne Twister: A 623-dimensionally Equidistributed Uniform Pseudo-random Number Generator", *ACM Transactions on Modeling and Computer Simulations*, vol. 8, pp. 3–30, Jan. 1998.

[46] M. Uecker, P. Lai, M. J. Murphy, P. Virtue, M. Elad, J. M. Pauly, S. S. Vasanawala, and M. Lustig, “ESPIRiT-An Eigenvalue Approach to Autocalibrating Parallel MRI: Where SENSE Meets GRAPPA”, *Magnetic Resonance in Medicine*, vol. 71, pp. 990–1001, Mar. 2014.

[47] Martin Uecker, Frank Ong, Jonathan I Tamir, Dara Bahri, Patrick Virtue, Joseph Y Cheng, Tao Zhang, and Michael Lustig, “Berkeley Advanced Reconstruction Toolbox”, in *Proc. Intl. Soc. Mag. Reson. Med.*, vol. 23, 2015.

[48] E. C. Ford, G. S. Mageras, E. Yorke, and C. C. Ling, “Respiration-correlated spiral CT: a method of measuring respiratory-induced anatomic motion for radiation treatment planning”, *Medical Physics*, vol. 30, pp. 88–97, Jan. 2003.

[49] J. W. H. Wolthaus, J.-J. Sonke, M. van Herk, J. S. A. Belderbos, M. M. G. Rossi, J. V. Lebesque, and E. M. F. Damen, “Comparison of different strategies to use four-dimensional computed tomography in treatment planning for lung cancer patients”, *International Journal of Radiation Oncology, Biology, Physics*, vol. 70, pp. 1229–1238, Mar. 2008.

[50] J. W. H. Wolthaus, C. Schneider, J.-J. Sonke, M. van Herk, J. S. A. Belderbos, M. M. G. Rossi, J. V. Lebesque, and E. M. F. Damen, “Mid-ventilation CT scan construction from four-dimensional respiration-correlated CT scans for radiotherapy planning of lung cancer patients”, *International Journal of Radiation Oncology, Biology, Physics*, vol. 65, pp. 1560–1571, Aug. 2006.

[51] H. D. Heerkens, W. A. Hall, X. A. Li, P. Knechtges, E. Dalah, E. S. Paulson, C. a. T. van den Berg, G. J. Meijer, E. J. Koay,

C. H. Crane, K. Aitken, M. van Vulpen, and B. A. Erickson, "Recommendations for MRI-based contouring of gross tumor volume and organs at risk for radiation therapy of pancreatic cancer", *Practical Radiation Oncology*, vol. 7, pp. 126–136, Apr. 2017.

[52] A. D. Vellet, W. Romano, D. B. Bach, R. B. Passi, D. H. Taves, and P. L. Munk, "Adenocarcinoma of the pancreatic ducts: comparative evaluation with CT and MR imaging at 1.5 T.", *Radiology*, vol. 183, pp. 87–95, Apr. 1992.

[53] B. Vachiranubhap, Y. H. Kim, N. C. Balci, and R. C. Semelka, "Magnetic Resonance Imaging of Adenocarcinoma of the Pancreas", *Topics in Magnetic Resonance Imaging*, vol. 20, p. 3, Feb. 2009.

[54] H. Saisho and T. Yamaguchi, "Diagnostic Imaging for Pancreatic Cancer: Computed Tomography, Magnetic Resonance Imaging, and Positron Emission Tomography", *Pancreas*, vol. 28, p. 273, Apr. 2004.

[55] T. Zhang, J. Y. Cheng, Y. Chen, D. G. Nishimura, J. M. Pauly, and S. S. Vasanawala, "Robust self-navigated body MRI using dense coil arrays", *Magnetic Resonance in Medicine*, vol. 76, pp. 197–205, July 2016.

[56] J. A. J. Richter, T. Wech, A. M. Weng, M. Stich, N. Jin, A. Kosmala, T. A. Bley, and H. Köstler, "Accelerated aortic 4d flow mri with wave-CAIPI", *Magnetic Resonance in Medicine (in Production)*, 2020.

[57] M. Markl, A. Frydrychowicz, S. Kozerke, M. Hope, and O. Wieben, "4d flow MRI", *Journal of Magnetic Resonance Imaging*, vol. 36, pp. 1015–1036, Nov. 2012.

[58] P. Dyverfeldt, M. Bissell, A. J. Barker, A. F. Bolger, C.-J. Carlhall, T. Ebbers, C. J. Francios, A. Frydrychowicz, J. Geiger, D. Giese, M. D. Hope, P. J. Kilner, S. Kozerke, S. Myerson, S. Neubauer, O. Wieben, and M. Markl, "4d flow cardiovascular magnetic resonance consensus statement", *Journal of Cardiovascular Magnetic Resonance*, vol. 17, p. 72, Aug. 2015.

[59] M. D. Hope, T. A. Hope, S. E. S. Crook, K. G. Ordovas, T. H. Urbania, M. T. Alley, and C. B. Higgins, "4d Flow CMR in Assessment of Valve-Related Ascending Aortic Disease", *Jacc-Cardiovascular Imaging*, vol. 4, pp. 781–787, July 2011.

[60] M. Markl, P. J. Kilner, and T. Ebbers, "Comprehensive 4d velocity mapping of the heart and great vessels by cardiovascular magnetic resonance", *Journal of Cardiovascular Magnetic Resonance*, vol. 13, p. 7, Jan. 2011.

[61] S. A. Ansari, S. Schnell, T. Carroll, P. Vakil, M. C. Hurley, C. Wu, J. Carr, B. R. Bendok, H. Batjer, and M. Markl, "Intracranial 4d Flow MRI: Toward Individualized Assessment of Arteriovenous Malformation Hemodynamics and Treatment-Induced Changes", *American Journal of Neuroradiology*, vol. 34, pp. 1922–1928, Oct. 2013.

[62] T. Sekine, Y. Amano, R. Takagi, Y. Matsumura, Y. Murai, and S. Kumita, "Feasibility of 4d Flow MR Imaging of the Brain with Either Cartesian y-z Radial Sampling or k-t SENSE: Comparison with 4d Flow MR Imaging using SENSE", *Magnetic Resonance in Medical Sciences*, vol. 13, pp. 15–24, Mar. 2014.

[63] L. A. Rivera-Rivera, P. Turski, K. M. Johnson, C. Hoffman, S. E. Berman, P. Kilgas, H. A. Rowley, C. M. Carlsson, S. C. Johnson, and O. Wieben, "4d flow MRI for intracranial hemodynamics as-

sessment in Alzheimer's disease", *Journal of Cerebral Blood Flow & Metabolism*, vol. 36, pp. 1718–1730, Oct. 2016.

[64] A. L. Wentland, T. M. Grist, and O. Wieben, "Repeatability and internal consistency of abdominal 2d and 4d phase contrast MR flow measurements", *Academic Radiology*, vol. 20, pp. 699–704, June 2013.

[65] R. Bastkowski, K. Weiss, D. Maintz, and D. Giese, "Self-gated golden-angle spiral 4d flow MRI", *Magnetic Resonance in Medicine*, vol. 80, no. 3, pp. 904–913, 2018.

[66] C. Kolbitsch, R. Bastkowski, T. Schäffter, C. Prieto Vasquez, K. Weiss, D. Maintz, and D. Giese, "Respiratory motion corrected 4d flow using golden radial phase encoding", *Magnetic Resonance in Medicine*, vol. 83, pp. 635–644, Feb. 2020.

[67] V. M. Stoll, M. Loudon, J. Eriksson, M. M. Bissell, P. Dyverfeldt, T. Ebbers, S. G. Myerson, S. Neubauer, C.-J. Carlhäll, and A. T. Hess, "Test-retest variability of left ventricular 4d flow cardiovascular magnetic resonance measurements in healthy subjects", *Journal of Cardiovascular Magnetic Resonance*, vol. 20, p. 15, Mar. 2018.

[68] S. Schnell, M. Markl, P. Entezari, R. J. Mahadewia, E. Semaan, Z. Stankovic, J. Collins, J. Carr, and B. Jung, "k-t GRAPPA accelerated four-dimensional flow MRI in the aorta: effect on scan time, image quality, and quantification of flow and wall shear stress", *Magnetic Resonance in Medicine*, vol. 72, pp. 522–533, Aug. 2014.

[69] J. M. Schwarz, E. D. Pracht, D. Brenner, M. Reuter, and T. Stöcker, "GRAPPA reconstructed wave-CAIPI MP-RAGE at 7

Tesla", *Magnetic Resonance in Medicine*, vol. 80, pp. 2427–2438, Dec. 2018.

[70] J. Conklin, M. G. F. Longo, S. F. Cauley, K. Setsompop, R. G. González, P. W. Schaefer, J. E. Kirsch, O. Rapalino, and S. Y. Huang, "Validation of Highly Accelerated Wave–CAIPI SWI Compared with Conventional SWI and T2*-Weighted Gradient Recalled-Echo for Routine Clinical Brain MRI at 3t", *American Journal of Neuroradiology*, Nov. 2019.

[71] M. A. Griswold, S. Kannengiesser, R. M. Heidemann, J. Wang, and P. M. Jakob, "Field-of-view limitations in parallel imaging", *Magnetic Resonance in Medicine*, vol. 52, pp. 1118–1126, Nov. 2004.

[72] J. W. Goldfarb, "The SENSE ghost: Field-of-view restrictions for SENSE imaging", *Journal of Magnetic Resonance Imaging*, vol. 20, pp. 1046–1051, Dec. 2004.

[73] P. Noël, R. Bammer, C. Reinhold, and M. A. Haider, "Parallel imaging artifacts in body magnetic resonance imaging", *Canadian Association of Radiologists Journal = Journal l'Association Canadienne Des Radiologistes*, vol. 60, pp. 91–98, Apr. 2009.

[74] Aaron Pruitt, Adam Rich, Yingmin Liu, Ning Jin, Lee Potter, Orlando Simonetti, Rizwan Ahmad, "Self-gated 5-minute whole-heart 4d flow imaging", in *Proc. Intl. Soc. Mag. Reson. Med. 27*, (Montréal, Kanada), 2019.

[75] F. Huang, J. Akao, S. Vijayakumar, G. R. Duensing, and M. Limkeman, "k-t GRAPPA: A k-space implementation for dynamic MRI with high reduction factor", *Magnetic Resonance in Medicine*, vol. 54, pp. 1172–1184, Nov. 2005.

[76] T. H. Kim, B. Bilgic, D. Polak, K. Setsompop, and J. P. Haldar, "Wave-LORAKS: Combining wave encoding with structured low-rank matrix modeling for more highly accelerated 3d imaging", *Magnetic Resonance in Medicine*, vol. 81, pp. 1620–1633, Mar. 2019.

[77] R. Otazo, E. Candès, and D. K. Sodickson, "Low-rank plus sparse matrix decomposition for accelerated dynamic MRI with separation of background and dynamic components", *Magnetic Resonance in Medicine*, vol. 73, pp. 1125–1136, Mar. 2015.

A | Curriculum Vitae

B | Publications

Papers

M. Schrauth, J.A.J. Richter, J.S.E. Portela, ”Two-dimensional Ising model on random lattices with constant coordination number”, Physical Review E **98**, 022144 (2018)

M. Stich, J.A.J. Richter, T. Wech, T.A. Bley, R. Ringler, H. Köstler, A.E. Campbell-Washburn, ”Field Camera versus Phantom-based Measurement of the Gradient System Transfer Function (GSTF) with dwell time compensation”, Magnetic Resonance Imaging **71**, 125-131 (2020)

J.A.J. Richter, T. Wech, A.M. Weng, M. Stich, S. Weick, K. Breuer, T.A. Bley, H. Köstler, ”Free-Breathing Self-Gated 4D-Lung MRI using wave-CAIPI”, Magnetic Resonance in Medicine **84**, 3223-3233 (2020)

J.A.J. Richter, T. Wech, A.M. Weng, M. Stich, N. Jin, A. Kosmala, T.A. Bley, H. Köstler, ”Accelerated Aortic 4D Flow MRI with wave-CAIPI”, Accepted in Magnetic Resonance in Medicine (2020), DOI:10.1002/mrm.28605

Conference Abstracts

J.A.J. Richter, T. Wech, A.M. Weng, M. Stich, S. Veldhoen, S. Weick, T.A. Bley, H. Köstler, "Free-Breathing Self-Gated 4D-Lung MRI with wave-CAIPI", Proc. Intl. Soc. Mag. Reson. Med. **27** (2019)

M. Stich, J.A.J. Richter, T. Wech, T.A. Bley, H. Köstler, A.E. Campbell-Washburn, "Dwell Time Compensation of the Gradient System Transfer Function (GSTF): Field Camera versus Phantom-based Measurement", Proc. Intl. Soc. Mag. Reson. Med. **27** (2019)

P. Eirich, T. Wech, M. Stich, J.A.J. Richter, T.A. Bley, H. Köstler, "Spiral imaging using a fully automatic pre-emphasis based on the Gradient System Transfer Function (GSTF)", Proc. Intl. Soc. Mag. Reson. Med. **27** (2019)

J.A.J. Richter, T. Wech, A.M. Weng, M. Stich, S. Weick, H. Köstler, "Accelerated Free-Breathing Self-Gated 4D-Lung MRI with wave-CAIPI", Magn Reson Mater Phy (2019) **32** (Suppl 1): 107.

J.A.J. Richter, T. Wech, A.M. Weng, M. Stich, N. Jin, T.A. Bley, H. Köstler, "Accelerated 4D Flow MRI with wave-CAIPI", Proc. Intl. Soc. Mag. Reson. Med. **28** (2020)

C | Affidavit / Eidestattliche Erklärung

I hereby confirm that my thesis entitled ”Wave-CAIPI for Accelerated Dynamic MRI of the Thorax” is the result of my own work. I did not receive any help or support from commercial consultants. All sources and / or materials applied are listed and specified in the thesis. Furthermore, I confirm that this thesis has not yet been submitted as part of another examination process neither in identical nor in similar form.

Würzburg, 05.11.2020 Julian Richter

Hiermit erkläre ich an Eides statt, die Dissertation ”Beschleunigte Dynamische MR-Bildgebung des Thorax mit wave-CAIPI” eigenständig, d.h. insbesondere selbständig und ohne Hilfe eines kommerziellen Promotionsberaters, angefertigt und keine anderen als die von mir angegebenen Quellen und Hilfsmittel verwendet zu haben. Ich erkläre außerdem, dass die Dissertation weder in gleicher noch in ähnlicher Form bereits in einem anderen Prüfungsverfahren vorgelegen hat.

Würzburg, 05.11.2020 Julian Richter

D | Acknowledgments

I am very grateful to Prof. Dr. Herbert Köstler for his extraordinary supervision and guidance throughout my work at his department. He always found the time to discuss issues related to my research and on many occasions provided efficient solution strategies.

Further, I would like to thank the other members of my thesis committee: Prof. Dr. Laura Schreiber, PD Dr. Peter Nordbeck and PD Dr. Dr. Bernhard Petritsch. The regular meetings with the thesis committee represented valuable milestones and provided an excellent opportunity to discuss the development of the project.

Special thanks goes to PD Dr. Tobias Wech, who gladly shared his expertise in MRI and always provided helpful guidance and support.

I had the pleasure of working in an exceptionally friendly working environment. My special thanks are extended to all the members of the Experimental Radiology, in particular: Philipp Eirich, Dr. Manuel Stich, Dr. Andreas Weng, Dr. Anne Slawig, Dr. Lenon Mendes Pereira, Juliana Bibiano, Katharina Rath, Johannes Portmann, Susanne Gaul, Hannah Scholten, Christiane Pfaff, Richard Dederichs and Vanessa Kümmel.

I am also grateful to Dr. Stefan Weick, Dr. Kathrin Breuer and Dr. Serge-Peer Ströhle for sharing their expertise in radiotherapy treatment and for many helpful discussions related to the 4D lung MRI project. I wish to acknowledge Dr. Jin Ning and Dr. Aleksander Kosmala for their contribution to the 4D flow MRI project.

I thank the Graduate School of Life Sciences for offering a well structured doctoral research training, many helpful courses and financial support for attending international conferences.

Finally, I am especially grateful to my parents, Bettina Richter and Dr. Jürgen Richter, as well as to my girlfriend Franziska Räder for continued support throughout my studies and my doctoral thesis.